Solitons and Volume Preserving Flow

GILLARD, MIKE

Centre for Particle Theory
Department of Mathematical Sciences

Durham University, Durham DH1 3LE, U.K.

Solitons and Volume Preserving Flow

A Thesis presented for the degree of

Doctor of Philosophy

September 2010

Author:

Mike Gillard

mike.gillard@durham.ac.uk

Supervisor:

Prof. Paul Sutcliffe

p.m.sutcliffe@durham.ac.uk

Solitons and Volume Preserving Flow

Mike Gillard

Submitted for the degree of Doctor of Philosophy

September 2010

Abstract

Solitons arise as solutions to non-linear partial differential equations. These equations are only analytically solvable in very few special cases. Other solutions must be found numerically. A useful technique for obtaining static solutions is gradient flow. Gradient flow evolution is in a direction which never increases energy, leading to solutions which are local minima. Here, a modified version of gradient flow referred to as volume preserving flow is introduced. This flow is constructed to evolve solutions towards local minima, while leaving a number of global quantities unaltered. Volume preserving gradient flow will be introduced and demonstrated in some simple models.

Volume preserving flow will be used to investigate minimal surfaces in the context of double bubbles. Work will reproduce explicit results for double bubbles on the two-torus and construct a range of possible minimisers on the three-torus. Domain walls in a Wess-Zumino model with a triply degenerate vacuum will be used to represent the surfaces of the bubbles. Volume preserving flow will minimise the energy of the domain walls while maintaining the volumes of the space they contain. Global minima will represent minimal surfaces in the limit in which the domain wall thickness tends to zero.

Numerical simulations of solitons in models which have conformal symmetry are problematic. Discretisation breaks the zero modes associated with changes of scale to negative modes. These lead to the collapse of solutions. Volume preserving flow provides a frame-

work in which minimisation occurs orthogonally to these zero modes, maintaining a scale for the minimisation.

Two such conformal models which permit Hopf solitons are the Nicole and AFZ models. They are comprised of the two components of the Skyrme-Faddeev model, taken to fractional powers to allow for solitons. Volume preserving flow will be used to find static solutions for a range of Hopf charges for each model. Comparisons will be made with the Skyrme-Faddeev model and general features of Hopf solitons will be discussed. A one parameter family of conformal Skyrme-Faddeev models will also be introduced. These models will be the set of linear combinations of the Nicole and AFZ models where the coefficients sum to one. Energy and topology transitions through this set of models will be investigated.

Declaration

The work in this thesis is based on research carried out at the Centre for Particle Theory, the Department of Mathematical Sciences, Durham University, England. No part of this thesis has been submitted elsewhere for any other degree or qualification and it is all my own work unless referenced to the contrary in the text.

Chapters 1 and 4 contains mostly background material which is included to place later work in context. The material in chapters 2, 3, 5, 6 and 7 covers my own work. The contents of chapters 6 and 7 can be found in the solo publication [1]. The contents of chapters 5 and 6 represent my own contribution to the joint publications [2] and [3] with Prof. P. M. Sutcliffe.

Acknowledgements

I am indebted to my supervisor, Prof. Paul Sutcliffe, for introducing me to the subject of this thesis and offering guidance, encouragement and helpful suggestions throughout my period of study. In addition I would like to thank David Foster and Derek Harland for useful discussions, and Rob Powell for some optimisation assistance.

I thank the Engineering and Physical Sciences Research Council for the financial support allowing me to produce this work.

I would also like to thank St Mary's College bar and its patronage, without which I might have finished this work much sooner!

Finally, thank you to all my family and friends who have supported me throughout my extended period of education.

Contents

List of Figures

List of Tables

Chapter 1

Solitons - An Introduction

1.1 Introduction

Topological solitons in field theory arise as solutions to nonlinear partial differential equations. In general, these solutions are some kind of stable localised blobs of energy and exist as a result of some topology present in the system. They solve the equations of motion and in many ways behave like particles with some finite size that roughly retain their shape in motion and are stable to small perturbations. There is often some sort of conserved topological charge associated with the solitons which can be used to classify solutions in certain systems. Usually, this is an integer and can be thought of as the number of blobs (or particles).

A simple example of a system which might be described as permitting topological solitons, is a set of equally separated pendulums, with each attached to its neighbours by identical rubber bands. Each pendulum has one degree of freedom, and can rotate in the plane perpendicular to the axis of rotation of the set of pendulums. Imagine all the pendulums are stationary, and none of the elastic bands are either stretched, nor slack. This would equate to a vacuum state, both for each individual pendulum, and for the system as a whole. Now, take the pendulum at one end of the line and rotate it through an angle of 2π, back to its vacuum state. Fix both ends. As all the pendulums are linked, the elastic bands along the line will stretch as the twist is imparted. The stretching will cause each pendulum to be perturbed from its vacuum state to lie at some angle, from zero at the unrotated end of the system through to 2π at the other end. Each pendulum

in between will then reside at an angle set by the following factors: the rubber bands springiness and any two from three of; a) the number of pendulums, b) their separation and c) the length of the system. If the system is at rest, the pendulums should form into a spiral through 2π. This could be defined to have a winding of one, which could be called a soliton with topological charge one. If the chain is long enough, the twisted section of the static configuration will be localised, with most of the pendulums in the ground state. Plotting the displacement angle against distance from the beginning of the configuration will give a localised curve of discrete points, traversing between 0 and 2π for one twist. If the system's energy is plotted, it will again be localised to the subset in which the previous curve is changing, with a maximum around the most vertical pendulum, i.e. when the angle approaches π. In fact, this reduces this system to a 1+1 dimensional problem. The system is described by a kink model, details of kinks will be given later. If any of the pendulums are perturbed slightly, the system should eventually come to rest in the same configuration as before the perturbation. Winding the end pendulum through another rotation, the stationary configuration could be called a charge two soliton and a winding angle of $2\pi N$ would give a charge N soliton. The integer N captures the topological character of the system. Here, topology was imparted by the boundary conditions, with a winding occurring in between.

In general, the map will have an associated non-trivial homotopy group which will classify the topological space. These homotopy groups are well known in algebraic topology and will be of great use here. Homotopy describes the ability of manifolds to be continuously deformed into one another. If two manifolds, $\mathcal{S}^n$ and $\mathcal{M}$, are related by two continuous functions, f and g, then f and g are homotopic if f can be continuously deformed into g (and vice versa since the concept is an equivalence relation). The set of equivalence classes are then given by $f, g : \mathcal{S}^n \to \mathcal{M}$. The two functions are equivalent if one can be continuously deformed into the other, such that there exists a continuous map, $h_{f,g}$ where $h_{f,g} : \mathcal{S}^n \times [0,1] \to \mathcal{M}$. The two end points are the maps f and g. The related homotopy group is $\pi_n(\mathcal{M})$. Later, we shall be interested in maps between an $\mathcal{S}^3$ and an $\mathcal{S}^2$. The related homotopy group is well known, where $\pi_3(\mathcal{S}^2) = \mathbb{Z}$. This gives distinct homotopy classes for each element of $\mathbb{Z}$. We are also interested in kinks solutions. The topology of the kink solutions is given by the boundary conditions, that is, by maps

to the vacuum manifold $\mathcal{V} \subset \mathcal{M}$. The d dimensional theory will then have homotopy given by $\pi_{d-1}(\mathcal{V})$. For one dimensional kink solutions this is $\pi_0(\mathcal{V})$, maps from points to the vacuum. In the previously mentioned pendulum example the vacuum manifold consists of all $2\pi N$ possible windings, i.e. $\pi_0(\mathcal{S}^1) = \mathbb{Z}$. Each choice of $N \in \mathbb{Z}$ will give a different homotopy class and clearly each class will not be able to continuously deform into another class is both ends are kept fixed (and the system does not break down). In other kink models, $\mathcal{V}$ will consist of a series of fixed points. In this case, the homotopy classes relate to the different choices of boundary conditions, i.e. which vacua the solutions will move between. Boundary conditions that are distinct (such that one cannot be continuously deformed into the other) lead to topologically distinct solutions to the differential equations classified by their homotopy class. Solutions of one homotopy class cannot be continuously deformed to solutions with a different class, making the soliton stable, at least up to small perturbations. It also prevents them being able to unwind to a trivial solution, i.e. to the vacuum. For details on homotopy or algebraic topology, see [4, 5].

Early work on topological solitons studied systems in one spatial dimension. The dynamics of such solutions were investigated and characteristic properties of solitons were found. This led to much analytical investigation which draws on many different areas of mathematics. With increased computing power and the spread of knowledge about solitons and techniques of investigation, more complicated systems were investigated - including those in higher dimensions. Modern computing power allows for investigation of solitons in one, two, three and even higher spatial dimensions. Much is known about many different types of solitons in many different models, although there is so much that is still unknown.

Derrick's Theorem Topological solitons exist, at least in part, due to the non-trivial topology and boundary conditions. Not all systems that satisfy these conditions will have solitons. There does exist a simple theorem due to Derrick [6], which evaluates the behaviour of the energy function under scaling. He noted that for many field theories defined on flat space there are no non-vacuum static field configurations for which the variation of the energy with respect to spatial rescaling vanishes. Therefore the only

field configuration which is a stationary point of the energy is the vacuum, as any field configuration which is a stationary point of the energy must also be a stationary point against length variations. This implies that no static finite energy solutions to the field equations exist in any homotopy class excluding the one which contains the vacuum, so there are no topological solitons.

So, a finite energy field $\Theta(\boldsymbol{x})$, will be related to a one parameter family of fields $\Theta_{[\lambda]}(\boldsymbol{x})$ by spatial rescaling $\boldsymbol{x} \to \lambda\boldsymbol{x}$: $\lambda > 0$. Let the energy as a function of the scaling be $e(\lambda) = E\left(\Theta_{[\lambda]}\right)$. If $e(\lambda)$ has no stationary points, no finite energy static field configurations exist past the vacuum. Consider a scalar field, $\Theta(\boldsymbol{x}) = \phi(\boldsymbol{x})$, under rescaling $\phi(\boldsymbol{x}) \to \phi(\lambda\boldsymbol{x}) \equiv \phi_{[\lambda]}(\boldsymbol{x})$. Then, the gradient will scale like $\partial_i\phi_{[\lambda]}(\boldsymbol{x}) = \lambda\partial_i\phi(\lambda\boldsymbol{x})$. This information can then be used to find whether or not a given scalar field theory could permit topological solitons.

A free scalar field theory in a potential in d spatial dimensions would have a static energy given by

$$E(\phi) = \int \left(\partial_i\phi\partial_i\phi + U(\phi)\right) d^dx \equiv E_2 + E_0, \tag{1.1.1}$$

where the energy has been divided into the contributions of two terms. The subscripts relate to behaviour under scaling. The gradient product will scale like λ^2, as stated previously, whilst the potential is purely a function of the field and so is unaffected by scaling. The infinitesimal volume element d^dx will scale like λ^{-d}. Thus, the energy will transform under scaling like

$$e(\lambda) = \lambda^{2-d}E_2 + \lambda^{-d}E_0. \tag{1.1.2}$$

It is easy to see that $e(\lambda)$ can only have stationary points if $d = 1, 2$, since $E_0, E_2 \geq 0$. In one dimension, stationary points occur when $\lambda = \sqrt{E_0/E_2}$ and the topological solitons are called kinks. In two dimensions, topological solitons are possible, provided $E_0 = 0$, i.e. there is no potential. Here, $e(\lambda)$ is independent of the scaling choice. The theory is then scale invariant, and examples of solitons in this kind of theory are called sigma model lumps. Both will be introduced later.

Expanding the Lagrangian of scalar field theories to include terms with higher order derivatives or higher power derivatives will allow for solitons in higher dimensions. Take

a field theory with an energy

$$E = \int \left(\partial_i \phi \partial_i \phi + \left(\partial_j \phi \partial_k \phi \right)^2 \right) d^d x \equiv E_2 + E_4. \tag{1.1.3}$$

The energy will the act under scaling like

$$e(\lambda) = \lambda^{2-d} E_2 + \lambda^{4-d} E_4. \tag{1.1.4}$$

Topological solitons are then permitted when $d = 3$. One may also wish to consider a potential term E_0 or define a gauge potential but that will not be necessary in this discussion. When $d=3$, (1.1.4) will have stationary points when $\lambda = \sqrt{E_2/E_4}$. One such theory (that contains a collection of scalar fields), the Skyrme-Faddeev model [7], will be introduced later which has topological solitons called Hopf solitons. In this case, the theory contains a collection of scalar fields. Hopf solitons can also be found by taking the components E_2 or E_4 and raising them to fractional powers resulting in scale invariant field theories. Two such models, the Nicole model [8] and the AFZ model [9, 10] will be discussed in detail later.

Bogomolny Bounds In general the field equations satisfied by topological solitons are second order partial differential equations. In many theories it is possible to reduce these to first order partial differential equations which are almost always much simpler to work with. The first examples were discovered by Bogomolny [11], with many more following. These Bogomolny equations are first order and contain only spatial derivatives with solutions describing soliton configurations. In these theories the energy is bounded from below by some multiple of the topological charge. This is called the Bogomolny bound. The Bogomolny bound is attained by configurations which satisfy the Bogomolny equations. Therefore solutions of the Bogomolny equations with a given topological charge, N, will all have the same energy, thus solutions form an N-soliton solution space - the moduli space, $\mathcal{M}_N$. They will be stable solutions of the Euler-Lagrange equations.

Two examples of field theories with topological solitons are given next. Details of Hopf solitons can be found in a later chapter.

1.2 Kinks

Kinks are the simplest topological solitons, they represent the least-energy transition of a scalar field between two separated vacua. If the field is in a vacuum the system has zero energy. Consider a 1+1 dimensional field theory, with a Lagrangian density such as

$$\mathcal{L} = \frac{1}{2}\partial^\mu\phi\partial_\mu\phi - U(\phi). \tag{1.2.1}$$

The minima of $U(\phi)$ are the vacua of the field theory and are usually arranged so that they occur at $U=0$. The type field theories of interest here are scalar field theories where the transitions, i.e. the static solutions which solve the equations of motion, are called kinks.

The topology of the system allows the field to tend to different values, $\phi_\pm$, at $x=\pm\infty$, $\phi_\pm$. These are usually taken to be the two vacuum solutions of the field theory, which can lead to static solutions in one spatial dimension having a finite energy. If the system were in the same vacuum at both spatial infinities the system could be continuously deformed, so that the entire field was in this vacuum. The field can transverse the gap in the space between in whichever way it wishes. The energy of this will be large if, either most of the field is not in a vacuum, or the transition is too quick. If the field changes rapidly over a short space the gradient terms in the Lagrangian will be large resulting in a large energy.

The energy of a given configuration is bounded from below. The bound is derived from the Bogomolny equations where the field equations are reduced from second order to first order in certain circumstances, which comes from the topology of the system. The case where the bound is attained is the minimal energy case. It can be easily found that the inequality

$$\left(\partial_x\phi \pm \sqrt{2U(\phi)}\right)^2 \geq 0, \tag{1.2.2}$$

must hold. Expanding and integrating this over the real line leads to the energy bound, for static fields, given by

$$E \geq \left|\int_{\phi_-}^{\phi_+} \sqrt{2U(\phi)}d\phi\right|. \tag{1.2.3}$$

The energy bound also applies to time dependent field, where the integral runs between

the two vacua. To attain this bound, the fields must be static and satisfy

$$\partial_x \phi = \pm\sqrt{2U(\phi)}. \tag{1.2.4}$$

These are the Bogomolny equations. Solutions that exist will be kinks (if + is used above) and anti-kinks (if − is used). These kink solutions are automatically static, since they are critical points of the energy.

Since the potential U is never negative it can be redefined in terms of a superpotential, W, where

$$U(\phi) = \frac{1}{2}\left(\frac{dW}{d\phi}\right)^2, \tag{1.2.5}$$

in which case, the energy bound can be simply integrated, making the lower bound equal to the positive difference between the values of the superpotential in the two vacua.

$$E \geq \left|W(\phi_+) - W(\phi_-)\right|. \tag{1.2.6}$$

When the bound is attained, the energy in the kink is equal to difference in the superpotential across the kink. The Bogomolny equations then become

$$\partial_x \phi = \pm\frac{dW}{d\phi}. \tag{1.2.7}$$

The superpotential will play an important role later. It also has an important role in supersymmetric theories, although this is beyond the scope of the discussion here.

1.2.1 ϕ^4 Kinks

The simplest non-trivial real scalar field theory is ϕ^4 theory. In the case of ϕ^4 kinks, the Lagrangian density can be written as

$$\mathcal{L} = \frac{1}{2}\partial^\mu\phi\partial_\mu\phi - \lambda\left(m^2 - \phi^2\right)^2. \tag{1.2.8}$$

This equation has two global minima, at $\phi = \pm m$ and has field equations

$$\partial^\mu\partial_\mu\phi - 4\lambda\phi\left(m^2 - \phi^2\right) = 0. \tag{1.2.9}$$

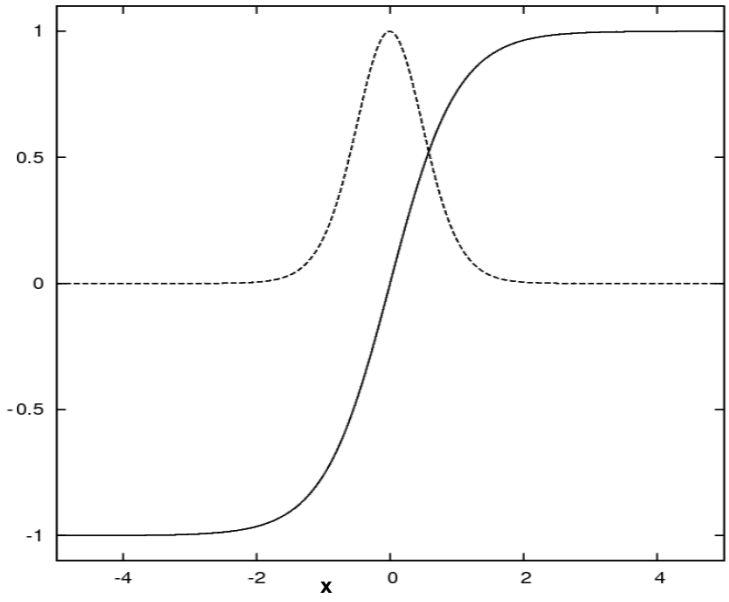

Figure 1.1: The kink solution (solid) $\phi(x)$, and its associated energy density (dashed) $\mathcal{E}(x)$, of a ϕ^4 kink solution, setting $\lambda = \frac{1}{2}$, $m = 1$ and $a = 0$. The general characteristics of the plots are the same for any values of the parameters. For these parameters, the field and energy density both reach the same maxima, though this would not be the case for other parameter values

There are then three possible situations. If the field is in the same vacua at $x = \pm\infty$ then it can be continuously deformed so that all the field lies in the same vacuum. The other two cases are essentially the same, up to a reflection. Here, the field is in different vacua at the two spatial infinities. The case where $\phi(-\infty) = -m$ and $\phi(+\infty) = +m$ is the kink and the reverse is the anti-kink. The Bogomolny bound for the kink (or anti-kink) is then

$$E \geq \frac{4}{3} m^3 \sqrt{2\lambda}, \tag{1.2.10}$$

with the equality attained when the Bogomolny equation is satisfied, i.e.

$$\partial_x \phi = \sqrt{2\lambda} \left(m^2 - \phi^2 \right). \tag{1.2.11}$$

Integration gives the kink solution:

$$\phi(x) = m \tanh\left(\sqrt{2\lambda} m \left(x - a \right) \right). \tag{1.2.12}$$

It is also easy to calculate the energy density of the static solution which follows from the Lagrangian density given above. A plot of the energy density (given below) and the field (given above) can be found in figure 1.1

$$\mathcal{E} = 2\lambda m^4 \mathrm{sech}^4\left(\sqrt{2\lambda} m \left(x - a \right) \right). \tag{1.2.13}$$

Integrating this gives the Bogomolny bound for the energy.

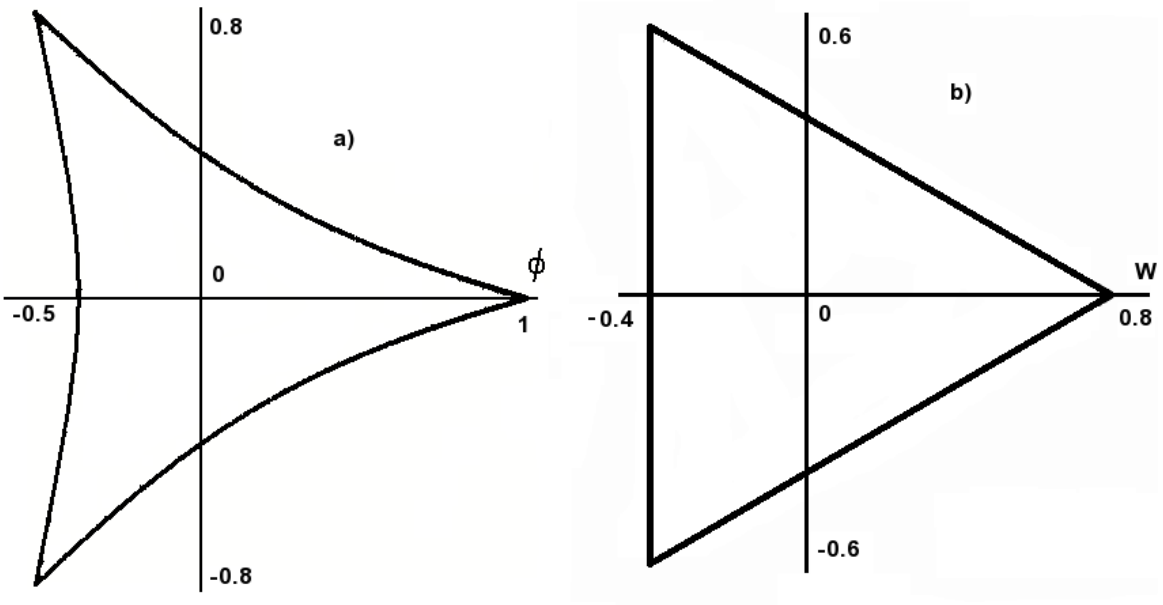

Figure 1.2: The kinks linking the three vacua in the ϕ^6 model in ϕ-space **a)** and W-space **b)** The three vacua are located at the corners, and the three kinks are the lines connecting the vacua. Note the scales on the two graphs are not the same

It is possible to set up a system with multiple well separated pairs of kinks and anti-kinks. There is an attractive force between the kink and anti-kink which brings them together and can cause them to annihilate. The system will usually then evolve into one of the three cases mentioned above, depending on whether the system contains an extra kink or anti-kink which has no partner to annihilate it. Other situations such a back-reflections can also occur under the correct conditions, but that will not be of interest here.

1.2.2 ϕ^6 Kinks

A complex scalar field can also be used. One such field theory has a ϕ^6 potential, such that

$$\mathcal{L} = \frac{1}{4}\partial^\mu \bar{\phi}\partial_\mu \phi - \lambda \left|m - \phi^3\right|^2, \tag{1.2.14}$$

where here the superpotential is written as $U(\phi) = |W'(\phi)|^2$. m will scale the position of the vacua while λ will scale the size of the kinks. This field theory has three complex vacua, if $\lambda, m = 1$ they are located at the three cubed roots of unity. These are shown in figure 1.2a). The curves passing between these corner points represent the path of the kinks in the complex field space. Figure 1.2b) shows the vacua and kinks in the superpo-

tential space. It is worth noting here that the kinks progress between the vacua in straight lines through superpotential space [12] (a useful point that will be later exploited). The three vacua are equally spaced, meaning that a kink traversing between any two vacua has the same energy - which will also be important later. The superpotential is given by

$$W(\phi) = \phi - \frac{\phi^4}{4}. \tag{1.2.15}$$

As the field is now complex, the theory has a $U(1)$ symmetry and so the field can be rotated by an arbitrary phase. There are now a one-parameter family of Bogomolny equations associated with (1.2.14). Naively using the same energy formula as for kinks with a real scalar field (1.2.6), the energy of these kinks are given by the difference in superpotential between any two vacua, i.e.

$$|W(\phi_i) - W(\phi_j)| = \frac{3\sqrt{3}}{4}, \tag{1.2.16}$$

Note, $i, j = 1, 2, 3$ and $i \neq j$. This energy has also been confirmed numerically to within a fraction of a percent. This equation is not simple to prove, although the domain walls for this system have an associated topological charge. When the Bogomolny bound is attained, the modulus of this topological charge gives to the energy above [13, 14].

1.2.3 Kinks in Higher Dimensions

Domain walls can be formed by increasing the number of space dimensions in which the scalar field theory lives. So far the theories discussed have lived in 1+1 dimensions. A kink model, like the ones above, can exist in more spatial dimensions, but the field is only a function of one direction. A simple model would be a 2+1 dimensional system, with the kink extended along the second space direction, forming a domain wall. Since this extra spatial direction is infinite, the domain wall would have infinite total energy, but would have a finite energy per unit length. The energy of the domain wall per unit length can be thought of as the tension in the wall.

A kink model can also allow the field to vary in all the spatial directions. If a 1+1 dimensional slice is taken between the two vacua the cross-section of the domain wall will look like the kink solution of the 1+1 dimensional theory. Placing the complex ϕ^6 theory

in 2 or more spatial dimensions allows for the junction of different domain walls. In this theory there are three vacua, and so three different domain walls between each of the vacua which allows for the three walls to meet in a junction. The Bogomolny equation obeyed by these junctions will depend on the orientation of the three vacua. If the order is switched the junction will obey the anti-Bogomolny equation. The effect of this is to create an attraction between a junction and an anti-junction, similar to the kink anti-kinks, meaning they will tend to annihilate. Infinitely long walls obey the Bogomolny and anti-Bogomolny equations simultaneously.

Whilst these junctions can be found using numerical techniques, no rigorous proof is available that these junctions exist. The angles between each domain wall will depend on the tension in each of the individual walls. In the ϕ^6 theory, the tension in each wall is the same and so are the angles between the walls, since the vacua are equally spaced, but if they were different the angles would alter in order to balance the tensions.

1.3 $O(3)$ Sigma Model

Sigma models are nonlinear scalar field theories that take values on a Riemannian manifold. The field describes a differentiable map from some space to this target space with a Riemannian metric. They have applications across a wide range of subjects. The simplest sigma model is the $O(3)$ sigma model. It describes a map from Euclidean space to the unit 2-sphere. The field is a three component unit vector, $\boldsymbol{\phi}=(\phi_1,\phi_2,\phi_3)$, with $\boldsymbol{\phi}\cdot\boldsymbol{\phi}=1$ and the model is simply a massless free theory, i.e.

$$\mathcal{L}=\frac{1}{4}\partial_\mu\boldsymbol{\phi}\cdot\partial^\mu\boldsymbol{\phi}. \tag{1.3.1}$$

A Lagrange multiplier can be used to enforce the constraint $\boldsymbol{\phi}\cdot\boldsymbol{\phi}=1$, in this case the Lagrangian density would become

$$\mathcal{L}=\frac{1}{4}\partial_\mu\boldsymbol{\phi}\cdot\partial^\mu\boldsymbol{\phi}+\nu\left(1-\boldsymbol{\phi}\cdot\boldsymbol{\phi}\right). \tag{1.3.2}$$

$\boldsymbol{\phi}$ will satisfy the Euler-Lagrange equation, given by

$$\partial_\mu\left(\frac{\partial\mathcal{L}}{\partial(\partial_\mu\boldsymbol{\phi})}\right)-\frac{\partial\mathcal{L}}{\partial\boldsymbol{\phi}}=\frac{1}{2}\partial_\mu\partial^\mu\boldsymbol{\phi}+2\nu\boldsymbol{\phi}=0, \tag{1.3.3}$$

The Lagrange multiplier can then be found by taking the product of this equation with the field $\boldsymbol{\phi}$, so that using the constraint $\boldsymbol{\phi}\cdot\boldsymbol{\phi}=1$ gives,

$$\boldsymbol{\phi}\cdot\partial_\mu\partial^\mu\boldsymbol{\phi}+4\nu\boldsymbol{\phi}\cdot\boldsymbol{\phi}=0,\quad \text{i.e.}\quad \nu=\frac{1}{4}\partial_\mu\boldsymbol{\phi}\cdot\partial^\mu\boldsymbol{\phi}, \tag{1.3.4}$$

utilising that the field is on the $\mathcal{S}^2$, such that

$$\boldsymbol{\phi}\cdot\partial_\mu\partial^\mu\boldsymbol{\phi}=\partial_\mu\left(\boldsymbol{\phi}\cdot\partial^\mu\boldsymbol{\phi}\right)-\partial_\mu\boldsymbol{\phi}\cdot\partial^\mu\boldsymbol{\phi}, \tag{1.3.5}$$

as $\partial_\mu\left(\boldsymbol{\phi}\cdot\boldsymbol{\phi}\right)=0$.

Without loss in generality, a value of the field at infinity can be arbitrarily chosen, take $\boldsymbol{\phi}(\infty)=(0,0,1)$. This will be the vacuum field value for $\boldsymbol{\phi}$, and as the field tends to its vacuum value at infinity, its static energy will be finite. The static energy is

$$E=\frac{1}{4}\int\partial_i\boldsymbol{\phi}\cdot\partial_i\boldsymbol{\phi}\,d^dx. \tag{1.3.6}$$

At any given time, $\boldsymbol{\phi}$ is a map from $\mathbb{R}^d$ to $\mathcal{S}^2$. Identifying all points at infinity due to boundary conditions makes $\mathbb{R}^d$ topologically equivalent to a d-sphere, $\mathbb{R}^d\cup\{\infty\}\cong\mathcal{S}^d$. By Derrick's theorem, this Lagrangian can only have static, finite energy solutions if $d=2$. The map $\boldsymbol{\phi}:\mathcal{S}^2\to\mathcal{S}^2$ has a homotopy group $\pi_2(\mathcal{S}^2)=\mathbb{Z}$. The field theory classified by (1.3.6) has conformal symmetry as well as the rotational symmetry which gives the theory its name. The boundary condition breaks this symmetry: $O(3)\to O(2)$, preserving rotations in ϕ_1,ϕ_2. Due to the conformal symmetry the static solutions of this field theory will be invariant under scaling. For this reason they are usually referred to as lumps rather than solitons and will lie in an at least one-parameter family of solutions. The homotopy group shows that field configurations are characterised by the integer topological degree of the map, the topological charge N. N is taken to be the number of lumps in the system and is given explicitly as the pullback of the standard area form on the unit $\mathcal{S}^2$;

$$N=\frac{1}{8\pi}\int\boldsymbol{\phi}\cdot\left(\epsilon_{ij}\partial_i\boldsymbol{\phi}\times\partial_j\boldsymbol{\phi}\right)\,d^2x. \tag{1.3.7}$$

The Bogomolny bound of the $O(3)$ sigma model in the plane is $E\geq 2\pi|N|$, and is attained if

$$\partial_i\boldsymbol{\phi}\pm\epsilon_{ij}\boldsymbol{\phi}\times\partial_j\boldsymbol{\phi}=0. \tag{1.3.8}$$

The field theory can be re-expressed by taking a stereographic projection, using $\boldsymbol{\phi}(\infty) = (0, 0, 1)$. This gives the field in terms of a complex coordinate on the plane, W;

$$W = \frac{\phi_1 + i\phi_2}{1 + \phi_3}, \tag{1.3.9}$$

where W is a function of $z = x^1 + ix^2$. The Lagrangian is then given by

$$\mathcal{L} = \frac{\partial^\mu \overline{W} \partial_\mu W}{(1 + |W|^2)^2}. \tag{1.3.10}$$

This model is referred to as the $\mathbb{CP}^1$ sigma model, and the Bogomolny equation is now $\partial_{\bar{z}} W = 0$ (or anti-Bogomolny equation $\partial_z W = 0$). The bound can only be attained if W is a rational function of z. These are harmonic maps: $\mathbb{R}^2 \to \mathbb{CP}^1$ [15, 16]. If W is taken to be a rational map

$$W(z) = \frac{p(z)}{q(z)}, \tag{1.3.11}$$

then W attains the Bogomolny bound, and the topological charge will be the larger of the degrees of p and q. If the degree of the rational map is N, then W will be an N-lump solution with energy $2\pi N$. A plot of the energy density in the plane will in general give N localised lumps of energy.

For information regarding kinks, lumps and other topological solitons, see Topological Solitons [17] by Manton and Sutcliffe.

Chapter 2

Volume Preserving Flow

2.1 Gradient Flow and Volume Preserving Flow

The previous chapter introduced two systems that permit topological solitons. They were described by a Lagrangian, which is taken to be a function of the field, with the equations of motion giving the field equations of the system. In mechanics, systems described by a Lagrangian, $\mathcal{L}(\dot{\boldsymbol{x}}, \boldsymbol{x})$, with coordinates x^i on a given configuration space, are most commonly investigated by looking at their equations of motion. These can be found using the Euler-Lagrange equations, obtained by finding the stationary points in the variation of the Lagrangian;

$$\frac{d\left(\partial_{\dot{x}}\mathcal{L}\right)}{dt} = \frac{\partial \mathcal{L}}{\partial x}. \tag{2.1.1}$$

By taking $\mathcal{L}$ in terms of the kinetic $\mathcal{T}$ and potential $\mathcal{V}$ energy, this can be written in a general form as

$$\frac{d\left(g_{ij}\dot{x}^j\right)}{dt} = \frac{1}{2}\frac{\partial g_{jk}}{\partial x^i}\dot{x}^j\dot{x}^k - \frac{\partial \mathcal{V}}{\partial x^i}, \tag{2.1.2}$$

where g_{ij} is the metric, describing motion in the configuration space, where the kinetic energy is then given as $\mathcal{T} = \frac{1}{2}g_{ij}\dot{x}^i\dot{x}^j$. These are second order equations which describe how the system behaves as time advances. In addition to describing the motion of the system static solutions can also be found from here by finding minimal values of $\mathcal{V}$ which satisfy (2.1.2), taking $\dot{x}^i = 0$.

2.1.1 Gradient Flow

Another method of finding static solutions of systems of this type is the method of steepest decent, also referred to as gradient flow. Gradient flow takes a given point in the configuration space, which evolves in a direction of ever decreasing potential energy, i.e.

$$g_{ij}\dot{x}^j = -\partial_i \mathcal{V}. \tag{2.1.3}$$

At a given point in the configuration space, $\boldsymbol{x}$, the gradient flow is orthogonal to all hypersurfaces of constant $\mathcal{V}$ and is orientated in a direction of decreasing $\mathcal{V}$.

It is worth noting here that if the configuration space is taken to be Euclidean and Cartesian coordinates are used, then the gradient flow equations can be obtained directly from the Euler-Lagrange equations by replacing the second derivatives in time by first derivatives. The notion of time (in gradient flow) is different to the dynamical time in the field equations. It charts evolution through configuration space towards local minima.

Scalar Field theory

If we take a scalar field theory, the configuration space will be the space of fields $\{\phi(t, \boldsymbol{x})\}$, i.e. the set of all possible field configurations $\phi(\boldsymbol{x})$ at any given time. Gradient flow will then represent the dissipative relaxation of a given field configuration towards equilibrium. For example, consider a generic $1+d$ dimensional kink system with a real scalar field ϕ;

$$\mathcal{L} = \frac{1}{2}\partial^\mu \phi \partial_\mu \phi - U(\phi). \tag{2.1.4}$$

Applying the Euler-Lagrange field equations to this density, the non-linear wave equation is obtained

$$\partial^\mu \partial_\mu \phi + \frac{\partial U}{\partial \phi} = 0, \tag{2.1.5}$$

this implies that static equilibrium is reached if the configuration satisfies

$$\nabla^2 \phi = \frac{\partial U}{\partial \phi}. \tag{2.1.6}$$

To obtain a gradient flow for the system, the second order time derivative is replaced

by a first order one. Thus, at any point in the configuration space motion follows from

$$\kappa\partial_0\phi = \nabla^2\phi - \frac{\partial U}{\partial\phi}. \tag{2.1.7}$$

Note here, κ is a fixed positive dimensionful constant which can be absorbed into the time coordinate such that $\kappa\partial_0\phi \equiv \dot{\phi}$ by a simple rescale of the time variable. If the original time coordinate is labelled by τ, then let the rescaled time coordinate be labelled by t, such that $\partial_t\phi \equiv \dot{\phi}$. The time coordinate will be rescaled for each flow generated. It will be labelled t for convenience each time and relates to the evolution between different points in the configuration space. Also note that the Laplace operator can be written as $\nabla^2 \equiv \partial_i\partial_i$, where the index, i runs over the spatial coordinates of the configuration space i.e. $i=1\,..\,d$ in a $1+d$ dimensional space-time.

As we are only interested in static solutions, the time-independent energy of the system given by (2.1.4) is

$$E = \int \left(\frac{1}{2}\partial_i\phi\partial_i\phi + U(\phi)\right) d^dx = \int \mathcal{E}\, d^dx, \tag{2.1.8}$$

where $\mathcal{E}$ is the energy density. The variation of this energy gives

$$\begin{aligned}\delta\mathcal{E} &= \partial_i\phi\delta\left(\partial_i\phi\right) + \frac{\partial U}{\partial\phi}\delta\phi \\ &= \partial_i\phi\partial_i\left(\delta\phi\right) + \frac{\partial U}{\partial\phi}\delta\phi.\end{aligned} \tag{2.1.9}$$

This leads to the variational equation

$$\frac{\delta\mathcal{E}}{\delta\phi} = -\nabla^2\phi + \frac{\partial U}{\partial\phi}. \tag{2.1.10}$$

Thus the gradient flow equations for a scalar field theory are

$$\dot{\phi} = -\frac{\delta\mathcal{E}}{\delta\phi}. \tag{2.1.11}$$

This relation can be used to prove that the gradient flow evolution of the system will always decrease the energy towards a local minima, i.e. it will find a static configuration. If the energy evolves such that

$$\frac{dE}{dt} = \int \frac{\delta\mathcal{E}}{\delta\phi}\frac{\partial\phi}{\partial t}\, d^dx = -\int \dot{\phi}^2\, d^dx, \tag{2.1.12}$$

then it is either decreasing, lowering the energy, or zero, meaning the energy is constant in time. The gradient flow equations (2.1.11) act locally on the field. Gradient flow gives the direction of steepest decent of the energy functional, but the direction can be rescaled while still retaining its energy minimisation properties. It can be useful to simplify the equations or to circumvent potential problems such as singularities in the flow equations.

Setting $U(\phi)=(1-\phi^2)^2$, i.e. the ϕ^4 kink in 1+1 dimensions, gradient flow can be used to find the static kink solution introduced previously.

Complex Scalar Field theory

Gradient flow can also be applied to a 1+d-dimensional complex scalar field theory. The field can be described by a Lagrangian density such as

$$\mathcal{L} = \frac{1}{4}|\partial_\mu \phi|^2 - U(\phi), \tag{2.1.13}$$

where $U(\phi)$ is real valued, i.e. it can be written in the form $U(\phi) = |W'(\phi)|^2$. The Euler-Lagrange equations now give

$$\frac{1}{4}\partial_0^2\phi = \frac{1}{4}\nabla^2\phi - \frac{\partial U}{\partial \overline{\phi}}, \tag{2.1.14}$$

and the conjugate of this. The static configuration is given by

$$\nabla^2\phi = 4\frac{\partial U}{\partial \overline{\phi}}, \tag{2.1.15}$$

and the gradient flow equation can be written (again with a rescaling of time) by replacing second time derivatives with first time derivatives;

$$\dot{\phi} = \nabla^2\phi - 4\frac{\partial U}{\partial \overline{\phi}}. \tag{2.1.16}$$

The static energy of a 1+d-dimensional complex scalar field theory of this type, found from its Lagrangian, is

$$E = \int \left(\frac{1}{4}|\partial_i \phi|^2 + U(\phi)\right) d^d x, \tag{2.1.17}$$

where again the energy density is represented by $\mathcal{E}$. Variation of the energy density leads to

$$\frac{\delta \mathcal{E}}{\delta \overline{\phi}} = -\frac{1}{4}\nabla^2\phi + \frac{\partial U}{\partial \overline{\phi}}, \tag{2.1.18}$$

and so the gradient flow equations for a complex scalar field theory are given by

$$\dot{\phi} = -\frac{\delta \mathcal{E}}{\delta \overline{\phi}}. \tag{2.1.19}$$

The conjugates of both equations also apply. These equations obviously apply directly to real scalar field theory, since for a real field, $\overline{\phi}=\phi$.

This gradient flow will decrease the energy towards a local minimum. In a complex system, the energy evolution can be broken down to its complex and conjugated parts, i.e.

$$\frac{dE}{dt} = \int \left(\frac{\delta \mathcal{E}}{\delta \phi}\frac{\partial \phi}{\partial t} + \frac{\delta \mathcal{E}}{\delta \overline{\phi}}\frac{\partial \overline{\phi}}{\partial t} \right) d^d x = \int \left(-\dot{\overline{\phi}}\frac{\partial \phi}{\partial t} - \dot{\phi}\frac{\partial \overline{\phi}}{\partial t} \right) d^d x = -2\int |\dot{\phi}|^2 \, d^d x, \tag{2.1.20}$$

which is either decreasing, lowering the energy, or zero, meaning the energy is constant in time.

These complex scalar gradient flow equations can be applied to (2.1.13) using the ϕ^6 potential, $U(\phi)=|1-\phi^3|^2$, to find each of the three kinks in 1+1 dimensions in a similar way as with the ϕ^4 kinks. Setting the field at $x=\pm\infty$ to the correct vacua and evolving the rest of the field using the above defined gradient flow. A 1+2 dimensional domain wall can also be found from this system. If the two opposing sides of the lattice are set to different vacua, and the other two sides are periodic, then the resulting energy calculated divided by the length of the periodic lattice will be the energy per unit length, i.e. the tension of the domain wall.

2.1.2 Volume Preserving Flow

The gradient flow equations (2.1.19) give a direction of motion through configuration space of non-increasing energy. Gradient flow in the real Ginzburg-Landau model can be modified to preserve the total average of an effective magnetic field that depends on time, which is added for this purpose. It has been used to study phase ordering and interface-controlled coarsening [18], among other things. This section will discuss a generalisation of this type of flow for both real and complex scalar field theories. This volume preserving flow will be able to preserve multiple global quantities relating to the field theory whilst still providing energy minimisation within these constraints.

Taking the gradient flow of another quantity relating to the field, e.g.

$$V = \int_{\mathcal{M}} \upsilon \, d^d x, \tag{2.1.21}$$

where the space $\mathcal{M}$ has a total volume

$$V_{\mathcal{M}} = \int_{\mathcal{M}} d^d x. \tag{2.1.22}$$

V will be referred to as the volume, for reasons which will become apparent later, although it could be any desired quantity relating to the field theory.

The local density, υ, will have an associated gradient flow direction, f;

$$f = -\frac{\delta \upsilon}{\delta \overline{\phi}} = \frac{\partial \phi}{\partial t_V}, \tag{2.1.23}$$

where an associated flow time, t_V, has been introduced. Taking the static energy of a given field theory to be E, with a local energy density $\mathcal{E}$, the gradient flow direction F of this will be

$$F = -\frac{\delta \mathcal{E}}{\delta \overline{\phi}} = \frac{\partial \phi}{\partial t_E}. \tag{2.1.24}$$

If an inner product of two functions a, b is given as

$$\langle a, b \rangle = \frac{\int \overline{a} b \, d^d x}{\int d^d x}, \tag{2.1.25}$$

where taking the conjugate equates to switching the function order, i.e.

$$\overline{\langle a, b \rangle} = \langle \overline{a}, \overline{b} \rangle = \frac{\int a \overline{b} \, d^d x}{\int d^d x} = \langle b, a \rangle \,, \tag{2.1.26}$$

then a projection of one direction onto another can be taken. If the two directions are identical, e.g. f, this will give a magnitude of the force f, i.e. $\langle f, f \rangle = \|f\|^2$. A unit vector in this direction can be defined such that

$$\hat{f} = \frac{f}{\|f\|} \quad \text{with} \quad \left\langle \hat{f}, \hat{f} \right\rangle = 1. \tag{2.1.27}$$

Using this, it is possible to construct a gradient flow in a direction which will reduce E but will not change V. The amount of a force A in the direction $\hat{f}$ is given by the inner product $\left\langle \hat{f}, A \right\rangle$. Then the projection of A onto $\hat{f}$ is $\left\langle \hat{f}, A \right\rangle \hat{f}$. Then, the direction $B = A - \left\langle \hat{f}, A \right\rangle \hat{f}$ will be orthogonal to f.

Applying this to the field theory will give a gradient flow which will reduce the energy but leave V unchanged;

$$\dot{\phi} = F - \left\langle \hat{f}, F \right\rangle \hat{f}. \tag{2.1.28}$$

It can easily be seen that the flow will preserve V and also always reduce the energy E to a local minima. To preserve V, it is required that

$$\frac{dV}{dt} = 0. \tag{2.1.29}$$

If the total volume of the space, $\mathcal{M}$, is given by $V_{\mathcal{M}}$:

$$\frac{dV}{dt} = \int_{\mathcal{M}} \frac{d\upsilon}{dt}\, d^d x = 2\Re \int_{\mathcal{M}} \frac{\delta \upsilon}{\delta \phi} \frac{\partial \phi}{\partial t}\, d^d x = -2\Re \int_{\mathcal{M}} \bar{f}\dot{\phi}\, d^d x = -2V_{\mathcal{M}} \Re \left\langle f, \dot{\phi} \right\rangle. \tag{2.1.30}$$

This equation is zero by construction as the new flow $\dot{\phi}$ is defined to be in a direction orthogonal to f, i.e. $\left\langle f, \dot{\phi} \right\rangle = 0$, although it is simple to show. If $\left\langle \hat{f}, F \right\rangle = p$

$$\left\langle \hat{f}, \dot{\phi} \right\rangle = \left\langle \hat{f}, F - \left\langle \hat{f}, F \right\rangle \hat{f} \right\rangle = \left\langle \hat{f}, F \right\rangle - \left\langle \hat{f}, p\hat{f} \right\rangle = p - p = 0, \tag{2.1.31}$$

since $\left\langle \hat{f}, \hat{f} \right\rangle = 1$. Therefore V is preserved by this flow.

It is also simple to show that the energy will decrease towards a local minima using this flow.

$$\begin{aligned} \frac{dE}{dt} &= \int_{\mathcal{M}} \frac{d\mathcal{E}}{dt}\, d^d x = 2\Re \int_{\mathcal{M}} \frac{\partial \overline{\phi}}{\partial t} \frac{\delta \mathcal{E}}{\delta \overline{\phi}}\, d^d x = -2\Re \int_{\mathcal{M}} \frac{\partial \overline{\phi}}{\partial t} F\, d^d x = -2V_{\mathcal{M}} \Re \left\langle \dot{\phi}, F \right\rangle \\ &= -2V_{\mathcal{M}} \Re \left\langle \dot{\phi}, \dot{\phi} + \left\langle \hat{f}, F \right\rangle \hat{f} \right\rangle = -2V_{\mathcal{M}} \left\langle \dot{\phi}, \dot{\phi} \right\rangle - 2V_{\mathcal{M}} \Re \left\langle \dot{\phi}, p\hat{f} \right\rangle \\ &= -2V_{\mathcal{M}} \left\langle \dot{\phi}, \dot{\phi} \right\rangle \leq 0, \end{aligned} \tag{2.1.32}$$

using $\left\langle \dot{\phi}, \hat{f} \right\rangle = 0$ and $\left\langle \hat{f}, F \right\rangle = p$.

This flow is a generalised version of the volume preserving flow in the real Ginzburg-Landau theory [18]. It is recovered when the field is restricted to be real, $\phi = \overline{\phi} = \varphi$ with a volume

$$V = \int \frac{\varphi - \varphi_\infty}{2\varphi_\infty} dx, \tag{2.1.33}$$

where $\pm\varphi_\infty$ are the two real vacua. Clearly, the volume flow is constant, and the volume preserving flow is

$$\dot{\varphi} = F - \langle F \rangle, \tag{2.1.34}$$

where $\langle F \rangle \equiv \langle 1, F \rangle$ is the average value of F. This flow will preserve the average value of the field, since $\partial_t \langle \varphi \rangle = 0$. The Ginzburg-Landau flow will match closely with the ϕ^4 example presented later in the chapter.

Preserving Multiple Volumes

It is possible to make a flow that will leave $i = 1 \ldots n$ quantities relating to the field theory unchanged. Defining

$$V_i = \int_{\mathcal{M}} \upsilon_i \, d^d x, \tag{2.1.35}$$

will lead to flow directions f_i for each of these as before, i.e.

$$f_i = -\frac{\delta \upsilon_i}{\delta \bar{\phi}} = \frac{\partial \phi}{\partial t_{V_i}}. \tag{2.1.36}$$

These cannot all be normalised and projected out of the overall flow as the f_i's are not orthogonal to each other. Projecting one out, then projecting another will result in the overall flow being orthogonal to only the last flow projected out, unless all the flows are orthogonal to begin with. This means an orthonormal set of flows, $\hat{f}_i$ must be created. One possible method is

$$\tilde{f}_i = f_i - \sum_{j<i} \left\langle \hat{f}_j, f_i \right\rangle \hat{f}_j, \quad \text{then} \quad \hat{f}_i = \frac{\tilde{f}_i}{\|\tilde{f}_i\|}. \tag{2.1.37}$$

Here, a set of orthogonal flows $\tilde{f}_i$ are defined, by making each subsequent $\tilde{f}_i$ orthogonal to each of the $\tilde{f}_j$'s with $j < i$ already made orthogonal. These can then be normalised creating the orthonormal set of flows $\{\hat{f}_i\}$. These can now all be projected out of the overall flow as follows;

$$\dot{\phi} = F - \sum_{i=1}^{n} \left\langle \hat{f}_i, F \right\rangle \hat{f}_i, \tag{2.1.38}$$

which will keep all V_i's constant for $i = 1 \ldots n$ volumes. This is the volume preserving flow. It is again easy to prove this also preserves all the V_i's from (2.1.30) using (2.1.31);

$$\frac{dV_i}{dt} = \int_{\mathcal{M}} \frac{d\upsilon_i}{dt} \, d^d x = 2\Re \int_{\mathcal{M}} \frac{\delta \upsilon_i}{\delta \phi} \frac{\partial \phi}{\partial t} \, d^d x = -2\Re \int_{\mathcal{M}} \bar{f}_i \dot{\phi} \, d^d x = -2V_{\mathcal{M}} \Re \left\langle f_i, \dot{\phi} \right\rangle = 0. \tag{2.1.39}$$

Showing the energy always reduces is slightly more tricky. Since all the flows in the set $\{\hat{f}_i\}$ are orthonormal, they can be combined into an overall direction

$$\hat{f} = \frac{\sum_{i=1}^{n} \left\langle \hat{f}_i, F \right\rangle \hat{f}_i}{\sqrt{\sum_{i=1}^{n} \left\langle \hat{f}_i, F \right\rangle^2}}. \tag{2.1.40}$$

This makes the volume preserving flow

$$\dot{\phi} = F - \left\langle \hat{f}, F \right\rangle \hat{f}, \tag{2.1.41}$$

and so, as before, using $\left\langle \dot{\phi}, \hat{f} \right\rangle = 0$ (2.1.31) and $\left\langle \hat{f}, F \right\rangle = p$;

$$\begin{aligned} \frac{dE}{dt} &= \int_{\mathcal{M}} \frac{d\mathcal{E}}{dt}\, d^d x = 2\Re \int_{\mathcal{M}} \frac{\partial \overline{\phi}}{\partial t} \frac{\delta \mathcal{E}}{\delta \overline{\phi}}\, d^d x = -2\Re \int_{\mathcal{M}} \frac{\partial \overline{\phi}}{\partial t} F\, d^d x = -2V_{\mathcal{M}} \Re \left\langle \dot{\phi}, F \right\rangle \\ &= -2V_{\mathcal{M}} \Re \left\langle \dot{\phi}, \dot{\phi} + \left\langle \hat{f}, F \right\rangle \hat{f} \right\rangle = -2V_{\mathcal{M}} \left\langle \dot{\phi}, \dot{\phi} \right\rangle - 2V_{\mathcal{M}} \Re \left\langle \dot{\phi}, p\hat{f} \right\rangle \\ &= -2V_{\mathcal{M}} \left\langle \dot{\phi}, \dot{\phi} \right\rangle \leq 0. \end{aligned} \tag{2.1.42}$$

The same details will apply to multi-component scalar field theories, e.g. the Hopf map $\boldsymbol{\phi} : \mathcal{S}^3 \to \mathcal{S}^2$, where $\boldsymbol{\phi} = (\phi_1, \phi_2, \phi_3)$ and $\boldsymbol{\phi} \cdot \boldsymbol{\phi} = 1$.

2.2 Scalar Field Theory and Volume Preserving Flow

To see volume preserving flow in action, it is best to look at an example. One simple case is to show that, in two dimensions, the mean curve of minimal length enclosing a given area is with a circular perimeter. Take the static energy of a 2-dimensional ϕ^4 kink system, introduced earlier - where $m = 1$ and $\lambda = \frac{1}{2}$;

$$\mathcal{E} = \frac{1}{2} \partial_i \phi \partial_i \phi + \frac{1}{2} \left(1 - \phi^2\right)^2. \tag{2.2.1}$$

The kink solution in 1-dimension will attain the Bogomolny bound, and so has an energy defined previously (1.2.10), which becomes the energy per unit length or tension of the domain wall, $\mu = 4/3$. The set of field configurations that will be of interest are those where the field is in one vacua at the centre of the 2-dimensional space, with $\phi = -1 \equiv \phi_1$ say, and in another vacua at spatial infinity (or a reasonable distance away from the centre of the space) $\phi = 1 \equiv \phi_\infty$. The domain wall between the two vacua will form a

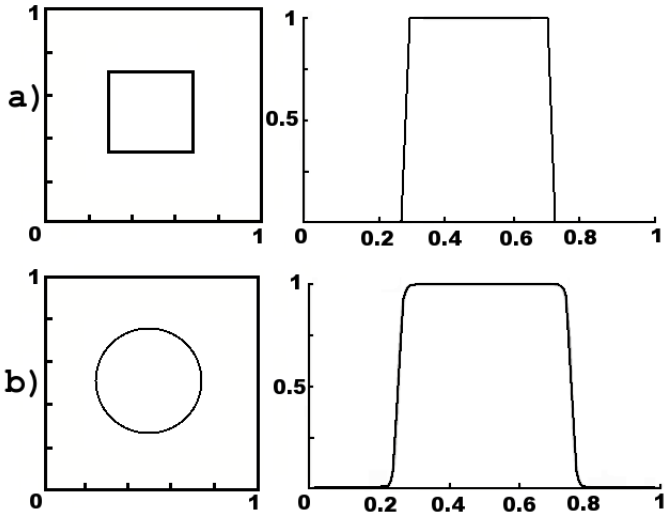

Figure 2.1: Initial and final states for the perimeter minimisation of an area on the unit lattice. The area being minimised is 0.25 times the area of the total area. **a)** is the starting configuration; a square of $\phi = -1$, surrounded by $\phi = 1$. The left plot is the plane, the boundary marks the perimeter of the bubble ($\phi = 0$), the contents of which are in the $\phi = -1$ vacuum. The cross sectional plot on the right shows this. The cross section is taken for x, where $y = 0.5$. Perimeter has length 2 here. **b)** is the final configuration, which is circular, with the domain walls formed. The domain walls are shown on the right, from the cross sectional plot of the volume density function. Perimeter has length 1.765 here.

closed perimeter around the region in which ϕ_1. It is clear that applying gradient flow (or an other general energy minimisation technique) will cause the domain wall to shrink, reducing the amount of ϕ_1 vacuum present until all the ϕ_1 disappears and the entire field is in a single vacuum. If an amount, or 'volume' of ϕ_1 is defined in some way, volume preserving flow will keep the total amount of ϕ_1 constant while still moving towards configurations with ever reduced energy until it finds a local minima. Details of the set up can be seen in figure 2.1.

The gradient flow equations (2.1.11) will be

$$F = -\frac{\delta \mathcal{E}}{\delta \phi} = \nabla^2 \phi + 2\phi \left(1 - \phi^2\right). \tag{2.2.2}$$

One possible 'volume' count for this system is to count 1 when $\phi = \phi_1$ and 0 when $\phi = \phi_\infty$, e.g.

$$V = \frac{1}{2} \int (1 - \phi)\, d^2x, \tag{2.2.3}$$

which will have an associated flow, f, such that

$$f = -\frac{\delta \upsilon}{\delta \phi} = \frac{1}{2}, \quad \text{where} \quad \hat{f} = 1. \tag{2.2.4}$$

Then, applying volume preserving flow (2.1.28) will give

$$\dot{\phi} = F - \left\langle \hat{f}, F \right\rangle \hat{f} = F - \langle F \rangle, \tag{2.2.5}$$

i.e. remove the average value of the gradient flow to preserve V.

The initial and final configurations can be found in figure 2.1 for the numerical solution found using volume preserving flow. Calculations will be conducted on a finite square domain, $\mathcal{M}$, where the region has a total area $V_{\mathcal{M}}$. $\mathcal{M}$ is approximated by a lattice of equally spaced points, with a lattice size of $100 \equiv \sqrt{V_{\mathcal{M}}}$ and a lattice spacing of $\Delta x = 0.1 (= \Delta y)$. Second order accurate finite difference methods are used to calculate derivatives. Solutions are evolved using an explicit method with first order accuracy, with a time step of $\Delta t = 0.1\Delta x^2$. Integrals are approximated as summations over the lattice. The perimeter of the final configuration can be found by dividing the energy of the domain wall by its tension - giving its length, $P \sim E/\mu = 1.765\sqrt{V_{\mathcal{M}}}$. The final area was $V/V_{\mathcal{M}} = 0.25$. A circle of area $V = 0.25V_{\mathcal{M}}$ will have a perimeter of $P = 2\sqrt{\pi V} \approx 1.772\sqrt{V_{\mathcal{M}}}$. This perimeter is within $\approx 0.5\%$ of the numerically calculated perimeter. Reducing the lattice size to 50 with a lattice spacing of $\Delta x = 0.25$ gives a perimeter of $E/\mu = 1.749V_{\mathcal{M}}$, within $\approx 1\%$. The domain walls in this system have a width of 5. On the first lattice, this is covered by 50 lattice points and has a size of $0.05\sqrt{V_{\mathcal{M}}}$. On the second lattice the domain wall is covered by 20 lattice points and has a size of $0.1\sqrt{V_{\mathcal{M}}}$. This result shows that, even with smaller lattices, providing the volumes and lattice size are chosen correctly this method of calculating minimal surfaces is very effective. Two dimensional calculations, found in chapter 3, will be done on a lattice with size 80 and lattice spacing $\Delta x = 0.2$. The minimal field configuration on this sized lattice equates to a perimeter of $E/\mu = 1.758\sqrt{V_{\mathcal{M}}}$.

For further details on numerical methods, consult [19–21].

2.3 O(3) Sigma Model and Volume Preserving Flow

The $O(3)$ sigma model in the plane has been introduced in chapter 1. Soliton solutions to this model are localised lumps of energy in the plane. N lumps will have an energy of $2\pi N$. Although static lump solutions can be found from rational maps, as seen previously, numerical calculations are difficult. Energy minimisation of static lump solutions will have a zero mode associated with changes in scale as the theory is scale invariant. When placed onto a finite lattice the zero mode is broken, becoming a negative mode and will cause any field configuration to shrink and so reduce its energy. The shrinkage will continue

until the soliton unwinds by falling through the lattice due to the scale of the soliton becoming of the same order as the lattice spacing [22]. The topology is lost in this case, but it can be preserved by using a certain lattice configuration [23] which allows lumps to be studied numerically. Splitting the plane into a regular square lattice and using volume preserving flow, static lump configurations can be found. The O(3) sigma model in the plane is a massless free scalar field theory of a unit vector field $\boldsymbol{\phi} = (\phi_1, \phi_2, \phi_3)$. Field configurations have a static energy density

$$\mathcal{E} = \frac{1}{4}\partial_i \boldsymbol{\phi} \cdot \partial_i \boldsymbol{\phi}, \tag{2.3.1}$$

with a Lagrange multiplier used to impose the constraint $\boldsymbol{\phi} \cdot \boldsymbol{\phi} = 1$.

The simulations will be conducted over a region of the plane, $\mathcal{M}$, with total area of

$$V_{\mathcal{M}} = \int_{\mathcal{M}} d^2x. \tag{2.3.2}$$

On the boundary, $\partial\mathcal{M}$, the field will be set to the vacua $\boldsymbol{\phi} = (0, 0, 1)$. The scale of $\mathcal{M}$ can be set arbitrarily, since the theory is scale invariant. This allows a unit lattice spacing to be employed.

Gradient flow can then be used to find static solutions that are local minima of this system. The flow $\boldsymbol{F}$ will be proportional to the field equations, such that

$$\frac{\partial \boldsymbol{\phi}}{\partial t_0} = -\frac{\delta \mathcal{E}}{\delta \boldsymbol{\phi}} = \frac{1}{2}\partial_i \partial_i \boldsymbol{\phi} + \frac{1}{2}\left(\partial_i \boldsymbol{\phi} \cdot \partial_i \boldsymbol{\phi}\right)\boldsymbol{\phi} \equiv \frac{\boldsymbol{F}}{2}, \tag{2.3.3}$$

Since $\boldsymbol{\phi}$ maps to $\mathcal{S}^2$ and the flow keeps the field on the two-sphere, $\boldsymbol{\phi} \cdot \boldsymbol{F} = 0$.

The scale invariance of the system will be slightly broken under numerical computations. The broken zero modes will cause any given lump to expand or collapse. As the lumps will be examined in a finite region of the plane, $\mathcal{M}$, they will collapse [22]. By defining a given 'volume' of lump, its size can be stabilised under numerical calculations using volume preserving gradient flow. Since the vacuum field is given by $\boldsymbol{\phi} = (0, 0, 1)$, the amount of lump could be defined using a volume density, υ such as

$$\upsilon = \frac{1}{2}(1 - \phi_3). \tag{2.3.4}$$

Lumps will be centred at points where $\boldsymbol{\phi} = (0, 0, -1)$, so $\upsilon = 1$ at the centre of a lump and

0 in the vacuum. The flow which alters the total volume, $V = \int_{\mathcal{M}} \upsilon \, d^2x$, can be defined, and will once again include a Lagrange multiplier term to impart the constraint $\boldsymbol{\phi} \cdot \boldsymbol{\phi} = 1$. The volume flow, $\boldsymbol{f}$ is

$$\frac{\partial \boldsymbol{\phi}}{\partial t_V} = -\left.\frac{\delta \upsilon}{\delta \boldsymbol{\phi}}\right|_{\boldsymbol{\phi}\cdot\boldsymbol{\phi}=1} = \frac{1}{2}\left(\boldsymbol{e}_3 - \phi_3 \boldsymbol{\phi}\right) \equiv \boldsymbol{f}, \tag{2.3.5}$$

where the Lagrange multiplier is again found using the Euler-Lagrange equation. The volume flow can be normalised, such that

$$\widehat{\boldsymbol{f}} = \frac{\left(\boldsymbol{e}_3 - \phi_3 \boldsymbol{\phi}\right)}{2\sqrt{\langle \boldsymbol{f} \cdot \boldsymbol{f} \rangle}}, \tag{2.3.6}$$

where

$$\langle \boldsymbol{f} \cdot \boldsymbol{f} \rangle = \frac{1}{V_{\mathcal{M}}} \int_{\mathcal{M}} \boldsymbol{f} \cdot \boldsymbol{f} \, d^2x = \frac{1}{4V_{\mathcal{M}}} \int_{\mathcal{M}} \left(1 - \phi_3^2\right) d^2x \equiv \|\boldsymbol{f}\|^2, \tag{2.3.7}$$

The volume preserving flow will then be

$$\begin{aligned}
\frac{\partial \boldsymbol{\phi}}{\partial t} \quad &= \boldsymbol{F} - \left\langle \widehat{\boldsymbol{f}} \cdot \boldsymbol{F} \right\rangle \widehat{\boldsymbol{f}} = \boldsymbol{F} - \frac{\langle \boldsymbol{f} \cdot \boldsymbol{F} \rangle}{\langle \boldsymbol{f} \cdot \boldsymbol{f} \rangle} \boldsymbol{f}, \qquad (2.3.8) \\
&\equiv \boldsymbol{F} - \left[\frac{1}{V_{\mathcal{M}}} \int_{\mathcal{M}} \left(\widehat{\boldsymbol{f}} \cdot \boldsymbol{F}\right) d^2x\right] \widehat{\boldsymbol{f}} = \boldsymbol{F} - \left[\frac{1}{V_{\mathcal{M}}} \int_{\mathcal{M}} \frac{\left(\boldsymbol{e}_3 \cdot \boldsymbol{F} - \phi_3 \boldsymbol{\phi} \cdot \boldsymbol{F}\right)}{2\sqrt{\langle \boldsymbol{f} \cdot \boldsymbol{f} \rangle}} d^2x\right] \widehat{\boldsymbol{f}}, \\
&= \boldsymbol{F} - \left[\frac{1}{2V_{\mathcal{M}} \|\boldsymbol{f}\|} \int_{\mathcal{M}} \left(\partial_i \partial_i \phi_3 + \left(\partial_i \boldsymbol{\phi} \cdot \partial_i \boldsymbol{\phi}\right) \phi_3\right) d^2x\right] \widehat{\boldsymbol{f}}, \\
&= \partial_i \partial_i \boldsymbol{\phi} + \left(\partial_i \boldsymbol{\phi} \cdot \partial_i \boldsymbol{\phi}\right) \boldsymbol{\phi} - \left(\boldsymbol{e}_3 - \phi_3 \boldsymbol{\phi}\right) \frac{\int_{\mathcal{M}} \left(\partial_i \partial_i \phi_3 + \left(\partial_i \boldsymbol{\phi} \cdot \partial_i \boldsymbol{\phi}\right) \phi_3\right) d^2x}{\int_{\mathcal{M}} \left(1 - \phi_3^2\right) d^2x},
\end{aligned}$$

since $\boldsymbol{\phi} \cdot \boldsymbol{F} = 0$. This can be expressed as a vector:

$$\frac{\partial \boldsymbol{\phi}}{\partial t} = \begin{pmatrix} \partial_i \partial_i \phi_1 + \left(\partial_i \boldsymbol{\phi} \cdot \partial_i \boldsymbol{\phi}\right) \phi_1 + A \phi_1 \phi_3 \\ \partial_i \partial_i \phi_2 + \left(\partial_i \boldsymbol{\phi} \cdot \partial_i \boldsymbol{\phi}\right) \phi_2 + A \phi_2 \phi_3 \\ \partial_i \partial_i \phi_3 + \left(\partial_i \boldsymbol{\phi} \cdot \partial_i \boldsymbol{\phi}\right) \phi_3 - A\left(1 - \phi_3^2\right) \end{pmatrix}, \tag{2.3.9}$$

where

$$A = \frac{\int_{\mathcal{M}} \left(\partial_i \partial_i \phi_3 + \left(\partial_i \boldsymbol{\phi} \cdot \partial_i \boldsymbol{\phi}\right) \phi_3\right) d^2x}{\int_{\mathcal{M}} \left(1 - \phi_3^2\right) d^2x}. \tag{2.3.10}$$

This flow will again will preserve the volume, V, since $\left\langle \boldsymbol{f}, \dot{\boldsymbol{\phi}} \right\rangle = 0$. Volume preserving flow will keep the field on the unit sphere as $\boldsymbol{\phi} \cdot \dot{\boldsymbol{\phi}} = 0$. It can also be easily shown that this flow will also minimise the energy to a local minima, as proved earlier (2.1.42).

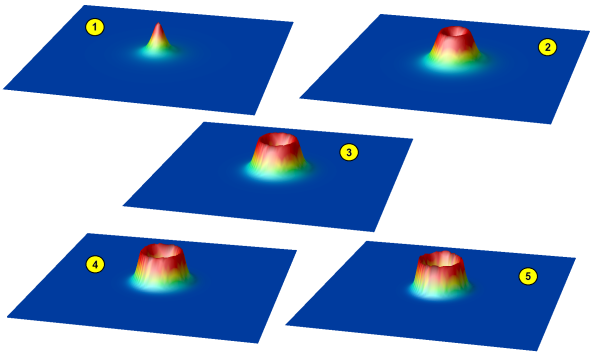

Figure 2.2: The energy (and charge) density plots for charge 1-5 lump solitons.

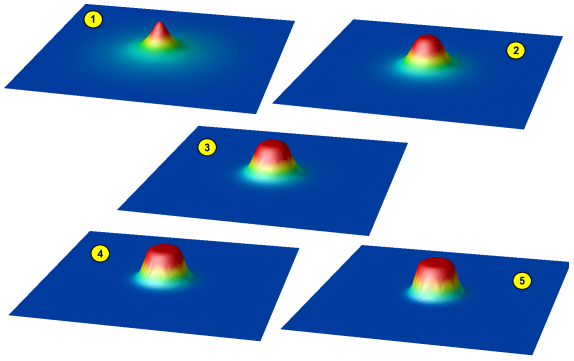

Figure 2.3: The volume density plots for charge 1-5 lump solitons.

The field will initially be set as a perturbed version of

$$\boldsymbol{\phi} = (\sin(f(\rho))\cos(\theta), \sin(f(\rho))\sin(\theta), \cos(f(\rho))), \tag{2.3.11}$$

with profile function, $f(\rho)$. Replacing θ by $N\theta$ will introduce a winding, and so lead to higher charged lumps, with integer topological charge N. The single lump solution in the $O(3)$ sigma model has a profile function of the form

$$f(\rho) = \cos^{-1}\left(\frac{\rho^2 - R^2}{\rho^2 + R^2}\right), \tag{2.3.12}$$

where R is the radius of the lump. R is defined as the boundary of the region containing half the total charge. R can be chosen arbitrarily, and sets the scale of the lump which will be preserved by utilising volume preserving flow. When the Bogomolny bound is attained, the energy is $2\pi N$. A profile function, $f(\rho)$, must also be defined. It must tend to π at the centre of the lump and to 0 as $\rho \to \infty$. An applicable function, used here is $f(\rho) = \pi e^{-A\rho}$, where A is a positive constant, large enough so that the vacuum is reached within the box and small enough so that the lump does not fall through the lattice.

The following simulations were carried out on a 201^2 lattice, with unit lattice spacing and $\Delta t = 0.1$. The volume initially alters by a thousandth of a percent then stays constant. Spacial derivatives are calculated using fourth order accurate finite difference methods and the flow is evolved using an explicit method with first order accuracy. The volume of a charge one lump from the initial conditions is $V = 1135$.

For charge $N = 1 \ldots 3$ lumps:

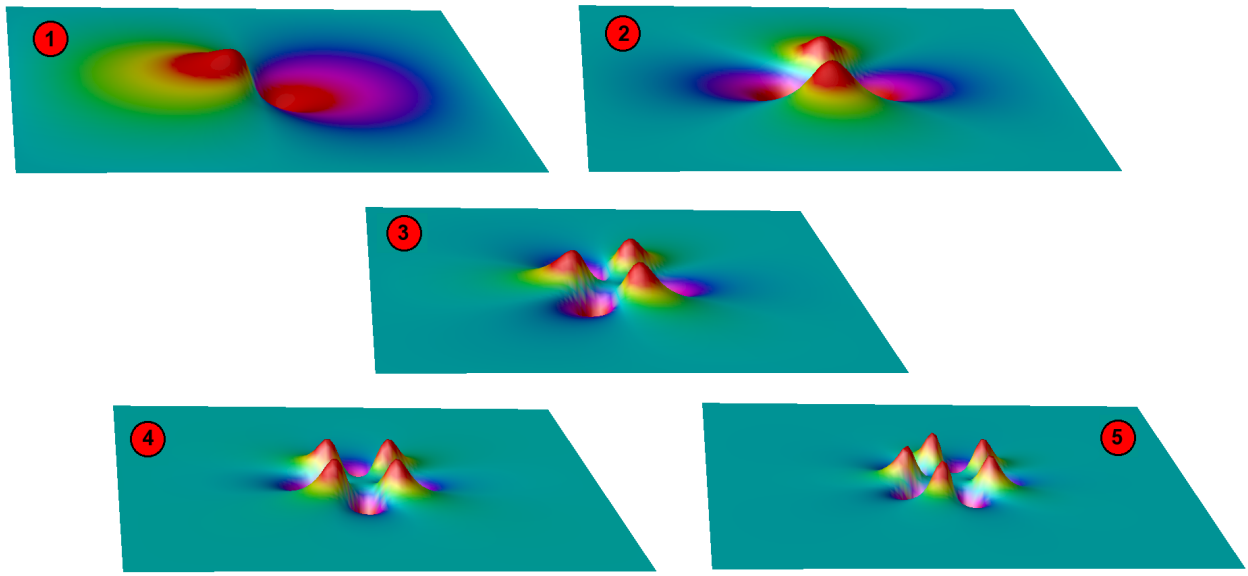

Figure 2.4: The form of ϕ_1 (and ϕ_2 up to a rotation) for charge 1-5 lump

	Charge 1	Charge 2	Charge 3
$E/2\pi$	1.01708	2.00161	3.00003
N	0.99992	1.99989	2.99957

Figures 2.2 and 2.3 show the energy (or charge) density and volume density for charge 1-5 lumps. Figure 2.4 shows a plot of the first field component ϕ_1, it is the same as ϕ_2 up to a rotation. The third component ϕ_3 has a form similar to that of the volume functions, with the red end corresponding $\phi_3 = -1$ and the blue part corresponding to $\phi_3 = +1$.

These results demonstrate the concept of calculating static soliton solutions in a scale invariant theory by using volume preserving gradient flow. The volume preservation stabilises the instability caused by putting them onto a lattice, where the boundary conditions imposed break the scale invariance. Volume preserving flow could be used in other scale invariant systems to find static solutions and such examples will be seen later.

Chapter 3

Double Bubbles and Domain Walls

Domain walls are kinks models embedded into higher spatial dimensions. They have an associated energy per unit length, i.e. a tension, and they separate distinct regions of vacua. Soap bubbles can be thought of in a similar way as distinct regions of air, separated by a soap film. This film will have an associated tension, which will attempt to minimise the area of the film. This chapter will investigate double bubbles using a network of domain walls, which is a minimal surface problem. Using a volume preserving flow to maintain the interior size of each bubble whilst still minimising the domain wall's energy should produce minimal surfaces for a given bubble configuration.

3.1 Double Bubbles

When a boundary exists between two media, enclosing a region of one medium, the enclosed region is called a bubble. Examples of bubbles are pockets of gaseous substances in a liquid, or a soap film enclosing a region of air from the surrounding air. In the latter case two or more bubbles may group together, with each of the bubbles remaining self-enclosed, without merging. The case of two such soap bubbles coming together and enclosing two separate volumes of gas are known as double bubbles [24].

3.1.1 Soap Bubbles as Minimal Surfaces

As the exterior of a soap bubble is made up of a given amount of oily film, stretched to enclose a given volume of air, the smaller the surface area of the film, the better. This is due to the tension in the film: the lower the surface area, the lower the tension, and so the lower the energy stored in the film. The pressure of the gas inside the bubble stops it collapsing and the tension in the film stops the bubble expanding. When these two are in balance the area of the film will be the minimum allowed to contain the volume of air. For a single bubble, the best you can do is a sphere - the minimal surface enclosing a given volume which has been mathematically known for quite some time [25]. Things become much more complicated as more bubbles are added, such that it took over a hundred years to prove that the double bubble (described below) is actually a minimal surface. The multi-bubble problem is referred to as the Kelvin Problem, in which one would ask what is the best structure for a foam of bubbles to form. It was proposed by Kelvin in 1887 to be the Kelvin Structure, which was bettered by Weaire and Phelan [26] in 1993 using computer simulations. The problem at hand here relates to the two bubble problem. For further information regarding soap bubbles, see for example, [27] or [28].

3.1.2 Double Bubbles and Periodic Spaces

As you begin to combine bubbles together they can share connecting walls which further minimises the surface area of the film required, and therefore energy, compared to the individual spherical bubbles. It has been explicitly proved that in two dimensions the best you can do is what is known as a standard planar double bubble [29] (see figure 3.1a). It consists of two regions, each bounded two circular arcs, one separating the two bubbles, and the other being the boundary to the exterior. These arcs meeting triple junctions, with each arc making an angle of 120^o with the others. The standard planar bubble has a line of symmetry between the upper an lower regions. The surfaces of revolutions generated by rotating about this axis in three dimensions gives the standard double bubble (see figure 3.1b). It has been proved to be the best configuration in three dimensions that, firstly if the volumes are equal [30], and then later for non-equal volumes [31]. This result has also been extended into higher dimensions [32]. The torus

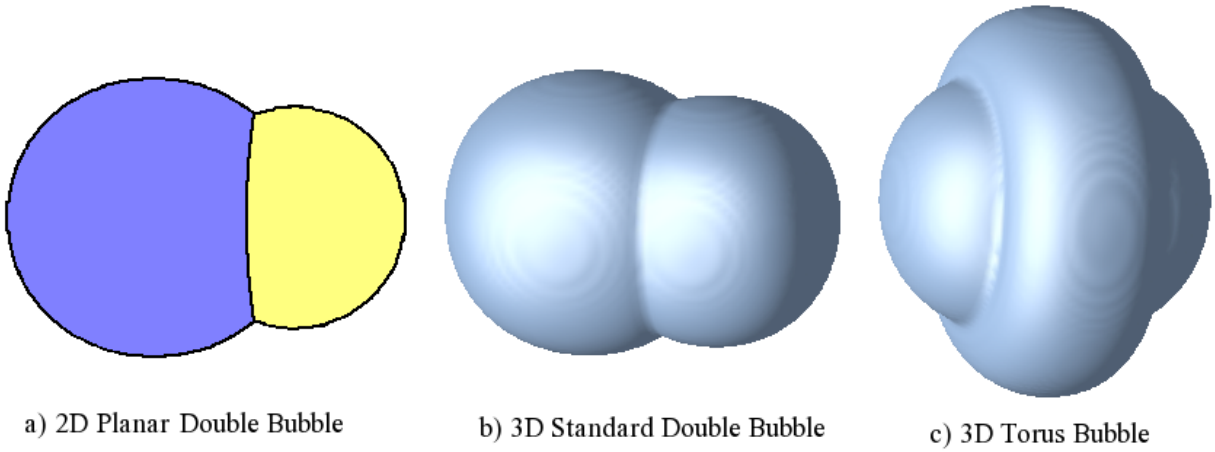

Figure 3.1: **a)** The standard planar double bubble, **b)** The standard double bubble in three dimensions, and **c)** The torus bubble, a possible surface minimiser, disproved in [31]

bubble (see figure 3.1c) was thought to be a candidate for a minimal surface, but it has been proved not to be the case [30, 31]. It is obvious that if the bubbles here were made from soap films, then the two bubbles sharing a wall would have a lower overall surface tension (and so lower energy) than if the two bubbles were separated. If these bubbles exist in flat space and they are far away from other objects, or the boundary, then the standard double bubble is all you get. Things become slightly more interesting if the space is compact (but still flat).

If the bubbles lie in a periodic space then there are a range of different perimeter minimising bubbles. There are four known minimisers on a generic flat two-torus (five, if the torus geometry is hexagonal) [33] and ten known minimisers on a generic flat three torus [34]. The minimum surfaces in these cases are dependent on the relative volumes enclosed by the bubbles and their size relative to the space. In each case the wall junctions meet in threes and at angles of 120^o to each other. More precisely, the curvature of the separating wall of the bubble is equal to the difference in curvature between the other two walls with which it meets.

3.1.3 Double Bubbles on the flat 2-Torus

The known minimisers for two bubbles on a flat, square two-torus can be found in figure 3.2. The perimeters of each of these minimisers can be explicitly calculated [33] for a given set of volumes. The minimiser for a given set of volumes can then be classified, which will be discussed later. The important information here is that the bubble perimeter has

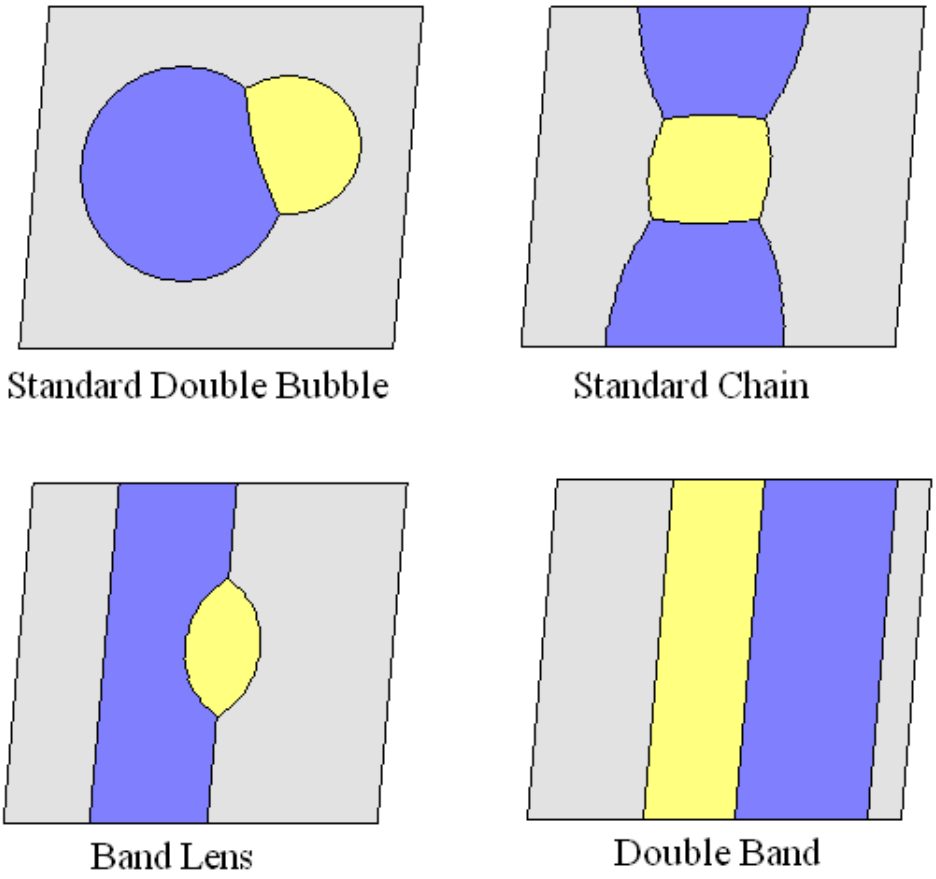

Figure 3.2: The surface minimisers on a flat two-torus.

three different parts constituting the boundaries between each of the three areas. If these boundaries meet then, to balance the tensions, the angle between each boundary at the point of intersection must be 120^o. The standard double bubble consists of three circular arcs which meet in threes balancing the curvature. The standard chain is symmetric about three geodesics which each pass through only two of the vacuum regions. The band lens consists of a two congruent circular arcs meeting at 120^o such that the lens can fit onto the space. The two vertices are connected by the shortest geodesic, which is congruent to the geodesic marking the other side of the band. The double band is bounded by three geodesics, with the shortest possible length on the compact surface. The geodesics are arranged next to each other such that the area of each bubble is correct. For further details relating to double bubbles on the flat two-torus, including explicit formulae for each bubble configuration, see [33]. The results of this paper are reproduced later using numerically computed energy minimisation of domain walls.

3.1.4 Triply Periodic Double Bubbles

As in two dimensions the only minimal surface available, if the two bubbles are well separated from any boundaries or obstacles, is the standard double bubble. If this space remains flat, but is also compact, then the number of minimisers increases. The known minimisers for two bubbles on a flat, square three-torus can be seen in figure 3.3. The structure of solutions is more complex than in two dimensions. They can be classified in a similar way. There are still junctions of the three boundaries but these junctions are now smooth, extended objects. The angle between each of the boundaries is again 120^o. Unlike in two dimensions the structure of which surface is a minimiser, and when, remains a conjecture. It is yet to be explicitly proven. Undergraduates at Millersville University [35] have also produced physical soap bubble versions of each minimiser although they only claim four of these to be stable. It remains possible that other minimisers may exist which could either replace any of the current minimisers or be added to the list. For further details relating to double bubbles on the flat three-torus see [34]. The minimisers, as well as other candidates in this paper, are reproduced later using numerically computed energy minimisation of domain walls. The full phase space of the minimisers is not verified, just the ability to reproduce the different configurations. Computation of the phase diagram for the three-torus is an open problem.

3.2 Using Domain Walls to find Minimal Surfaces

The surface of a soap bubble and a domain wall have much in common. By minimising the energy of a specific system containing different vacua, set up correctly with appropriate boundary conditions, the domain walls separating the different vacua will form minimal surfaces. Soap bubbles do this automatically.

Domain walls seem like a natural way to represent the film of a soap bubble. Work has previously been done using a ϕ^4 system to find quasicrystiline type minimal surface structures [36] and domain walls have also been used to investigate triply periodic minimal surfaces [37]. A soap film, enclosing a given amount of air, has an associated tension. This tension balances with the outward pressure associated with the enclosed air. The effect of this is that the film has a given energy per unit area and so it will form a surface

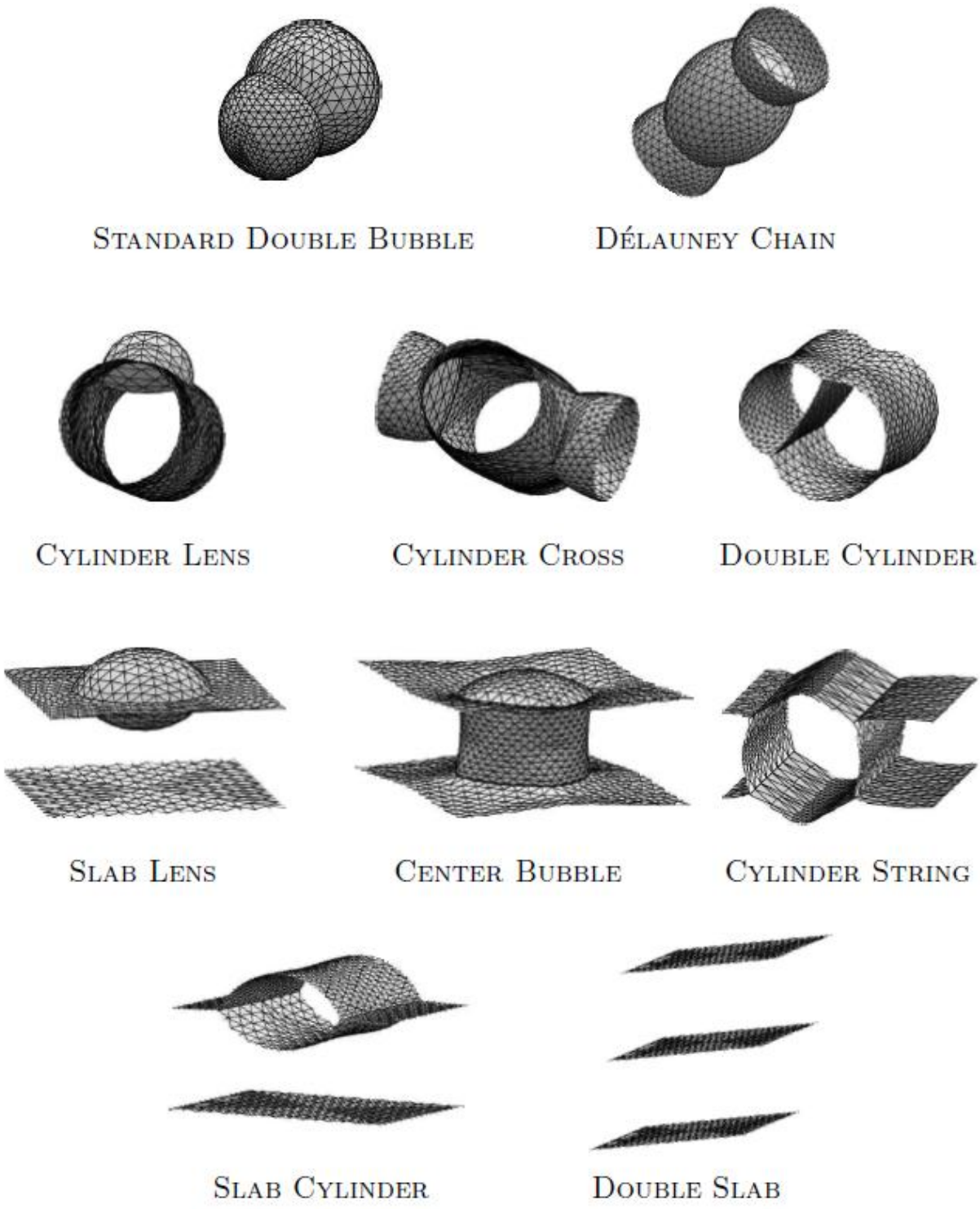

Figure 3.3: The known surface minimisers on a flat, square three-torus. Figure taken from [34].

with the minimal area to enclose the volume of air. Domain walls in three dimensions would also have a tension, i.e. an energy per unit area of wall. If a domain wall formed a closed surface around a given vacuum, and the amount of vacuum cannot change, then

minimising the energy of the domain wall will minimise the surface area in a similar way as with the soap bubbles. This concept also works with three domain walls enclosing two volumes. To balance the tensions in each wall they must intersect in threes, at an angle of 120^o, as with the double bubbles introduced earlier. Clearly, in order to produce double bubbles using domain walls, two ingredients are necessary

- A METHOD OF MINIMISING THE ENERGY OF A DOMAIN WALL CONFIGURATION - By minimising the energy of a correctly set up configuration of domain walls the surface area of the bubbles will reduce, hopefully into a minimal surface

- A METHOD OF FIXING THE VOLUMES OF THE BUBBLES - The energy minimisation would attempt to reduce the system into a single vacuum, therefore some method of fixing the amount of each vacuum needs to be applied in order to find the minimal surfaces for these fixed volumes

Given these ingredients, a network of domain walls could be used to model double bubbles. In the limit that the domain walls reduce towards delta functions in relation to the volumes of vacua, the system will become a minimal surface. The limit in which the walls become negligible compared to the much larger volumes of vacua will be referred to as the thin wall limit.

A problem of this type can be solved by applying volume preserving flow as a method of energy minimisation. The method is the same as set out previously and is detailed below. It can also be solved by adding a large value to the energy depending on the difference between the current volume and the desired volume. This will be referred to as the penalty function method and will be introduced after the discussion below.

3.2.1 Volume Preserving Flow

The field theory of interest here will be ϕ^6 theory, introduced earlier, which is from the bosonic sector of the Wess-Zumino model with one complex scalar field. As the domain walls will form the boundaries of the double bubbles a field theory with at least three independent vacua is needed, one for each of the bubbles, and one for the exterior. It is also important that domain walls linking the vacua all have the same tension so that

no single domain wall will be preferred and all walls will be subject to the same energy minimisation restraints. These features can easily be seen in figure 1.2 for ϕ^6 kinks. Another important detail about this theory relates to surface junctions. It has been noted earlier that in both two, and three dimensions, individual boundary sections of the bubbles (which will relate to different domain walls in this method) intersect only in threes and that the angle between each boundary at these triple junctions is 120^o. This junction angle occurs for ϕ^6 domain wall junctions, as shown numerically from networks of junctions, connected by domain walls, creating a tiling of the plane [14]. It occurs as all three domain walls have the same tension.

Gradient Flow

For static solutions of the field theory in question, the local energy density is given by

$$\mathcal{E} = \frac{1}{4}\left|\partial_i\phi\right|^2 + \left|1-\phi^3\right|^2, \tag{3.2.1}$$

where the potential and superpotential are

$$U(\phi) = \left|\frac{dW}{d\phi}\right|^2 = \left|1-\phi^3\right|^2, \quad \text{and} \quad W = \phi - \frac{\phi^4}{4}. \tag{3.2.2}$$

There are three vacua, ϕ_i, $i=1\ldots3$;

$$\phi_1 = -\frac{1}{2} + \frac{\sqrt{3}}{2}i, \quad \phi_2 = -\frac{1}{2} - \frac{\sqrt{3}}{2}i, \quad \text{and} \quad \phi_3 = 1. \tag{3.2.3}$$

These domain walls will have a thickness $\mathcal{O}(1)$. The thickness can be reduced to $\mathcal{O}(\epsilon)$ if

$$\mathcal{E} = \frac{1}{4}\left|\partial_i\phi\right|^2 + \frac{1}{\epsilon^2}\left|1-\phi^3\right|^2. \tag{3.2.4}$$

The thin wall limit would then be $\epsilon \to 0$, but as the regularity of this limit would also have to be addressed, it is simpler to consider the other scales, such as taking the torus length to be $\mathcal{O}(1/\epsilon)$.

The tension of domain walls in this theory can be found by evaluating kinks in the $1+1$ dimensional theory. If the field lies in separate vacua at $x=+\infty$ and $x=-\infty$, say ϕ_i and ϕ_j, $i\neq j$, then the kink that would attain the Bogomolny bound for this system

would have an energy

$$E = \int_{-\infty}^{\infty} \mathcal{E}\, dx = |W(\phi_i) - W(\phi_j)| = \frac{3\sqrt{3}}{4}. \tag{3.2.5}$$

So the domain walls will have a tension $\mu = 3\sqrt{3}/4$. A network of domain walls in two(three) spatial dimensions will then have a perimeter(surface area) E/μ, where the tension is the energy per unit length(area).

Static solutions will obey the Euler-Lagrange equations of (3.2.1), such that

$$\nabla^2\phi = -12\bar{\phi}^2\left(1-\phi^3\right). \tag{3.2.6}$$

The gradient flow equation for (3.2.1) with time parameter t_0 is

$$\partial_{t_0}\phi = -\frac{\delta\mathcal{E}}{\delta\bar{\phi}} = \frac{1}{4}\nabla^2\phi + 3\bar{\phi}^2\left(1-\phi^3\right) \equiv F. \tag{3.2.7}$$

A network of domain walls contained in a space where the entire boundary is a single vacuum will be reduced to zero length under this flow. Two methods of preserving 'volumes' of given vacua will be discussed below, after suitable methods of counting each volume are introduced.

Volumes

A possible method of counting bubble volumes was introduced previously in the circular perimeter ϕ^4 example. It counts one when ϕ is in the given vacuum and zero when it is in another vacuum. If the three vacua are labelled (ϕ_1, ϕ_2, ϕ_3), the three roots of unity, then $\upsilon_i(\phi_j) = \delta_{ij}$, which is satisfied if

$$\upsilon_i(\phi) = \frac{|\phi-\phi_j|^2\,|\phi-\phi_k|^2}{|\phi_i-\phi_j|^2\,|\phi_i-\phi_k|^2}, \tag{3.2.8}$$

where i, j, k are three distinct elements of $\{1, 2, 3\}$ and $|\phi_i - \phi_j| = \sqrt{3}$. Since the space in question will be periodic, the total volume will be given by

$$V_i = \int_{T^d} \upsilon_i\, d^d x, \tag{3.2.9}$$

and the flat, regular torus will have a total volume of V_T. In the thin wall limit,

$$V_1 + V_2 + V_3 \to V_T. \tag{3.2.10}$$

These volume functions are not ideal since, not only will they count the vacua in question, but also all three domain walls. It makes sense to include the domain walls directly linked to the vacua in a volume count but not the third, unconnected, wall. In the thin wall limit this would not be an issue but, as the walls will always have a thickness for numerical calculations, this could introduce an error. This error could be reduced by raising the volume functions above to a higher power. It is possible to entirely remove this error by utilising that domain walls follow a straight path in the W-plane - as seen in figure 1.2.

In the W-plane, the three vacua $W(\phi_i)$ are connected by three straight lines, W_{ij}, where

$$W(\phi_1) = -\frac{3}{8}\left(1-\sqrt{3}i\right), \quad W(\phi_2) = -\frac{3}{8}\left(1+\sqrt{3}i\right), \quad \text{and} \quad W(\phi_3) = \frac{3}{4}, \tag{3.2.11}$$

and the domain walls lie along the W_{ij} lines, given by

$$W_{12} : \Re(W) = \frac{3}{8},\ W_{23} : \Re(W) - \sqrt{3}\Im(W) = \frac{3}{4},\ W_{31} : \Re(W) + \sqrt{3}\Im(W) = \frac{3}{4}. \tag{3.2.12}$$

Choosing $\upsilon_i(\phi_i) = 1$ and $\upsilon_i(W_{jk}) = 0$ gives

$$\begin{aligned}
\upsilon_1 &= \frac{\left|4\Re(W) - 4\sqrt{3}\Im(W) - 3\right|^2}{\left|4\Re(W(\phi_1)) - 4\sqrt{3}\Im(W(\phi_1)) - 3\right|^2} = \frac{1}{9^2}\left|4\Re(W) - 4\sqrt{3}\Im(W) - 3\right|^2 \\
&= \frac{1}{81}\left|2\left(1-\sqrt{3}i\right)W + 2\left(1+\sqrt{3}i\right)\overline{W} - 3\right|^2, \\
\upsilon_2 &= \frac{\left|4\Re(W) + 4\sqrt{3}\Im(W) - 3\right|^2}{\left|4\Re(W(\phi_2)) + 4\sqrt{3}\Im(W(\phi_2)) - 3\right|^2} = \frac{1}{9^2}\left|4\Re(W) + 4\sqrt{3}\Im(W) - 3\right|^2 \\
&= \frac{1}{81}\left|2\left(1+\sqrt{3}i\right)W + 2\left(1-\sqrt{3}i\right)\overline{W} - 3\right|^2, \\
\upsilon_3 &= \frac{|8\Re(W) - 3|^2}{|8\Re(W(\phi_3)) - 3|^2} = \frac{1}{9^2}|8\Re(W) - 3|^2 = \frac{1}{81}\left|4W + 4\overline{W} - 3\right|^2,
\end{aligned} \tag{3.2.13}$$

where

$$\Re(W) = \frac{W+\overline{W}}{2} \qquad \text{and} \qquad \Im(W) = \frac{W-\overline{W}}{2i}. \tag{3.2.14}$$

The gradient flow equations for (3.2.13) with time parameters t_i follow from

$$\frac{\partial \upsilon_1}{\partial \overline{W}} = \frac{2}{81}\left(1-\sqrt{3}i\right)\left[2\left(1+\sqrt{3}i\right)W+2\left(1-\sqrt{3}i\right)\overline{W}-3\right], \tag{3.2.15}$$

$$\frac{\partial \upsilon_2}{\partial \overline{W}} = \frac{2}{81}\left(1+\sqrt{3}i\right)\left[2\left(1-\sqrt{3}i\right)W+2\left(1+\sqrt{3}i\right)\overline{W}-3\right]. \tag{3.2.16}$$

As preserving V_1 and V_2 will automatically preserve V_3, no flow equations for υ_3 is required. W, and it is conjugate differential are then,

$$W = \phi - \frac{\phi^4}{4}, \quad \text{and} \quad \frac{\partial \overline{W}}{\partial \bar{\phi}} = 1-\bar{\phi}^3. \tag{3.2.17}$$

The flow equations for the two volume functions are then

$$\begin{aligned} f_1 = \partial_{t_1}\phi &= -\frac{\partial \upsilon_1}{\partial \bar{\phi}} = -\frac{\partial \upsilon_1}{\partial \overline{W}}\frac{\partial \overline{W}}{\partial \bar{\phi}} \qquad (3.2.18)\\ &= \frac{2}{9^2}\left(1-\sqrt{3}i\right)\left(1-\bar{\phi}^3\right)\left[3-2\left(1+\sqrt{3}i\right)W-2\left(1-\sqrt{3}i\right)\overline{W}\right], \\ f_2 = \partial_{t_2}\phi &= -\frac{\partial \upsilon_2}{\partial \bar{\phi}} = -\frac{\partial \upsilon_2}{\partial \overline{W}}\frac{\partial \overline{W}}{\partial \bar{\phi}} \qquad (3.2.19)\\ &= \frac{2}{9^2}\left(1+\sqrt{3}i\right)\left(1-\bar{\phi}^3\right)\left[3-2\left(1-\sqrt{3}i\right)W-2\left(1+\sqrt{3}i\right)\overline{W}\right]. \end{aligned}$$

These will be the volume functions taken in the numerical calculations presented later in this chapter, unless stated otherwise.

Another choice of volume functions that count one when the field is in a given vacua and zero along the non-connecting domain wall is to take

$$\upsilon_i(\phi) = \left(\frac{\Im\left[\left(W(\phi)-W(\phi_k)\right)\left(\overline{W(\phi_j)}-\overline{W(\phi_k)}\right)\right]}{\Im\left[\left(W(\phi_i)-W(\phi_k)\right)\left(\overline{W(\phi_j)}-\overline{W(\phi_k)}\right)\right]}\right)^2. \tag{3.2.20}$$

The volume density is zero in either of the other two vacua ϕ_j, $i \neq j$. Along the domain wall W_{jk}, the equation of this straight line through $W(\phi_j)$ and $W(\phi_k)$ can be written as

$$\frac{W-W(\phi_k)}{W(\phi_j)-W(\phi_k)} = \frac{\overline{W}-\overline{W(\phi_k)}}{\overline{W(\phi_j)}-\overline{W(\phi_k)}}, \tag{3.2.21}$$

substituting into (3.2.20), it can easily be seen that

$$\Im\left[\left(W(\phi)-W(\phi_k)\right)\left(\overline{W(\phi_j)}-\overline{W(\phi_k)}\right)\right] = \Im\left[\left(\overline{W(\phi)}-\overline{W(\phi_k)}\right)\left(W(\phi_j)-W(\phi_k)\right)\right], \tag{3.2.22}$$

i.e. $\Im[a] = \Im[\overline{a}] = 0$, meaning that the volume density, $\upsilon_i(\phi)$, counts zero along the W_{jk} domain wall. As $\upsilon_i(\phi) = 0$ anywhere along W_{jk}, it must also count zero when the field is in either vacuum at either end of the wall. Also note that, for any arrangement of vacua in (3.2.20),

$$\Im\left[(W(\phi_i) - W(\phi_k))\left(\overline{W(\phi_j)} - \overline{W(\phi_k)}\right)\right]^2 = \frac{2187}{1024} \equiv \chi. \tag{3.2.23}$$

The flow of these volume functions, with $W_i = W(\phi_i)$, will follow from

$$\frac{\partial \upsilon_i}{\partial \overline{W}} = 2\chi \overline{W_k}\,(W_j - W_k)\left[\left(\overline{W} - \overline{W}_k\right)(W_j - W_k) - (W - W_k)\left(\overline{W_j} - \overline{W_k}\right)\right]. \tag{3.2.24}$$

Simply substituting in the relevant parts will give the volume flows:

$$f_i = \partial_{t_i}\phi = -\frac{\partial \upsilon_i}{\partial \bar{\phi}} = -\frac{\partial \upsilon_i}{\partial \overline{W}}\frac{\partial \overline{W}}{\partial \bar{\phi}}. \tag{3.2.25}$$

This particular volume choice is useful as it allows for all three volume functions to be easily written in a single equation.

Volume Preserving Flow

Given the volume flow (3.2.18), (3.2.19) or (3.2.25), and the energy flow (3.2.7), a volume preserving flow for this system can be constructed. The normalised volume reducing flow for the first volume, $\hat{f}_1$ is given by the following, though it is not illuminating to give the full expressions,

$$\hat{f}_1 = \frac{f_1}{\|f_1\|}, \quad \text{where} \quad \|f_i\| = \sqrt{\langle f_i, f_i\rangle} = \left(\int \overline{f_i} f_i \, d^d x\right)^{\frac{1}{2}}. \tag{3.2.26}$$

The projection of the f_2 onto $\hat{f}_1$, i.e. the inner product of the two directions, is

$$\left\langle \hat{f}_1, f_2 \right\rangle = \frac{\int \overline{\hat{f}_1} f_2 \, d^d x}{\int d^d x}, \tag{3.2.27}$$

using this, a flow of υ_2 that is orthonormal to $\hat{f}_1$ can be defined

$$\tilde{f}_2 = f_2 - \left\langle \hat{f}_1, f_2 \right\rangle \hat{f}_1, \quad \Longrightarrow \quad \hat{f}_2 = \frac{\tilde{f}_2}{\|\tilde{f}_2\|}. \tag{3.2.28}$$

The volume preserving flow equation for this system, with a flow time, t is

$$\dot{\phi} = F - \left\langle \hat{f}_1, F \right\rangle \hat{f}_1 - \left\langle \hat{f}_2, F \right\rangle \hat{f}_2, \tag{3.2.29}$$

where

$$\left\langle \hat{f}_i, F \right\rangle = \frac{\int \overline{\hat{f}_i} F \, d^d x}{\int d^d x}. \tag{3.2.30}$$

The full equation can be found by substituting in the appropriate equations for f_1, f_2 (3.2.18), (3.2.19) or (3.2.25) and F, (3.2.7) respectively.

3.2.2 Penalty Function

Volume preserving flow is an elegant method for finding local minima subject to global constraints. In some cases the minimisation landscape may contain many local minima in the direction of volume preserving flow, or at least, non-trivial zero modes. Finding the global minima in a landscape such as this can be difficult as only a limited number of initial conditions will minimise to the global minima. One such example in the framework of double bubbles is to imagine two spherical bubbles, one entirely contained within the other in $\mathbb{R}^3$. Moving the smaller bubble in any direction will be not reduce the area unless the two domain walls become close enough. This configuration is clearly a stationary point of the area functional.

Another method of constraining the volumes during energy minimisation is to add an energy penalty to the field theory. The additional amount of energy relates to how close the actual volumes are to the desired volumes. This would alter the field theory in question, where the energy would then be given by

$$E = E_{kink} + E_{penalty}, \tag{3.2.31}$$

where E_{kink} is the same as (3.2.1) and $E_{penalty}$ is the penalty function, given by

$$E_{penalty} = \lambda\{(V_1 - V_1^*)^2 + (V_2 - V_2^*)^2\}. \tag{3.2.32}$$

V_i^* denotes the desired volumes, with V_i being the actual volumes. λ is a large positive constant $\lambda \gg 1$. The limit $\lambda \to \infty$ forces $V_i \to V_i^*$, but the minimisation will favour preserving the volumes over forming domain walls and minimising their energy. To apply this numerically, a finite λ should be chosen, which will keep the volumes to within a given accuracy allowing the domain walls to be formed and their energy to be correctly minimised. Gradient flow can be applied directly to (3.2.31), and given an appropriate

choice of λ, the volumes will become close to the desired values. If the volumes are close enough (λ dependent), then E_{kink} (3.2.1) will dominate and the energy minimisation will find minimal surfaces relating to the given volumes. The gradient flow equations F_λ, for (3.2.31) are

$$F_\lambda = -\frac{\delta \mathcal{E}}{\delta \bar{\phi}} = -\frac{1}{4}\nabla^2\phi - 3\bar{\phi}^2(1-\phi^3) + 2\lambda\left[(V_1 - V_1^*)\frac{\partial \upsilon_1}{\partial \bar{\phi}} + (V_2 - V_2^*)\frac{\partial \upsilon_2}{\partial \bar{\phi}}\right], \quad (3.2.33)$$

where V_i are found from either (3.2.13) or (3.2.20), with

$$\frac{\partial \upsilon_i}{\partial \bar{\phi}} = -f_i, \quad (3.2.34)$$

i.e. either (3.2.18), (3.2.19) or (3.2.25). It is also possible to isolate λ dependence to each volume individually. Splitting the λ dependence could be useful when the two volumes are quite different, such as if one bubble were small, there would be more need to get that volume correct than the much larger one.

The penalty function method is much less elegant than the volume preserving flow as it requires careful choice of λ. The method does not exactly solve the same problem, except in the limit $V_i \to V_i^*$. This property can be useful, and in fact it will be used later. Non-trivial zero modes of the area functional for two and three dimensional configurations, restricted to volume preserving flow, can be overcome by utilising the penalty function method greatly reduces the computational power needed to find those minimal surfaces. Details of when this method is used will be included, where appropriate, otherwise volume preserving flow will be used to find solutions.

3.3 Two Dimensional Double Bubbles

All the ingredients for using domain walls to produce minimal surfaces have now been introduced. Some information regarding the links between soap bubbles and minimal surfaces has been given, as well as details of what double bubbles are, and how they behave in periodic spaces for certain cases. The first case to be examined here is the case of a two-dimensional flat space. Chapter 2 has discussed some details relating to a single bubble in two dimensional, flat infinite space, where the circle is formed, with the same perimeter as would be expected. The correct perimeter can be found using a penalty

function to preserve the volume, and using the volume preserving technique.

The required mathematics that will describe the domain walls has also been introduced. The phase diagram for double bubbles on a flat two-torus will be reproduced using volume preserving flow, or the penalty function method, where necessary. Some problems and limitations of the techniques will be discussed and possible future work suggested.

3.3.1 Numerical Details

To be able to compute these equations and evolve the system there are some numerical tools that are needed. There are many different techniques available for numerically differentiating and integrating, as well as finding roots, interpolating data and finding points of intersection. For further details, consult [19–21].

Calculations in this section utilise a square lattice, usually with 401^2 lattice sites. The lattice spacing is $\Delta x = 0.2$, meaning that the lattice size is 80. 10-20 lattice points cover each kink. The flow will be evolved using an explicit method with first order accuracy with a time step of $\Delta t = 0.1\Delta x^2$. The derivatives are calculated using a finite difference method with second order accuracy. There are stability issues that can arise if the penalty function term in the gradient flow becomes large. This can happen when the difference between the calculated volume and the desired volume $V_i - V_i^*$ becomes large. The volumes will be normalised in the results presented, such that $V_T = 1$ for continuity.

3.3.2 Minimal Surfaces

The minimal surfaces, found on a two-dimensional flat torus, were introduced earlier. Figure 3.2 showed the four different possible minimisers. In fact, each of these is the minimal surface for a certain ratio of the different volumes $V_1 : V_2 : V_3$. Since the third volume is fixed by the other two if the torus volume is known, the minimiser for each pair of volumes, (V_1, V_2), can be illustrated using a phase space plot. This plot has previously been calculated [33], where the phase diagram produced can be seen in figure 3.4a). The phase diagram will be discussed in detail later, first the minimisers must be found using domain walls.

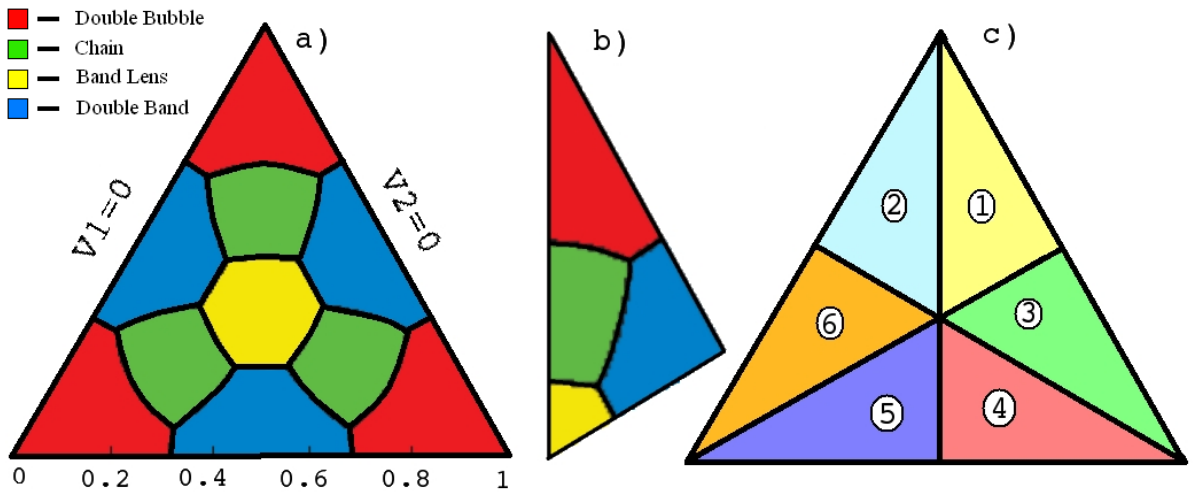

Figure 3.4: **a)** The phase plot taken from [33] for the square torus, **b)** The part of this phase plot which is unique (the rest of the plot can be found via symmetry) and **c)** The six different regions of the plot, all related to region one by a symmetry transformation, which relates to the fact that the volume labels are arbitrary, and so interchangeable.

The mathematics and numerical techniques outlined previously can be used to compute minimal surfaces formed by static domain wall configurations, both in flat space and on a torus. It has been proved that, in flat space, the least-perimeter way to enclose two separate areas is the standard, planar double bubble (see figure 3.1a)). If the domain wall system is to find minimal surfaces, the standard double bubble should be found. The critical factor is the initial conditions imposed. Remember that the three vacua are located at the three cube roots of unity;

$$\phi_1 = -\frac{1}{2} + \frac{\sqrt{3}}{2}i\,, \quad \phi_2 = -\frac{1}{2} - \frac{\sqrt{3}}{2}i \quad \text{and} \quad \phi_3 = 1. \tag{3.3.1}$$

If ϕ_3 is the background vacuum, and the boundary is fixed in this vacuum, then the regions of the other two vacua must be adjacent, so that a domain wall can form between them, as well as the walls forming with the background vacuum. If they are isolated two individual circular bubbles will form and the solution will be static. In all the starting conditions used each volume will be placed purely in the vacuum required. With these conditions the derivatives are initially very large, but they are soon smoothed out as the domain walls form up, which happens in a matter of a few time steps. The energy minimisation can be done, using either technique previously outlined, with very similar results. The starting and ending field configurations can be found in the figure 3.5. In the case of two bubbles with equal volumes (which is true here) the domain walls between the

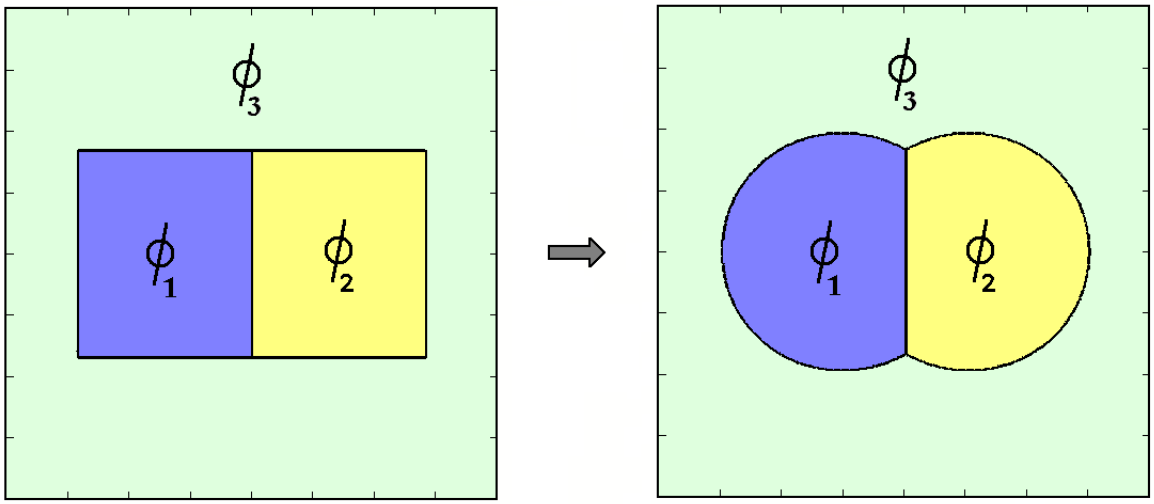

Figure 3.5: The starting, **a)** and ending, **b)** field configurations on the lattice. The volumes are $V_1 = V_2 = 0.15$. The boundary is set in vacua 3 and the edges of the bubble correspond to the midpoints of the domain walls, i.e. half way between either vacuum.

background and the volumes will form into part of the perimeter of a circle. The domain wall between the two volumes forms a straight line. These three walls meet at two points, at the top and bottom of the domain wall separating the two bubbles. Close to this triple point the field will not lie in any of the vacua, or along a domain wall, it will tend towards the midpoint of the three vacua in field space. On the lattice, this can be seen in figure 3.6a), and also notice on the energy density plot, figure 3.6b), where the energy density dies off towards the triple point. Figure 3.6c) shows the domain walls as the contours of the plot (note the error in the volume counting). This extra counting occurs as volume measures (3.2.8) (like that used in chapter 2 for one bubble modelled using ϕ^4 theory) have been used in this example. It can be seen in the plot of the first volume density, figure 3.6d). Further calculations will utilise volume functions like (3.2.20). The volumes of these bubbles are $V_1 = V_2 = 0.15$. Figure 3.6e) shows the midpoint locations of the three walls (half way between the two vacua in either ϕ space or W space), along with the two circles which the walls should follow, according to the formulae found in [33]. These midpoints will be used to define the boundary of each bubble in this context, i.e. the minimal surfaces. The final plot, figure 3.6f) shows the evolution of the bubbles perimeter over time. The energy decreases quickly at the start as the domain walls form, the corners are smoothed out, and the curvature at the triple point is balanced out. The process then slows down as the walls curve round to form circular arcs.

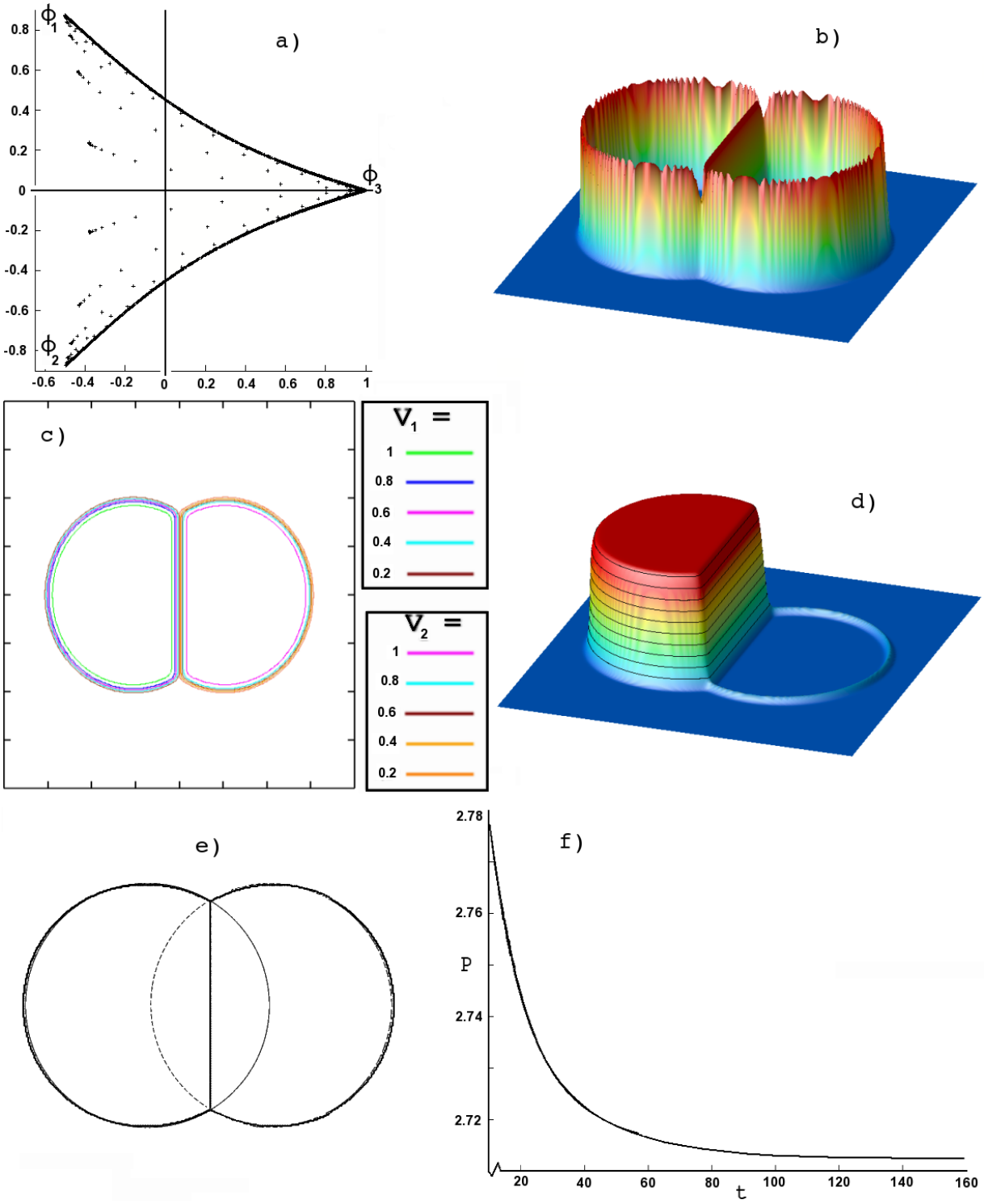

Figure 3.6: **a)** The plot of the field values in the complex plane. **b)** Plot of the final energy density configuration as a function of x and y. **c)** A contour plot of the volume densities, the key on the right specifies the values of each contour. **d)** Plot of the density of volume one. **e)** Plot of the mid-points of the domain walls overlaying two circles. The bubbles and the circles should line up, if the surface is a minimal one. **f)** Plot of the perimeter of the bubble against time. The final value of the perimeter is ~ 2.71, where as the actual perimeter should be 2.70. This is a reasonable estimate as it is within about half a percent of the expected value.

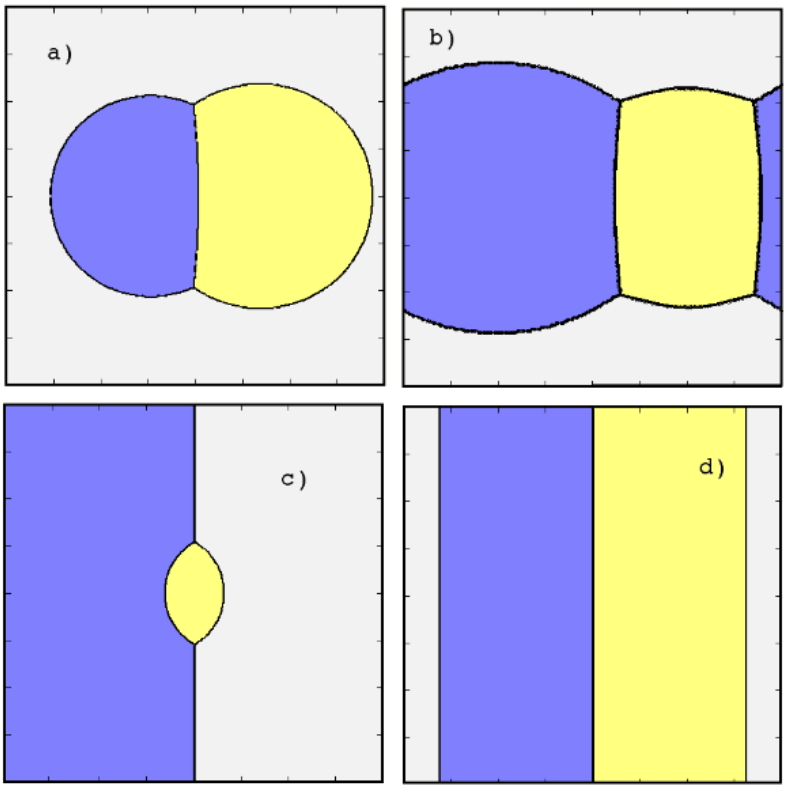

Figure 3.7: The four minimisers on the two-torus with the volumes (V_1, V_2) given, the standard double bubble $(0.2, 0.3)$ **a)**, the standard chain $(0.4, 0.2)$ **b)**, the band lens $(0.45, 0.5)$ **c)** and the double band $(0.4, 0.4)$ **d)**.

If the configuration space is periodic then the standard double bubble may not be the best solution. To find which is the best solution of a given pair of volumes the perimeter of each minimiser must be calculated. The four minimisers can be seen in figure 3.7, which also gives the relative volumes of each bubble. Volume preserving flow was used to find standard double bubble, band lens and double band solutions. Chain solutions were found using penalty function minimisation, for reasons discussed later. The details of each system can be better understood by examining figure 3.8. It gives a range of different plots, relating to different aspects of the solutions, for each minimiser. The field in the complex plane, figure 3.8a), deviates away from the vacua and domain walls as the triple point is approached. For the bubble solution, the vertices represent the field in the vacua (i.e. the majority of the points). The domain walls between the two bubbles and the background are picked out by a number of points. However, the domain wall between the two volumes is not as well defined. As the field approaches the triple point the field values are drawn towards the centre of the three vacua, eventually getting closer to the background vacuum at the wall junction. The same effect takes place with the chain, this time there are four junctions. These are simply two copies of the junction pairs seen with the bubble solutions. In the case of the band lens, the effect occurs

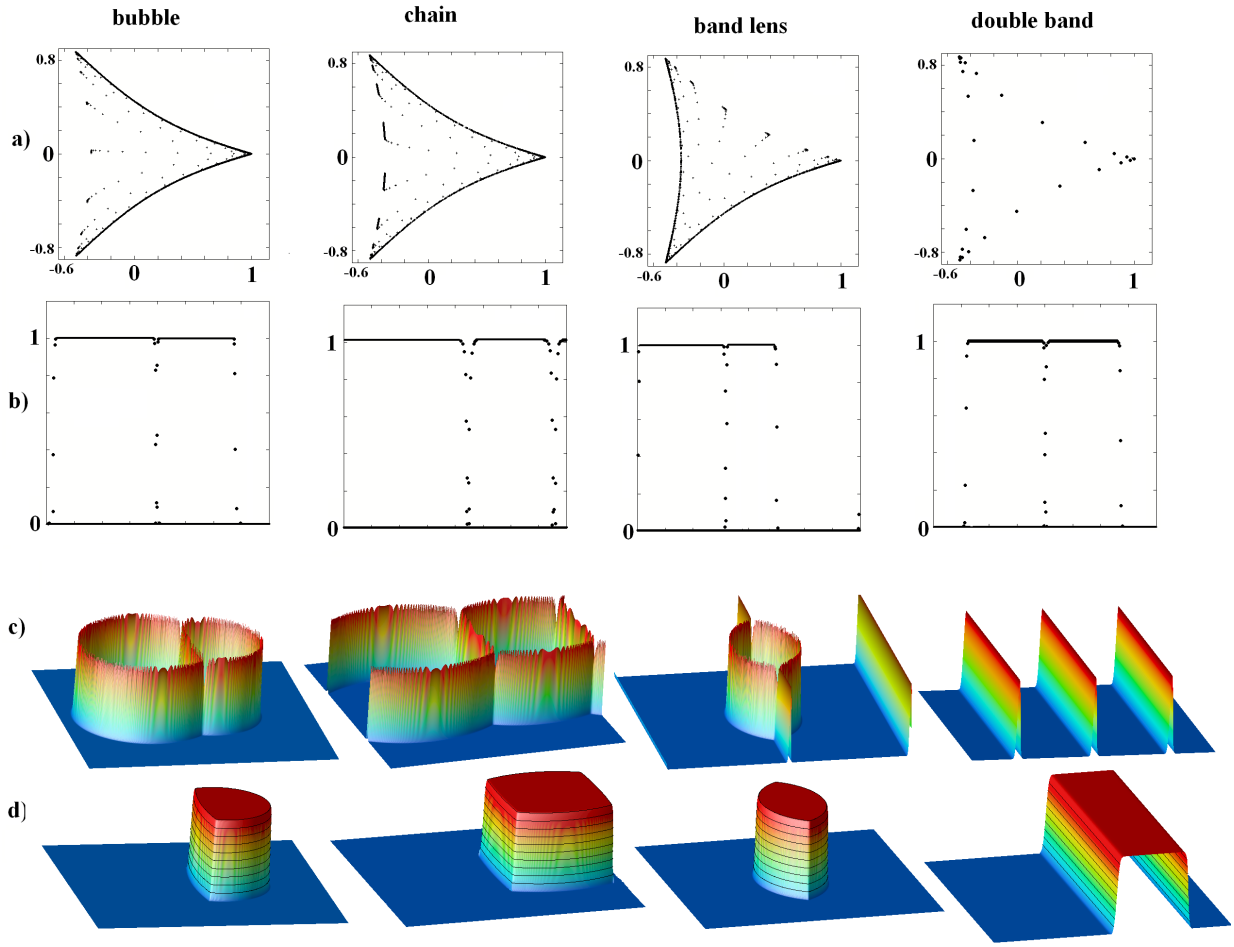

Figure 3.8: A range of plots for the standard double bubble $V_1 = 0.2, V_2 = 0.1, P = 2.14$, standard chain $V_1 = 0.3, V_2 = 0.2, P = 2.88$, band lens $V_1 = 0.45, V_2 = 0.1, P = 2.70$ and the double band $V_1 = 0.33, V_2 = 0.33, P = 2.99$, where P is the perimeter. **a)** The plot of the field values in the complex plane. **b)** Cross sectional plots of the volume densities. **c)** Plot of the energy density, showing the position and thickness of the domain walls, as well as their general behaviour. **d)** Plot of the volume two's density.

into another vacuum, since it is the wall between vacua one and three that are in the equivalent junction orientation as with the double bubble. For the bands, there are no junctions, so the domain walls are picked out entirely, albeit there are a limited number of lattice points covering the wall. The domain walls themselves are best seen in the profile pictures, figure 3.8b). They show the profile of the volume functions. In each case the outer walls are easy to spot and show the coverage of the domain wall. It is also noticeable where the two bubbles meet, that the volumes overlap. This is due to the counting of the domain wall in the volume function. In both cases the volume component dies off as the field moves towards the other vacua. The best way to pick out the structure of the bubbles is to look at the energy density. Since all the energy of the field is contained in the domain walls, and the midpoint has the greatest energy density, the middle of each

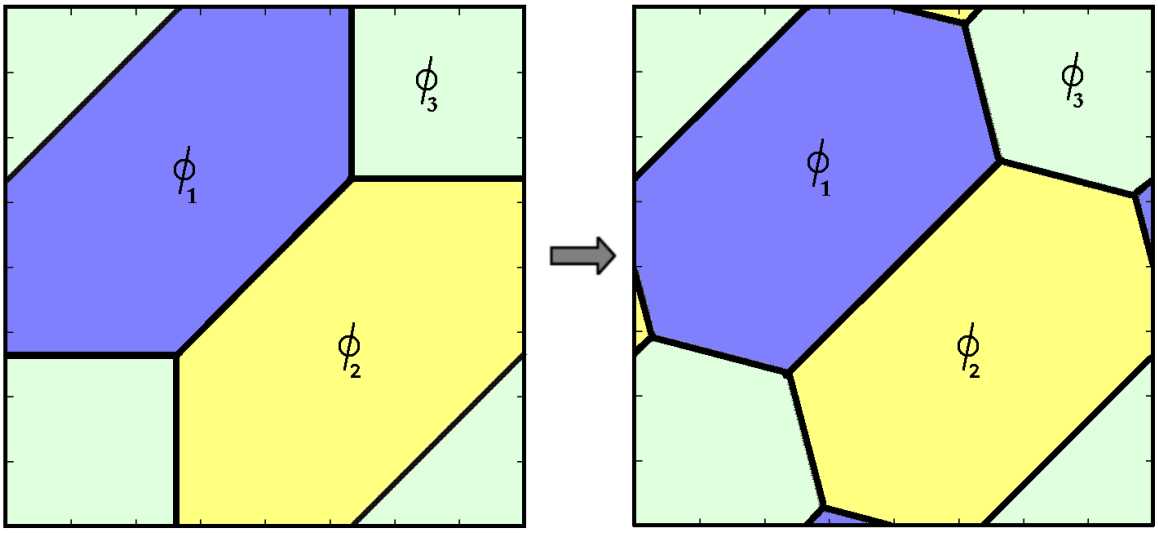

Figure 3.9: The start and ending Hexagonal Tiling configurations. This tiling can be found using either method of preserving the volume, for starting conditions similar to those seen above. The perimeter of the hexagonal tiling is always greater than the two-dimensional minimisers in figure 3.7.

domain wall should be thought of as the edge of the minimal surface. This is the point picked out to plot the configurations in figure 3.7. The structure of the walls can be seen in the energy density plots for each minimiser, figure 3.8c). The energy dips near to the triple points and increases towards the middle to the bubble separating wall in the chain and, most noticeably, the bubble configurations. Figure 3.8d) shows the full behaviour of the second volume function. It is clear to see, in each case, where the second bubble is located and how the domain walls behave.

All the minimisers can be plotted using domain walls and the perimeter, P, for given volume pairs, (V_1, V_2), of each possible minimiser can be compared. This comparison will allow for the production of a phase plot, like figure 3.4.

For certain classes of torus, hexagonal tiling (see figure 3.9) can have the same perimeter as the double band, and so both are minimisers for a given range of the parameters [33]. In the case of a square torus, the hexagonal tiling can be found as a stable solution using domain walls, but it never has a smaller perimeter than any of the minimisers in figure 3.7. This could be shown by comparing its perimeter with the other minimisers over the range of possible volume pairs, but it has been taken to never be the minimiser here.

Phase diagram

The phase diagram [33], figure 3.4a), can be parametrised using the volume pairs, (V_1, V_2). The volumes are interchangeable meaning there are three lines of symmetry. Each passes through a vertex and the triangle centre. This means the entire diagram can be derived from a sixth of it, using symmetry (see figure 3.4).

To produce a plot like the one in [33], the perimeter and volume pair must be known for each minimiser, over a range of the volumes. When both volumes are small the standard double bubble is the best configuration (as they are too small to benefit from the periodic nature of the space). The double band is the best solution when the volumes are large. If the torus is normalised so that each side has a length of one the maximum value of the perimeter is three. This will occur when all the volumes are of similar size. If one volume is small the two candidates are the standard double bubble and the band lens. The band lens comes into play only when the other volume becomes large enough. The final case of similar volume sizes, where the background volume is large, corresponds to the chain configuration.

An effective method of finding the perimeter for a range of volumes is to fix one volume and slowly change the other, allowing time between each change for the system to relax into a static configuration. Reproducing this for a range of fixed volumes will create a lattice of perimeter lengths for each configuration. A lattice point's location specifies the volumes - resulting in an array of perimeter values for each minimiser, where different points in the array relate to different pairs of volumes. The minimiser can then be found for each pair of volumes, as well as where the minimiser type changes. The perimeter of the double band is constant, so it only needs to be calculated once. The perimeter of the band lens only varies when volume of the lens alters. Only one volume needs to be varied in order to find it is perimeter values at all points on the phase plot.

To change a volume using the penalty function technique, simply alter the value of V_i^* and minimise the energy. It is best not to change the required volume by too much at a time, as a large change will cause a steep increase in the energy and the system may become unstable. The coefficient λ of the penalty function can be larger, for a given time step, if the bubble volumes remain close to their desired values during minimisation.

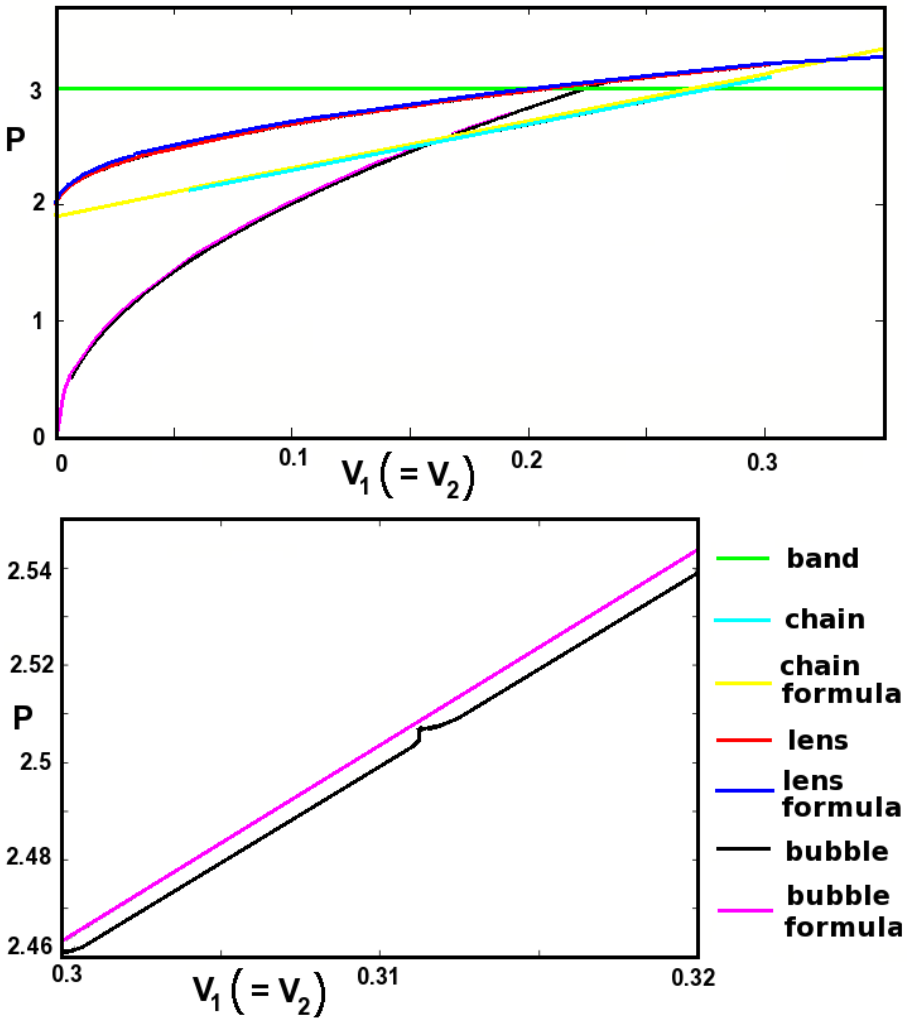

Figure 3.10: **top)** A plot of perimeter against volume when the volumes are equal. The analytical values are also plotted. **bottom)** The plot of the double bubble perimeter when is allowed to reduce under normal gradient flow, then the preservation is switched back on. The bump in the middle occurs when the bubble recovers the minimal perimeter when the system is minimised using volume preservation. The volume preserving minimisation takes the perimeter value close to the analytical value, but the trajectory will move away again once the preservation is switched off again.

The increased λ will force the calculated volumes towards the desired values and so the minimisation will conform more closely to the volume preserving flow method.

To change the volume using the preserving flow, the only way is down. If the energy is allowed to flow in the direction of steepest decline (i.e. normal gradient flow) the length of the domain walls will shrink (unless the domain wall is periodic with no junctions). This will cause the two smallest volumes to shrink as the surrounding domain walls shrink. There is a clear zero mode associated with the gradient flow of a band system, since reducing the volumes will not reduce the energy unless the domain walls are close enough to annihilate. The system can then be minimised using the preserving flow once the volume has reduced by the desired amount. This will lead to a static configuration with a different pair of volumes. The volume could be increased by either forcing the system to flow in a direction increasing the volume, or to simply add some volume onto the side of that which is already present.

To check that the perimeters and volumes match up to what is expected using these techniques, a sample should be compared to the formulae for the perimeters. These formulae can be found in [33]. Figure 3.10 shows a plot of the perimeter against volume when the volumes are equal. It can easily be seen that the three curves match closely with the curves expected. It may be expected that by allowing the system to reduce the volumes naturally (by turning off the volume preservation) that the perimeter would follow the same, or at least similar, path to the curve given by the correct formula found in [33]. In fact this is not true as can be seen in figure 3.10 bottom). Each junction will obey a Bogomolny or anti-Bogomolny equation, depending on the orientation of the vacua. Junctions will always appear in pairs with one satisfying the Bogomolny equation and the other the anti-Bogomolny equation. A domain wall originating in a Bogomolny junction will end at an anti-Bogomolny junction. This leads to an attraction between the triple points as they attempt to annihilate and could cause the bubble separating wall to contract more quickly, which more effectively reduces the energy, than if the system were in a minimal configuration for the given volumes at all times.

Given a lattice of perimeter values for each configuration the spaces can be filled in by interpolating the perimeters where they have not been calculated. The ranges in which each configuration has the minimal perimeter must also be evaluated. By checking where the minimiser changes between lattice sites and then calculating the position of the transition, where the two perimeter curves cross, the volumes at which the minimiser changes can be found.

The three volumes, and the fact they are not all independent, can be used to create coordinate system bounded by a triangle. Each position (x, y) will classify the normalised volume set (V_1, V_2, V_3). Only a sixth of the plot needs to be found as the rest is related by symmetry, see figure 3.4c). If the centre of the triangle, where all the volumes are equal, is taken to be the origin, $(0, 0)$, then

$$(x, y) = (AV_1 + BV_2 + CV_3, aV_1 + bV_2 + cV_3) \tag{3.3.2}$$

If each side has a length of one, and the triangle is equilateral, then the points where $V_3 = 1$, $V_1 = V_2 = V_3$ and $V_2 = 0$, $V_1 = V_3$, i.e. the three vertices of region one (see figure

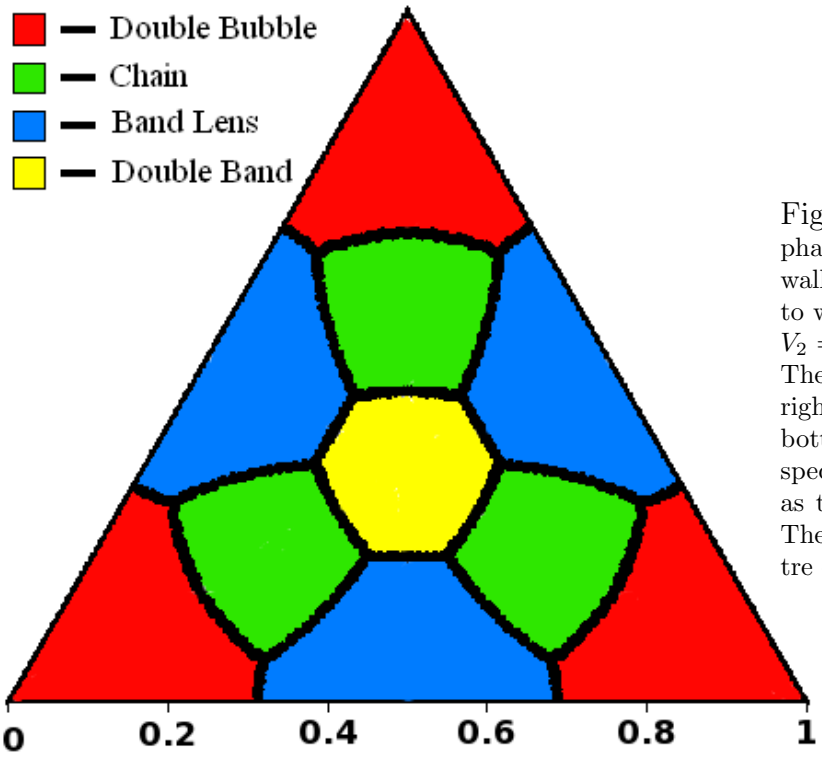

Figure 3.11: The reproduced phase plot, found using domain walls. The top vertex corresponds to when $V_3 = 1$, the left vertex when $V_2 = 1$ and the right when $V_1 = 1$. The left edge is where $V_1 = 0$, the right edge is where $V_2 = 0$ and the bottom edge is where $V_3 = 0$. The respective volumes increase from zero, as they move away from the edges. The volumes are all equal at the centre of the triangle.

3.4c)) can be used to determine the relation above. This results in

$$(x, y) = \left(\frac{1}{2} (V_1 - V_2) , \frac{1}{2\sqrt{3}} (2V_3 - V_1 - V_2) \right) \tag{3.3.3}$$

The full plot can be found in figure 3.11. Only region 1 (see figure 3.4c)) was calculated, the symmetries were used to complete the plot. It can be seen that it matches up closely to the plot found in [33], see figure 3.4.

Limitations

The first limitation of using domain walls to find surface minimisers is scale dependence. As the domain walls have a thickness, this thickness must be small compared to the size of the bubble. This creates a problem when trying to reduce one of the volumes to zero, e.g. to find where the transition exists between the standard double bubble and the band lens. The results gained above missed out a couple of lattice points just before the second volume disappeared. As the transition occurs along a roughly straight line near to the $V_2 = 0$ edge, the plot can just be continued through to the final distance, meeting with the expected value when the one circular bubble remaining has the same length as a band, i.e. $P = 2$, where $V_1 \approx 0.32$. The edges of the triangle give either a configuration with a single circular bubble or one band of vacua. The perimeter is constant in the

band lens section of each edge and will reduce to zero approaching the vertices in the bubble section. It is possible to get to smaller and smaller relative volumes by scaling the problem up. If the number of lattice points is doubled in both directions and the length of the torus is also doubled in both directions the kink is still covered by the same number of points. The wall is now half as thick compared to the total size of the torus. In effect, the torus is now four times its previous size (in terms of grid points) but the two volumes can now be half the size without increasing any errors incurred. This scaling up will work to an extent, but at some point the computation will become costly through either time or memory constraints.

An issue arises with the penalty method. Each time the magnitude of the kink energy is significantly greater than the energy penalty gained for not having the correct volume, the walls will begin to shrink until the penalty energy becomes too great and the volume has to be restored. Therefore the volumes are never actually the same but that they vary by a given amount depending on the magnitude of λ. Increasing λ will decrease this error but the penalty energy may then dominate the minimisation with the kinks not forming properly. The system is more concerned with reaching the correct volume than ensuring the field moves between the different vacua in the least-energy way (i.e. via a domain wall). The system would then try to put all of the volume into the vacuum. The derivatives in the kink energy will blow up, leading to instability. To ensure stability the volume should always be close to what is required. The value of λ should be chosen carefully so that the required accuracy in the volumes are achieved.

The volume preserving flow acts in a direction that is determined by the volume function. If the direction of steepest energy reduction and directions of reducing volumes are mostly the same (which seems logical, since when the volume decreases, so does the energy) then the majority of the flow will be prohibited by the preservation. This would make the the gradient very small, meaning that any evolution could take a long time making it much more difficult to calculate the static solutions.

Volume preserving flow can restrict the perimeter (or energy) function so that it is invariant under volume preserving variations. This can lead to equilibrium states with non-trivial zero modes that are not local minima. One such example was introduced as motivation for use of the penalty function method. Similarly, in $\mathbb{R}^2$, two circular bubbles

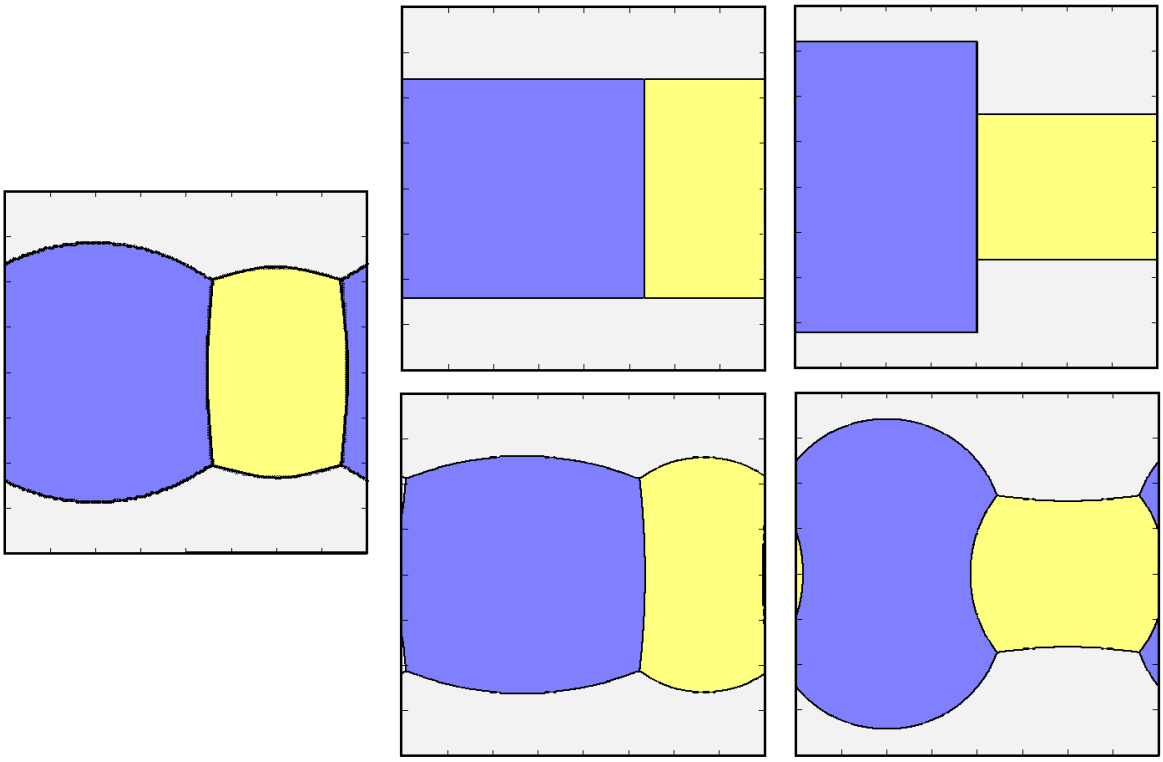

Figure 3.12: The plot on the left is obtained via the penalty function method. It is the standard chain solution. The start and end configuration are given for two systems evolved using volume preserving flow. In both cases the volumes are $V_1 = 0.4$ and $V_2 = 0.2$.

with one bubble contained within the other, will have a non-trivial zero mode of the perimeter function. The mode relates to translations of the smaller circle within the larger one, which clearly will preserve the total perimeter, as well as each individual perimeter. Modelling this as a field theory configuration, with the correct initial conditions, and evolving with volume preserving flow confirms these equilibrium states as static solutions. The only way this would be overcome is if the domain walls were to be close enough to reconnect, leading to a double bubble configuration. Equilibrium states occur for the chain configurations. An entire family of chain configurations exist on the two-torus, with only one configuration that minimises the perimeter for a given (V_1, V_2) - the standard chain. The perimeter function restricted to volume preserving flow has equilibrium states relating to the family of chains on the two-torus. For a given initial configuration the volume preserving flow of the field theory will lead to static solutions which match to a chain configuration. The range of initial configurations which result in static standard chain solutions, by applying volume preserving flow to the field theory, is small compared to the range of possible initial configurations. Examples of this can be found in figure

3.12. The initial configurations are pure areas of vacua, in the static solutions domain walls have formed and the triple junctions occur such that each domain wall is separated by 120^o. One possible explanation of this is that the forces of attraction between domain wall junctions are balanced. Volume preserving local translations of the relative position of these junctions correspond to zero modes of the perimeter function. The penalty function method overcomes these equilibrium states. The reason for this could be the slightly different problem being minimised (even in the thin wall limit providing λ is finite). The volumes are allowed to vary within the penalty function method. Also, the zero modes may only relate to the perimeter function when restricted to volume preserving flow. The penalty function minimisation method produces static solutions that are global minima from a wider range of initial configurations than applying volume preserving flow.

In general, producing double bubbles using domain walls on a flat two-torus was very successful and the results match up closely with the analytical results of [33].

Further Work

All minimal perimeter investigations using domain walls has been conducted on a flat square torus. The results of [33] are known for other torus angles. The torus of most interest would be the hexagonal torus since the hexagonal tiling and the double bands have the same perimeter for some volume pairs. Other possible work could involve using a system with four or more vacua and domain walls that have different energies. Would a system like this behave in a similar way to bubbles where the different vacua represent different viscosity mediums?

3.3.3 Three Dimensional Double Bubbles

Double bubbles on the flat three-torus were introduced earlier. They obey the same rules as the two dimensional bubbles, in that all individual surfaces meet in threes, with the junctions curves rather than points. In the plane perpendicular to the junction curve each wall is separated by 120^o. The addition of another periodic direction also allows for many more possible static configurations, like those seen in figure 3.3. The main difference

between double bubbles on the two-torus and the three-torus is that all the minimisers are only conjectured. The only proof available is that the standard double bubble is the minimal surface in $\mathbb{R}^3$ [31]. Previous numerical work suggests that there are ten different minimisers on the three-torus (see figure 3.3), and goes on to provide a potential phase diagram to indicate which configuration is the minimal surface for a given set of volumes V_1, V_2. Results here will reproduce these ten potential minimisers, each for a volume set in which a static solution exists. Other static solutions will also be investigated, and stability discussed. No investigation will be made into which configuration is the minimal surface of a given volume set V_1, V_2, only that such solutions are found using the field theory approach. Volume preserving flow will be used to find static solutions, except for configurations in which limited initial conditions lead to actual minima of the theory, under these conditions penalty function minimisation will be employed.

3.3.4 Numerical Details

The numerical tools needed are the same as those used in the two dimensional case. Calculations will utilise a cubic lattice, usually with 101^3 or 151^3 lattice sites. Fewer sites per dimension are used to limit computation time. Finding perimeter values for a given volume set may require a larger array of sites to increase accuracy of the results. As only qualitative features are of interest here, this lattice should be sufficient. The lattice spacing is $\Delta x = 0.4$, meaning that the lattice size is at least 40. 5-10 lattice points will cover each kink. The flow will be evolved using an explicit method with first order accuracy, with a time step of $\Delta t = 0.1\Delta x^2$. The derivatives are calculated using a finite difference method with second order accuracy. Stability issues may arise if the penalty function term in the gradient flow becomes large. Volumes will be normalised so $V_T = 1$.

3.3.5 Minimal Surfaces

Many more minimisers are thought to exist on a three-torus than on the two-torus. The conjectured minimisers can be found in figure 3.3, taken from [34]. There are several other candidate configurations that might be minimisers, some of which will be discussed later. For all of the surfaces created in three dimensions given here, none are shown

to be minimisers, though they may be for the volume set used. This is beyond the scope of the work undertaken here, the plots produced are purely to show that domain walls can reproduce the surfaces, and that it is likely that they could be used, like in two-dimensions, to plot a phase diagram to specify which surface is a minimiser for all possible volumes, such as the plot found in [34]. The work in [34] conjectures that ten surface minimisers exist and represent all possible minimisers in the three-torus. This conjecture is backed up by computational evidence. The surfaces used in [34] were created using a package called *Surface Evolver* [38]. It triangulates the surfaces and randomly moves these triangles. If the surface area is reduced the configuration is kept, allowing for another random manipulation, otherwise the change is discarded and process repeated. Triangulated surfaces can be seen in figure 3.3.

The Known Minimisers

Figure 3.3 shows examples of the ten surfaces that are thought to be minimisers for a range of volumes [34]. Figure 3.13 shows the ten conjectured minimal surfaces found by minimising domain wall networks on the three-torus. These surfaces are:

- **Standard Double Bubble** - Two bubbles sharing a surface.
- **Delaunay Chain** - Standard double bubble, large enough to wrap around a period and share two surfaces rather than one.
- **Cylinder Lens** - Standard double bubble with one much larger bubble, linking with itself over the period to form a cylinder.
- **Cylinder Cross** - Cylinder lens with a large bubble that wraps around the period to meet with the other side of the cylinder, to share two surfaces.
- **Double Cylinder** - Standard double bubble with both bubbles wrapping around a period to link themselves, forming two cylinders sharing a wall.
- **Slab Lens** - Standard double bubble, cylinder lens or Delaunay chain where the larger bubble is so big it wraps around two periods, forming a slab.

- **Centre Bubble** - Slab lens where the smaller bubble can wrap around a period to meet the other side of the slab, or the slab is thin enough that the bubble can link through the slab to the other surface.

- **Slab Cylinder** - Double cylinder with largest bubble wrapping two periods of slab lens with the smaller bubble wrapping a period to meet itself.

- **Cylinder String** - Delaunay chain with both bubbles wrapping around a different period to the one in which they are chained to meet themselves.

- **Double Slab** - Both bubbles are large enough to warp around two periods.

Each of the plots shown in figure 3.13 are stable configurations. Volume preserving flow was used for most minimisations, except where equilibrium surfaces of the area function restricted to volume preserving flow persist. Penalty function minimisation was used in these cases, which include the Delaunay chain, cylinder cross and cylinder string configurations. The critical factor for the initial conditions is to connect the vacua (i.e. bubbles) in the correct way. The size and shape of the space in between is much less important, the correct curves will form in any case (some exceptions will be discussed later). Close examination of the plots in figure 3.13 shows that each bubble edge has two boundary plots. These plots are actually isosurfaces of the energy. Even though the peak energy picks out the centre of the walls there are far more points with a slightly lower energy density and so the coverage of the surface is much better, creating a better picture. It would be feasible to plot the position of the mid-points of each wall, to plot a three-dimensional surface much like the plots in two-dimensions, if inclined to do so.

Other Surfaces

Figure 3.14 shows some examples of surfaces which are not minimisers for any volumes [34]. Their stability and details are discussed below;

- **Transverse Cylinder** - Allow the smaller bubble of the cylinder lens to wrap around a different period to the cylinder. It is a saddle point when the volumes are equal, in which case it is held by symmetry. If the volumes are not equal, the configuration will evolve into a cylinder cross, see appendix.

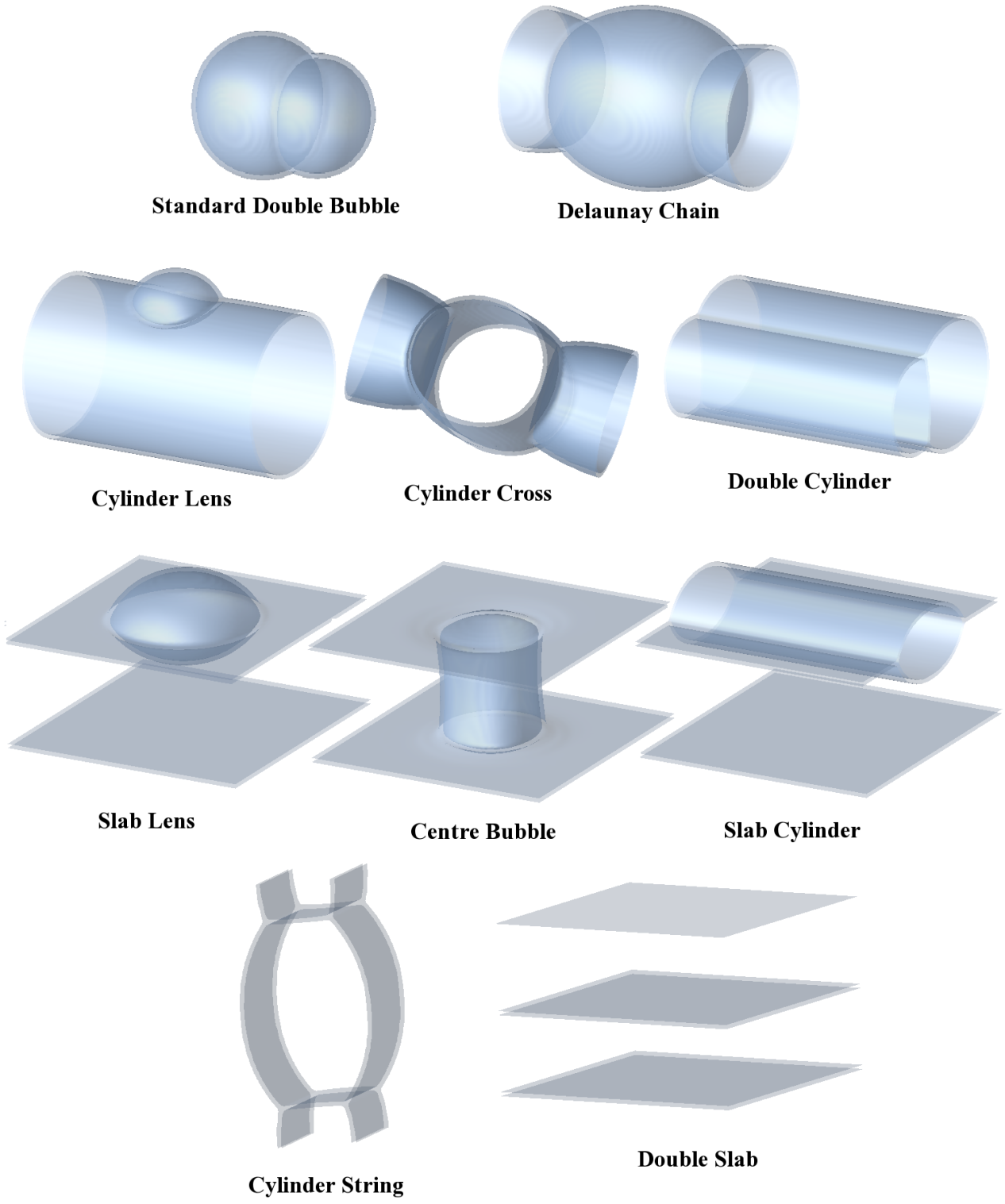

Figure 3.13: The known surface minimisers on a flat, cubic three-torus found using the field theory approach. Plots show isosurfaces near to the midpoints of domain walls.

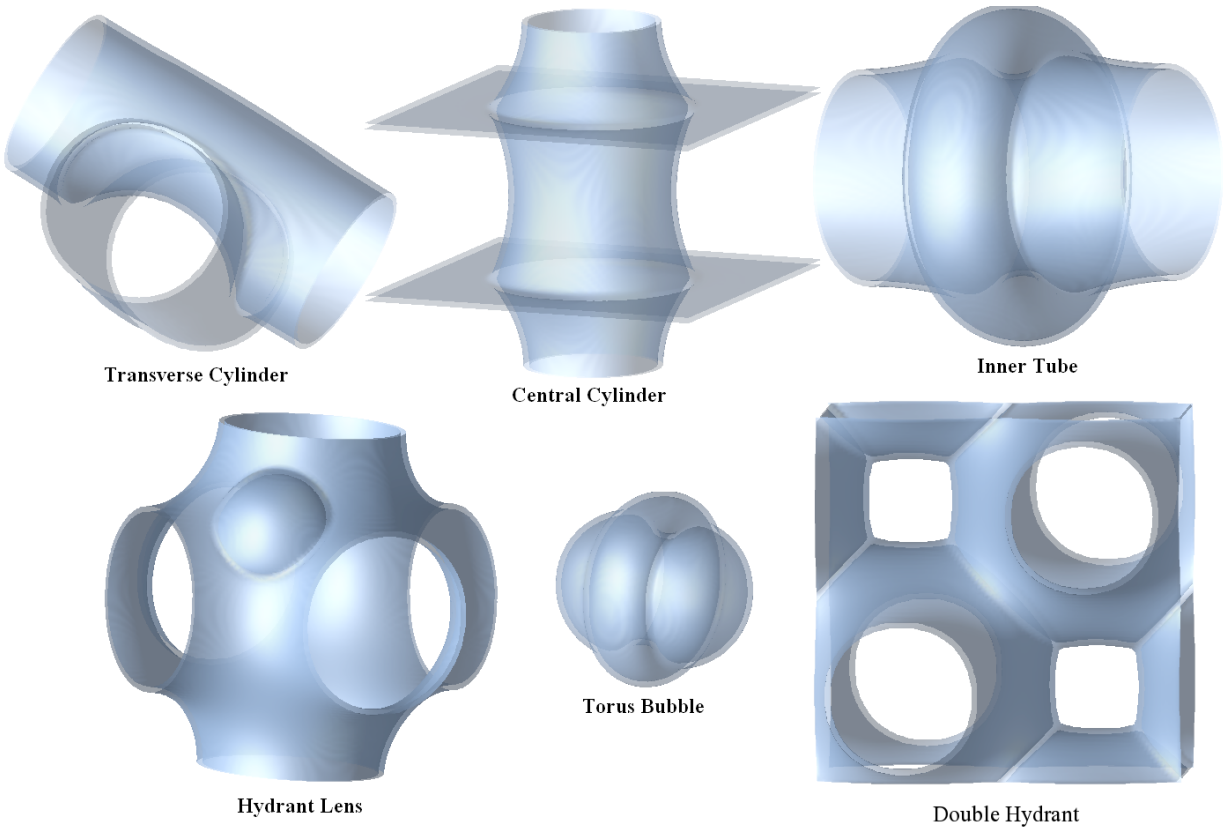

Figure 3.14: Other possible double bubble configurations on a flat, cubic three-torus. All conjectured to never be minimal surfaces, or not be stable solutions [34], where the torus bubble and the inner tube could not be found.

- **Central Cylinder** - Allow the smaller bubble in the centre bubble configuration to wrap around the third period to link with itself. It is a stable configuration, even if the symmetry of the system is broken. It is found to never be a minimal surface [34].

- **Torus Bubble** - Wrap one bubble around the other like a belt. It is a potential surface minimiser in Euclidean space. Torus bubble configurations are unstable to symmetry breaking perturbations, evolving into a standard double bubble, see appendix.

- **Inner Tube** - An expansion of the torus bubble, where the inner bubble is large enough to wrap around one direction. Under penalty function minimisation it evolves into a Delaunay chain, see appendix. The inner tube configuration is an equilibrium surface of the area function restricted to volume preserving flow.

- **Hydrant Lens** - Schwartz P surface, with a small bubble linked to it. Take a

cylinder lens and allow the cylinder to wrap around the other two periods, which can be stable for small bubbles. Above a certain bubble volume ratio it will evolve into a different configuration. An example of it deforming into a centre bubble configuration can be found in appendix.

- **Double Hydrant** - Increase the size of the standard double bubble or Delaunay chain until the bubbles meet each other across two periods and themselves across the other. It is known as 'Scary Gary'. For almost all volumes this configuration is unstable to symmetry breaking perturbations. An example of it evolving to a double cylinder can be found in appendix.

There will be many other types of surfaces that could be plotted using domain walls, but the above mentioned surfaces were the candidates that were thought to possibly be minimisers. They can be found by increasing the volume of the bubbles in some configurations so that they utilise the periodic nature of the torus. It is still possible that more minimisers exist for the three-torus and the technique of creating minimal surfaces using domain walls is one possible way that they could be found.

Limitations

There are several limitations with both techniques in three dimensions. Many issues continue from the two torus. Increased computational demands lead to issues with wall thickness, which may be mitigated by increasing lattice coverage. This cost would be computationally heavy. The size of the lattice becomes very important and a phase plot to a reasonable accuracy may require significant computing power. Volume oscillation instability from penalty function minimisation persists in three-dimensions, so care must to be taken in the choice of λ. The direction of flow, in the volume preserving method, may also result in a shallow gradient increasing computation.

Stationary points of the area function restricted to volume preserving flow occur for several of the surfaces. These configurations will be invariant under volume preserving variations. The cylinder string and Delaunay chain solutions are prime candidates as they are extended versions of the two-dimensional chain solutions. The Delaunay chain can be created by taking the two-dimensional chain and rotating it about the axis of

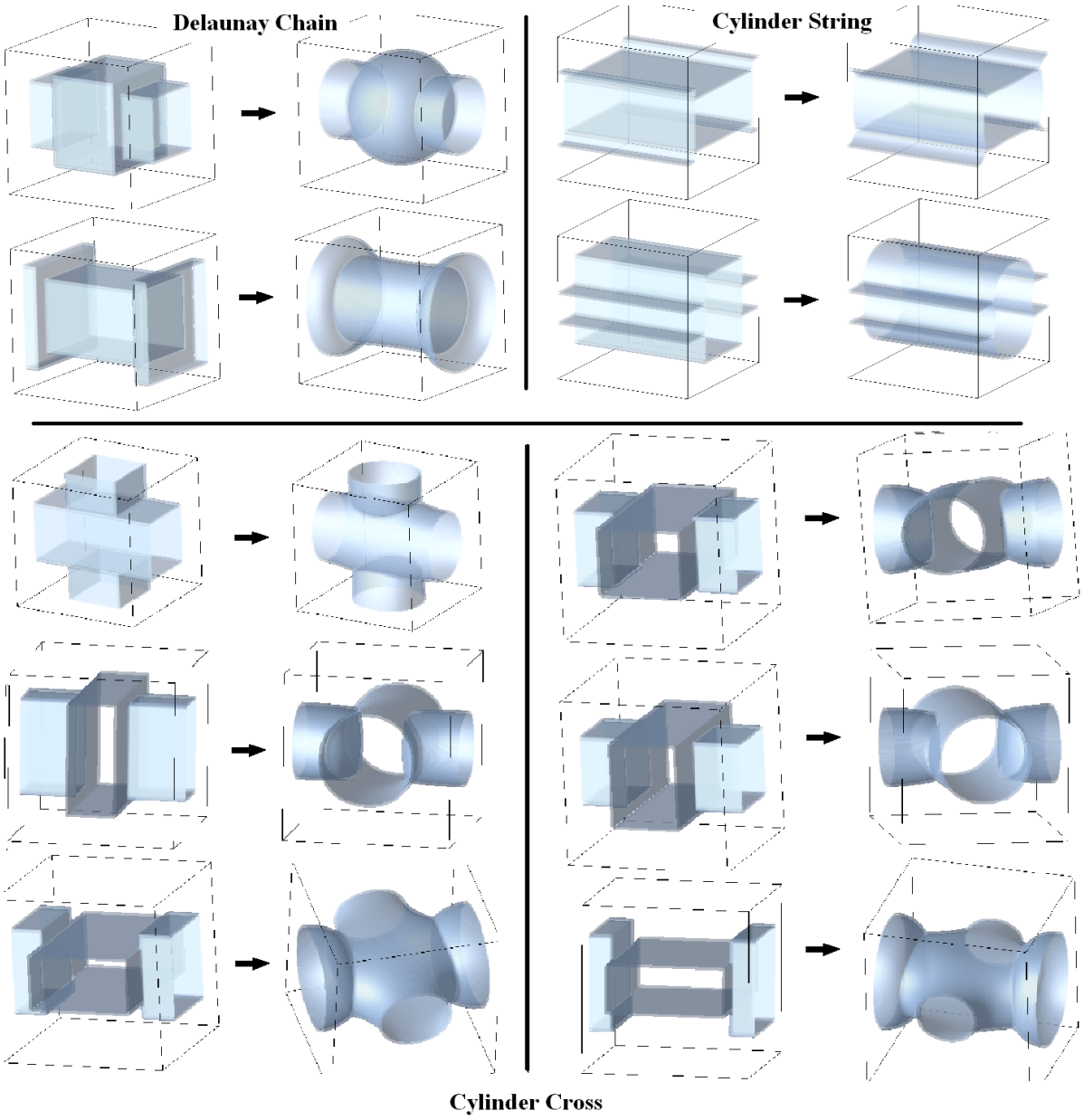

Figure 3.15: The configurations that find equilibrium states of the area function when restricted to volume preserving flow. The starting and ending configurations are plotted, for a range of starting configurations with the same volumes. The end configurations are static solutions in all cases.

symmetry passing through both of the volume separating walls. The cylinder string is simply the two-dimensional chain embedded in an extra dimension. The cylinder cross also exhibits the same problems as the chain and string. Examples of this can be seen in figure 3.15.

3.3.6 Further Work

The work detailed above is only a verification that the technique of using double bubbles to construct minimal surfaces on a three-torus is a good one. The results, especially when errors need to be very small, e.g. $\sim 1\%$ or less, can take a lot of computing power to find. Algorithm optimisation and multi-threading may address this issue

The most obvious next step using domain walls on the three-torus is to plot the phase space of all minimisers, like that found in [34]. This would serve as further evidence of the conjecture, put forward in [34] about the minimisers, since the plot in two-dimensions closely matched the expected plot. There is also scope to plot other possible double bubble surfaces using domain walls, with the possible aim of finding if another minimiser exists outside of the group of minimisers that are already known. A real scalar field could be used to plot surface minimisers for single bubbles. There is no reason why the techniques used on the square torus could not be applied to other torus configurations in three dimensions. In fact, it may be a useful technique for studying minimal surfaces in many different contexts.

3.4 Conclusion

The concept of double bubbles was introduced. A field theory approach to finding double bubbles has been introduced, expanding on details given in chapter 1 and utilising the volume preserving flow method introduced in chapter 2. The field theory in question arises in the bosonic sector of the Wess-Zumino model, with a triply degenerate potential. A second minimisation technique, penalty function minimisation, was also introduced. Minimisation of field theory configurations leads to a reproduction of a phase plot of all minimal perimeter configurations on the two-torus, which matches well with known results. The minimisation techniques can also be applied to field theory configurations on the three-torus. They have been used to compute a range of double bubble configurations and test stability.

Chapter 4

Hopf Solitons - An Introduction

4.1 Hopf Configurations

In 1931 Heinz Hopf wrote down that a three-sphere can be described in terms of circles and a two-sphere [39]. Each point on the two-sphere is defined by a many-to-one map from distinct circles on the three-sphere. This means that the three-sphere is composed of fibres, with each circular fibre relating to a distinct point on the two-sphere. This is the Hopf fibration, also known as the Hopf map or bundle. This map can be generalised to other higher dimensional spheres, but they will not be of interest here.

Hopf configurations given by, $\boldsymbol{\phi} : \mathcal{S}^3 \rightarrow \mathcal{S}^2$, have a related homotopy group $\pi_3(\mathcal{S}^2) = \mathbb{Z}$, where the Hopf map has degree one. This group in turn leads to a set of homotopy classes that will characterise $\boldsymbol{\phi}$. These homotopy classes are classified by an integer, $\mathcal{Q} \in \mathbb{Z}$, which will be called the Hopf index, or Hopf charge. Since $\boldsymbol{\phi} = (\phi_1, \phi_2, \phi_3)$ maps to an $\mathcal{S}^2$, it must have unit length, so $\boldsymbol{\phi} \cdot \boldsymbol{\phi} = 1$. A one-point compactification of $\mathbb{R}^3$ is topologically equivalent to $\mathcal{S}^3$, defined by a stereographic projection where all points on the $\mathcal{S}^3$ map to a point in $\mathbb{R}^3$ except the north pole, which maps to infinity and sets the compactification. The preimage $\boldsymbol{\phi}^{-1}(a)$ of a point a on the $\mathcal{S}^2$ then maps to a closed loop, or collection of closed loops in $\mathbb{R}^3$. The Hopf index, $\mathcal{Q}$, is then the number of times that the preimage loops of two distinct points on the $\mathcal{S}^2$, $\boldsymbol{\phi}^{-1}(a)$ and $\boldsymbol{\phi}^{-1}(b)$ are linked, see figure 4.1. This imparts the topology, there are no continuous maps between configurations of different topological charge, $\mathcal{Q}$. The topological charge $\mathcal{Q}$ can be derived mathematically in a number of ways, e.g. as an integral of the charge density over $\mathcal{S}^3$.

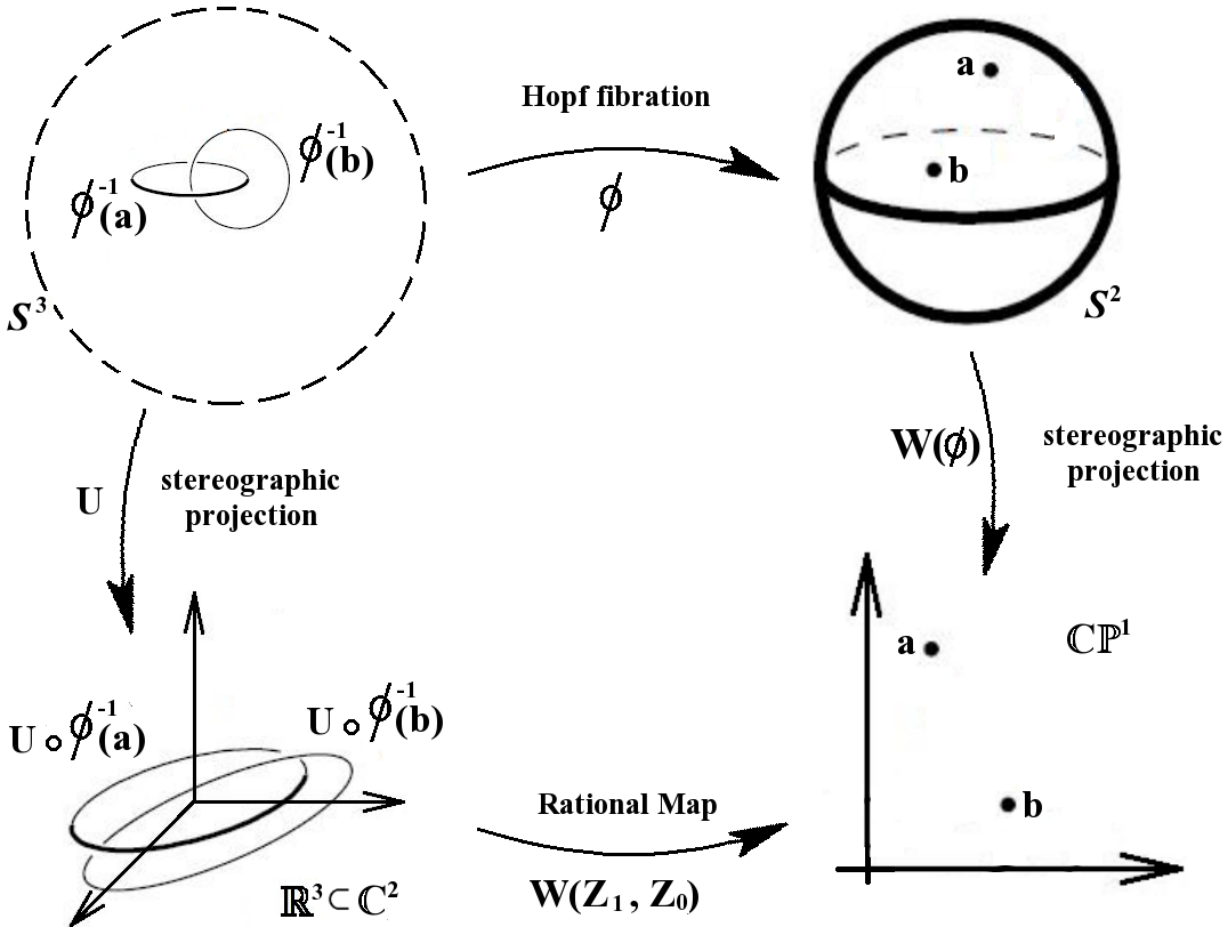

Figure 4.1: The Hopf map, ϕ, showing relations between $\mathbb{R}^3$ (bottom left), $\mathcal{S}^3$ (top left), $\mathbb{CP}^1$ (bottom right) and $\mathcal{S}^2$ (top right). The preimages of two points on the $\mathcal{S}^2$, a and b are closed loops. In this case each loop is linked once, so the Hopf index is $\mathcal{Q} = 1$. Taking a condition on the coordinates $(Z_1, Z_0) \in \mathbb{C}^2$ such that $|Z_1|^2 + |Z_0|^2 = 1$ restricts them to the $\mathcal{S}^3$, making the map $W(Z_1, Z_0) : \mathcal{S}^3 \to \mathbb{CP}^1$.

If w is the area form on the $\mathcal{S}^2$, then its pullback onto the $\mathcal{S}^3$ is an exact two-form $\mathcal{F} = \phi^* w \equiv d\mathcal{A}$, since the second cohomology group of $\mathcal{S}^3$ is trivial. The Hopf charge is then given by

$$Q = \frac{1}{4\pi^2} \int_{\mathcal{S}^3} \mathcal{F} \wedge \mathcal{A}, \tag{4.1.1}$$

which is a Chern-Simons invariant. Note this is neither uniquely defined, due to the choice of $\mathcal{A}$ which can be thought of as a gauge potential, nor can the charge density be written as a local function of ϕ.

The target $\mathcal{S}^2$ can be stereographically projected onto the complex plane with the addition of a point at infinity, i.e. onto the complex projective line, $\mathbb{CP}^1$. The complex coordinate, W - the Riemann sphere coordinate, can be related to ϕ;

$$W = \frac{\phi_1 + i\phi_2}{1 + \phi_3}. \tag{4.1.2}$$

Each component of the Hopf map can then be found by inverting the map, such that

$$\phi_1 = \frac{2\Re(W)}{1+W\overline{W}}\,, \quad \phi_2 = \frac{2\Im(W)}{1+W\overline{W}}\,, \quad \phi_3 = \frac{1-W\overline{W}}{1+W\overline{W}}. \tag{4.1.3}$$

The Hopf map is then given by

$$W = \frac{2\,(x_1+ix_2)}{1-r^2+2ix_3}, \tag{4.1.4}$$

where $r^2 = x_i x_i$. The preimages of points $W = const$ are circles that lie on tori, with all circles linked to each other once. It has a Hopf index $\mathcal{Q}=1$. This toroidal nature of the Hopf map will become important later when examining Hopf solitons in conformal field theories.

4.2 Rational Maps

A useful method for generating axial, knotted and linked Hopf configurations uses rational maps [40]. We are interested in maps from $\mathcal{S}^3 \to \mathcal{S}^2$, figure 4.1 shows that this is equivalent to looking at maps from $\mathbb{R}^3 \subset \mathbb{C}^2 \to \mathbb{CP}^1$. Take two complex functions, Z_1 and Z_0, such that $(Z_1, Z_0) \in \mathbb{C}^2$. These will form coordinates on the $\mathcal{S}^3$ (or $\mathbb{R}^3 \cup \{\infty\}$) provided that $|Z_1|^2+|Z_0|^2=1$. A spherically equivariant map of degree one can be applied to the usual coordinates on $\mathbb{R}^3$ to specify the structure of the complex coordinates on the $\mathcal{S}^3$. If $(x_1, x_2, x_3) \in \mathbb{R}^3$, then

$$(Z_1, Z_0) = \left(\frac{(x_1+ix_2)\sin\chi}{r}, \cos\chi + i\frac{x_3\sin\chi}{r}\right), \tag{4.2.1}$$

where $r^2 = x_i x_i$ and $\chi(r)$ is a monotonically decreasing profile function. It will need boundary conditions, that $\chi \to \pi$ as $r \to 0$ and $\chi \to 0$ as $r \to \infty$.

The map $W : \mathcal{S}^3 \to \mathbb{CP}^1$ can then be defined in terms of these complex coordinates, such that

$$W\,(Z_1, Z_0) = \frac{p\,(Z_1, Z_0)}{q\,(Z_1, Z_0)}. \tag{4.2.2}$$

This is a rational map of polynomials, p and q in Z_1, Z_0. Inverting this map using (4.1.3) will give $\boldsymbol{\phi}$. This creates a relation between the $\mathbb{R}^3$ coordinates x_i and $\boldsymbol{\phi}$. The Hopf map

(4.1.4) is then given by

$$W = \frac{Z_1}{Z_0}\,, \quad \text{with} \quad \sin\chi = \frac{2r}{1+r^2}\,,\ \cos\chi = \frac{1-r^2}{1+r^2} \quad \text{or} \quad \chi(r) = \tan^{-1}\frac{2r}{1-r^2}. \quad (4.2.3)$$

Any rational map will then have a position curve given by $q\left(Z_1, Z_0\right) = 0$ from (4.1.2). The Hopf map then clearly has a position curve made up of a circle in the $x_3 = 0$-plane, centred at the origin with unit radius (in these units).

The map W can be extended by relaxing the constraint on Z_1 and Z_0 to an inequality. W then maps the four-ball, with boundary $\mathcal{S}^3$ (which is contained in $\mathbb{C}^2$) to $\mathbb{C}^2$, giving it a full complex structure. The degree of the map $\left(p\left(Z_1, Z_0\right), q\left(Z_1, Z_0\right)\right)$ can be found by counting preimages of a point, since (p, q) is holomorphic and all Jacobian factors will be positive for all points on the target space using the CauchyRiemann equation. The degree of the map (p, q) will be equal to the topological charge $\mathcal{Q}$. This allows the Hopf index of a given rational map to be calculated. Take any point, e.g. $(\varepsilon, 0)$, then the Hopf index will be the number of solutions to $(p, q) = (\varepsilon, 0)$. The choice of point should be made to allow the number of solutions to be evaluated easily, e.g. by allowing for one of Z_1, Z_0 to be eliminated.

The following are details of axial, knotted and linked rational maps, generalising the work found in [40]. Any maps produced in [40] will be noted as such.

Axial Configurations

An axial configuration is one which has a symmetry about an axis. A common interpretation of Hopf solitons with axial symmetry arises from taking a two-dimensional soliton, called a baby Skyrmion [41] and embedding this into three-dimensions by rotating about a fixed axis at some point away from the baby Skyrmion, creating a toroidal structure. The baby Skyrme field is a map: $\mathcal{S}^2 \to \mathcal{S}^2$ which is classified by an integer, $m \in \mathbb{Z} = \pi_2\left(\mathcal{S}^2\right)$. This winding number is the topological charge of the baby Skyrmion. It also has an internal phase, which can also be wound as the two-dimensional field is rotated, as long as the start and ending fields match. This means an extra winding of $2\pi n$ can be added to the new three-dimensional axial configuration. So m counts the winding of a toroidal cross section of the field while n counts the number of twists that the field makes as it wraps around the torus. This type of configuration will be referred to as

type $\mathcal{A}_{n,m}$ and the Hopf index associated with it will be $\mathcal{Q}=nm$. With the conventions used here, the position of the a soliton (or general field configuration) will be taken to be where $\phi_3=-1$, when the field is at its furthest point from the vacuum where $\phi_3=1$. This will be a collection of one or more closed loops. Any other pre-image curve of $\boldsymbol{\phi}$ will then link with the pre-image of $\phi_3=-1$ exactly $\mathcal{Q}$ times. In general, configurations tend to have a higher energy per unit charge as $|n-m|$ increases. For example an $\mathcal{A}_{5,1}$ configuration will have a string wound five times as one revolution of the ring is made. This type of situation could lead to a twisting of the ring associated with the increased winding. A good example is the $\tilde{\mathcal{A}}_{3,1}$ configuration found to be the $\mathcal{Q}=3$ ground state in the Skyrme-Faddeev model, where the ring structure of the static configuration is highly perturbed [42, 43]. This model will be discussed later.

In terms of a rational map, where the Riemann sphere coordinate W is given as a ratio of polynomials in the two complex variables Z_1 and Z_0, an $\mathcal{A}_{n,m}$ axial configuration of Hopf index $\mathcal{Q}=nm$ could take the form [40]

$$W=\frac{Z_1^n}{Z_0^m}. \tag{4.2.4}$$

Clearly, any point in the target space will have nm solutions to $(Z_1^n, Z_0^m)=(a,b)$. In fact, topologically equivalent field configurations can be created using a rational map:

$$W=\pm\frac{aZ_1^p+bZ_0^qZ_1^r+cZ_0^s}{dZ_0^t+eZ_1^uZ_0^v+fZ_1^w}, \tag{4.2.5}$$

where $a,b,c,d,e,f\in\mathbb{R}$ and $p,q,r,s,t,u,v,w\in\mathbb{N}$, with some caveats (and (4.2.5) contains no common factors). One or both of a,b must be non zero, as must one or both of d,e. The axial windings, n,m will then be $n=\sup\{p,q+r,s\}$ and $m=\sup\{t,u+v,w\}$. The standard rational map is when $a,d=1$ and $b,c,e,f=0$. Varying the constants and their signs will alter the structure of the fields in a way that could be continuously deformed to the standard rational map. Altering the structure like this will become useful later in creating linked configurations. The field configurations can be found from W by inverting the stereographic projection back to the $\mathcal{S}^2$, (4.1.2).

In terms of knot theory, these axial configurations are single closed strings of $\phi_3=-1$, or multiple closed strings sat on top of each other. The axial symmetry implies that these closed strings will be circular rings. Configurations consisting of a single closed string

which does not wind around itself are referred to as unknots. When considering general configurations, which might contain more than one string, unknots might also be referred to as unlinks.

Knot Configurations

The knot configurations seen here will all be torus knots, which are knots that lie on the surface of a torus. As the knots lie on the surface of a torus (or can be continuously deformed so that they do), they will wind around the two cycles of the torus an integer number of times each. This allows for the knots to be classified, with a knot which wraps a times around the cross section of the torus and b times around the torus ring, being labelled an (a,b) knot. In the notation used here an (a,b) torus knot will be denoted $\mathcal{K}_{a,b}$, or sometimes as $\mathcal{K}_{a,b}^{\alpha,\beta}$ where α,β will relate to the rational map in Z_1, Z_0 used to generate torus knot field configurations. To be a torus knot, a and b must be co-prime and $a>b$. $\mathcal{K}_{a,b}$ will have $a(b-1)$ crossings, which relates the details here to the standard knot catalogue [44]. Important examples here will be the trefoil, $\mathcal{K}_{3,2}$, Solomon seal knot[1], $\mathcal{K}_{5,2}$ and the 8-crossing torus knot, $\mathcal{K}_{4,3}$. For further details on knot theory see [44, 45]. The charge, $\mathcal{Q}$, will equate to the sum of the crossing number and the number of times a linking curve wraps around $\phi_3=-1$.

In terms of complex coordinates on the $\mathcal{S}^3$, Z_1 and Z_0, the Riemann sphere coordinate W (i.e. the stereographic projection of $\boldsymbol{\phi}$ (4.1.2)) will be a rational map of the form [40];

$$W = \frac{Z_1^\alpha Z_0^\beta}{Z_1^a \pm Z_0^b}\,, \quad \text{with} \quad \alpha>0\,,\ \beta\geq 0: \quad \alpha,\beta\in\mathbb{Z}. \tag{4.2.6}$$

The Hopf index is $\mathcal{Q}=\alpha b+\beta a$, i.e. the number of solutions to $(Z_1^\alpha Z_0^\beta, Z_1^a \pm Z_0^b)=(\varepsilon,0)$.

The rational map (4.2.6) allows for knot configurations to be produced at any Hopf index greater than three, which will be all that is required here. For a given $\mathcal{Q}$, some (a,b) knots will exist for different α,β which will be qualitatively the same, i.e. they can all be continuously deformed into each other. The orientation of the knot can be altered with a simple complex transformation: $Z_1 \to \overline{Z_1}$. In fact, this is true of any rational map, the change in orientation will effect the winding directions.

[1] also known as cinquefoil or pentafoil knot

Clearly setting $a, c, e = 0, |b|, |d|, |f| = 1$ in (4.2.5) will give (4.2.6). In fact any non-co-prime $(a, b = 1)$ knot rational map will produce an $\mathcal{A}_{a,1}$ type configuration. Furthermore, $(a, b = a)$ knot rational maps will produce $\mathcal{A}_{a,a}$ type configurations and non-co-prime (a, b) knot rational maps will produce link type configurations, provided that (a, b) are chosen to produce a reducible denominator in (4.2.6) and α, β are chosen to give a solution with the correct $\mathcal{Q}$. $(a, b) = (1, 1)$ knot rational maps will produce axial type configurations, but the $\phi_3 = -1$ string might not be a ring.

The field configurations produced by the torus knot rational maps will have increased symmetry when compared to the eventual static solitons found via energy minimisation. A small perturbation of the coordinates will break any symmetry, although in general this will already be achieved by the cubic lattice.

Links and Beyond

So far the configurations discussed have been made up of a single closed string of $\phi_3 = -1$, or several identical closed strings on top of each other. It is also possible to create configurations in which two closed strings are inter-linked with each other and cannot be pulled apart. These configurations are referred to as links; a series of non-intersecting linked knots or unknots. Single closed strings are referred to as unlinks. The most trivial link is the Hopf link, two circular strings linked together such that the plane of the rings are perpendicular and each string passes through the centre of the opposing circle. This link would have a linking number of one, i.e. the number of times the two circles link together. For the purposes of counting here, the linking number will be the number of times the two strings are linked together if both strings were to be pulled apart in a planar direction. The number of times the strings loop around each other will be the linking number. For the Hopf link, each string would wind around each other once if pulled apart in this way, giving a linking number of one. Multi linked configurations considered will not be of the Brunnian link type, where the removal of one of the 3 or more strings will result in a series of unlinks. The simplest example of this is the Borromean rings, in which no two rings are linked, but the combination of the three rings are. It is also possible to have knotted strings linked together. In the case of the Hopf charges under consideration here, these configurations will not arise, although they may arise for larger

$\mathcal{Q}$'s, like in the Skyrme-Faddeev model [40].

In terms of the linking number of general configurations, each individual closed string is assigned an individual linking number, i.e. the number of times it is linked to all other strings. Each pair of strings will be linked with each other an equal number of times, but the overall linking for each string might be different. For example, three strings linked in a chain configuration will have the two end strings linked once, but the middle string will be linked to both ends, and so is linked twice.

The link configurations of static Hopf solitons in the field theory will differ from the standard links in shape, but will be qualitatively the same, meaning the $\phi_3 = -1$ strings can be continuously deformed into the standard link configurations, making it possible to count the linking number. Each unlink will have a Hopf index associated with it, it will be topologically matched to an axial or knot configuration of a given Hopf index, with the $\phi_3 = -1$ string being deformed in some way. The total Hopf index of a given link configuration will be the sum of each unlinks Hopf index added to the sum of the linking numbers. For example a Hopf index, $\mathcal{Q}=6$ link might consist of two $\mathcal{A}_{2,1}$'s, each linked once; $\mathcal{Q}=2+2+1+1=6$. This link would be a $\mathcal{L}^{1,1}_{2,2}$ link, where two Hopf index 2 unlinks are each linked to each other once. Notation for links containing knots will not be introduced, as these configurations do not arise in the Hopf index range investigated here.

Rational maps of the complex coordinates Z_1 and Z_0, giving the Riemann sphere coordinate, W, (4.2.2) corresponding to a link configuration will have a reducible denominator, $q\,(Z_1, Z_0)$. The number of possible solutions of each reduced denominator will be the linking number of what would be the unlink of the appropriate part of the decomposed W into a sum of fractions.

Rational maps leading to linked configurations can arise from the knot rational map (4.2.6), where (a, b) are no longer co-prime, and a minus sign taken in the denominator. The simplest form of this is for a type $\mathcal{L}^{1,1}_{n,n}$ link with $\mathcal{Q} = 2n+2$, taking $(a, b) = (2, 2)$, $\alpha, \beta = n+1, 0$ i.e. [40]

$$W = \frac{Z_1^{n+1}}{Z_1^2 - Z_0^2} = \frac{Z_1^n}{2\,(Z_1 - Z_0)} + \frac{Z_1^n}{2\,(Z_1 + Z_0)}, \tag{4.2.7}$$

which gives two $\mathcal{A}_{n,1}$ type configurations linked together once. It can easily be seen that

$(Z_1^{n+1}, Z_1^2 - Z_0^2) = (\varepsilon, 0)$ will have $2(n+1)$ solutions. For configurations with two strings double linked, $q = (Z_1^4 - Z_0^2)$ can be taken, and three double linked strings might have a $q = (Z_1^3 - Z_0^3)$ denominator. This would give the decomposed fractional denominators two solutions each, allowing for the double linking. More exotic linking is possible, but will not be necessary here, indeed the triple linked solutions only arise at $\mathcal{Q} \geq 9$.

The following will be a Hopf index breakdown of allowed link configurations and rational maps associated with them. In most cases it is possible to get a link with the same topology using a different rational map, and some alternatives will be given but the list is not complete. A rational map W for all relevant starting linked configurations for $4 \leq \mathcal{Q} \leq 11$ will be given.

$\mathcal{Q} = 4$ Hopf index of four is the minimum required to permit linked configurations as both unlinks can have a minimum of one linking, and the unlinks can have a minimum index of one. The only possible linked configuration is $\mathcal{L}^{1,1}_{1,1}$, where two $\mathcal{A}_{1,1}$'s are linked. This is found by setting $n = 1$ in (4.2.7). An $\mathcal{L}^{1,1}_{1,1}$ configuration can also be gained from (4.2.6) by setting $(a, b) = (2, 2)$ and either $\alpha, \beta = 1, 1$ or $2, 0$. Note that $\alpha, \beta = 2, 0$ is exactly the same as setting $n = 1$ in (4.2.7).

$\mathcal{Q} = 5$ Only one possible linked configuration is possible at Hopf index five, an $\mathcal{L}^{1,1}_{1,2}$ where an $\mathcal{A}_{1,1}$ and an $\mathcal{A}_{2,1}$ are linked once. Possible rational maps for this could be

$$W = \frac{Z_1^2}{Z_1 - Z_0} + \frac{Z_1}{2\,(Z_1 + Z_0)}\,, \quad W = \frac{Z_1}{Z_1 + Z_0} + \frac{Z_1 Z_0}{Z_1 - Z_0}, \tag{4.2.8}$$

where the factor of 2 included in the second decomposed fraction makes the contribution to the overall link structure by the unlinked $\mathcal{A}_{1,1}$ type part lower than that of the $\mathcal{A}_{2,1}$ type part. Indeed, any $\mathcal{L}^{1,1}_{n,m}$ type configuration can be produced as a decomposition like the first given;

$$W = \frac{Z_1^m}{Z_1 - Z_0} + \left(\frac{n}{m}\right) \frac{Z_1^n}{Z_1 + Z_0}, \tag{4.2.9}$$

where $m > n$ and the n/m pre-factor will make the lower Hopf index unlink smaller relative to the higher Hopf index unlink. Note here smaller refers to the volume of the unlink, not necessarily the diameter of the $\phi_3 = -1$ string.

$\mathcal{Q}=6$ Hopf index 6 allows for the first doubly linked configurations to be formed. In fact there are three possible configurations; $\mathcal{L}^{2,2}_{1,1}$, $\mathcal{L}^{1,1}_{1,3}$ and $\mathcal{L}^{1,1}_{2,2}$. An $\mathcal{L}^{1,1}_{2,2}$ type configuration can be found from (4.2.7) by setting $n=2$.

Alternatively a $(2,2)$ knot rational map (4.2.6) will produce an $\mathcal{L}^{1,1}_{2,2}$ configuration for $\alpha,\beta=2,1$ and vice versa. An $\mathcal{L}^{2,2}_{m,m}$ type configuration has a rational map of the type,

$$W=\frac{Z_1^{m+2}}{Z_1^4-Z_0^2}=\frac{Z_1^m}{Z_1^2-Z_0}+\frac{Z_1^m}{Z_1^2+Z_0}. \tag{4.2.10}$$

Clearly setting $m=1$ in (4.2.10) will give an $\mathcal{L}^{2,2}_{1,1}$ type configuration. This can also be found from (4.2.6) as a $(4,2)$ type knot rational map with $\alpha,\beta=1,1$ or $\alpha,\beta=3,0$. An $\mathcal{L}^{1,1}_{1,3}$ structure could be constructed using (4.2.9), with $m=3,n=1$ or from something like

$$W=\frac{Z_1}{Z_1+Z_0}+\frac{Z_1^2Z_0}{Z_1-Z_0}. \tag{4.2.11}$$

$\mathcal{Q}=7$ Hopf Index 7 permits three possible 2-string links, $\mathcal{L}^{1,1}_{2,3}$, $\mathcal{L}^{2,2}_{1,2}$ and $\mathcal{L}^{1,1}_{1,4}$. The $\mathcal{L}^{1,1}_{1,4}$ configurations can be produced from (4.2.9) as can the $\mathcal{L}^{1,1}_{2,3}$. A rational map of polynomials in Z_1,Z_0 for $\mathcal{L}^{1,1}_{2,3}$ could take the form of;

$$W=\frac{Z_1Z_0}{Z_1+Z_0}+\frac{Z_1Z_0^2}{Z_1-Z_0}. \tag{4.2.12}$$

The double linked $1-2$ configuration $\mathcal{L}^{2,2}_{1,2}$ can be made using an $\mathcal{L}^{2,2}_{n,m}$ rational map with $n=1$ and $m=2$;

$$W=\frac{Z_1^m}{Z_1^2-Z_0}+\left(\frac{n}{m}\right)\frac{Z_1^n}{Z_1^2+Z_0}, \tag{4.2.13}$$

which is similar to (4.2.9), in this case the two solutions in the decomposed fractional denominators allow for the double linking. Setting $n=1,m=2$ would give a $\mathcal{L}^{2,2}_{1,2}$. As with the axial maps, rational map solutions with large $|n-m|$ are likely to have relatively high energy per unit charge in a given field theory and thus $\mathcal{L}^{1,1}_{n,m}$ type configurations are unlikely to become global minima, or even exist as static solutions if $|n-m|$ becomes large enough.

The first possible three string configuration appears at $\mathcal{Q}=7$, the $\mathcal{L}^{1,2,1}_{1,1,1}$. This is a chain of $\mathcal{A}_{1,1}$'s, where the end strings are both linked once to the middle string, giving the middle string a linking number of 2. Possible chain configurations will be mentioned for

each homotopy class, although no explicit maps will be given. Triple string configurations where each unknot links with all the other unknots will be given explicitly. Indeed, it has already been seen that these configurations are the minimal energy solutions in the Skyrme-Faddeev model for Hopf index $\mathcal{Q}=9\,..\,12$ [40].

$\mathcal{Q}=8$ As the Hopf index increases, so does the number of possible linked configurations. With two strings, there are possible configurations of the types $\mathcal{L}^{1,1}_{3,3}$, $\mathcal{L}^{1,1}_{2,4}$, $\mathcal{L}^{1,1}_{1,5}$, $\mathcal{L}^{2,2}_{2,2}$ and $\mathcal{L}^{3,3}_{1,1}$ - the first triple linked solution. $\mathcal{L}^{1,1}_{3,3}$ can be found from (4.2.7), $\mathcal{L}^{1,1}_{2,4}$, and $\mathcal{L}^{1,1}_{1,5}$ from (4.2.9) and $\mathcal{L}^{2,2}_{2,2}$ from (4.2.10). A triply linked configuration, $\mathcal{L}^{3,3}_{m,m}$ would have a rational map of the form

$$W=\frac{Z_1^{m+3}}{Z_1^6-Z_0^2}=\frac{Z_1^m}{Z_1^3-Z_0}+\frac{Z_1^m}{Z_1^3+Z_0}. \tag{4.2.14}$$

Taking $m=1$ will give a system $\mathcal{L}^{3,3}_{1,1}$. Note that changing the power of Z_0 in the denominator of (4.2.14) to 3 will create a system with three Hopf index m strings, each double linked to each other. The minimum $\mathcal{Q}$ for this would be 15, as three $\mathcal{Q}=1$ strings would each have a linking number of 4.

There are also two 3-string configurations, with either a $\mathcal{Q}=2$ string in the middle, or at one of the ends of the chain.

$\mathcal{Q}=9$ Hopf index $\mathcal{Q}=9$ allows for a wide range of possible linked configurations, including the first 3-string systems with all strings linking with each other. The list of links consists of the $\mathcal{L}^{1,1}_{3,4}$, $\mathcal{L}^{1,1}_{2,5}$, $\mathcal{L}^{1,1}_{1,6}$ all found from (4.2.9); the $\mathcal{L}^{2,2}_{2,3}$ and $\mathcal{L}^{2,2}_{1,4}$, both found from (4.2.13); the $\mathcal{L}^{3,3}_{1,2}$ found from the rational map

$$W=\frac{Z_1^n}{Z_1^3+Z_0}+\frac{Z_1^m}{Z_1^3-Z_0}, \tag{4.2.15}$$

with $n,m=1,2$; and the triple string systems $\mathcal{L}^{2,2,2}_{1,1,1}$, $\mathcal{L}^{1,2,1}_{2,2,1}$ and $\mathcal{L}^{1,2,1}_{2,1,2}$. A three-linked configuration of each Hopf index unlinks $\mathcal{L}^{2,2,2}_{n,n,n}$, could have a rational map of the form

$$W=\frac{Z_1^{n+2}}{Z_1^3-Z_0^3}. \tag{4.2.16}$$

In the case of $\mathcal{Q}=9$, taking $n=1$ gives three interlinked $\mathcal{A}_{1,1}$ unlinks. The other two triple component configurations are chains.

$\mathcal{Q} = 10$ The possible linked solutions for Hopf index $\mathcal{Q} = 10$ are;

$$\begin{array}{ccccccccc} \mathcal{L}^{1,1}_{4,4}, & \mathcal{L}^{1,1}_{3,5}, & \mathcal{L}^{1,1}_{2,6}, & \mathcal{L}^{1,1}_{1,7}, & \mathcal{L}^{2,2}_{3,3}, & \mathcal{L}^{2,2}_{2,4}, & \mathcal{L}^{2,2}_{1,5}, & \mathcal{L}^{3,3}_{2,2}, & \mathcal{L}^{3,3}_{1,3}, \\ \mathcal{L}^{4,4}_{1,1}, & \mathcal{L}^{2,2,2}_{1,1,2}, & \mathcal{L}^{1,2,1}_{2,2,2}, & \mathcal{L}^{1,2,1}_{1,1,4}, & \mathcal{L}^{1,2,1}_{1,4,1}, & \mathcal{L}^{1,2,1}_{1,2,3}, & \mathcal{L}^{1,2,1}_{3,1,2}, & \mathcal{L}^{1,2,1}_{1,3,2}, & \mathcal{L}^{1,2,2,1}_{1,1,1,1}, \end{array}$$

including the first example of a 4-component link, $\mathcal{L}^{1,2,2,1}_{1,1,1,1}$. The 2-component single linked configurations can be found using either (4.2.7) or (4.2.9). The 2-component double linked configurations can be constructed from (4.2.10) or (4.2.13) and the 2-component triple linked configurations from (4.2.14) or (4.2.15). The 3-component linked configuration in which each element is linked together once, e.g. $\mathcal{L}^{2,2,2}_{n,m,m}$, can be found from a rational map such as,

$$W = \frac{Z_1^n}{Z_1 - Z_0} + \frac{Z_1^{m+1} + Z_1^a Z_0^b}{Z_1^2 + Z_0^2 + Z_1 Z_0}\,; \quad \text{where} \quad m + 1 \geq a + b : \; a, b \geq 0, \tag{4.2.17}$$

where the strings are positioned around each other in a triangular configuration, or from

$$W = \frac{Z_1^n}{Z_0} + \frac{Z_1^{m+1}}{Z_1^2 - Z_0^2}, \tag{4.2.18}$$

where the strings are positioned in a line. Linking such as these can be expanded to include axial components with more winding, e.g. $\mathcal{A}_{2,2}$ types if desired.

$\mathcal{Q} = 11$ Linked configurations for Hopf index $\mathcal{Q} = 11$ include

$$\begin{array}{ccccccc} \mathcal{L}^{1,1}_{4,5}, & \mathcal{L}^{1,1}_{3,6}, & \mathcal{L}^{1,1}_{2,7}, & \mathcal{L}^{1,1}_{1,8}, & \mathcal{L}^{2,2}_{3,4}, & \mathcal{L}^{2,2}_{2,5}, & \mathcal{L}^{2,2}_{1,6}, \\ \mathcal{L}^{3,3}_{2,3}, & \mathcal{L}^{3,3}_{1,4}, & \mathcal{L}^{4,4}_{1,2}, & \mathcal{L}^{2,2,2}_{1,2,2}, & \mathcal{L}^{2,2,2}_{1,1,3}, & \mathcal{L}^{1,2,1}_{2,3,2}, & \mathcal{L}^{1,2,1}_{2,2,3}, \\ \mathcal{L}^{1,2,1}_{1,1,5}, & \mathcal{L}^{1,2,1}_{1,5,1}, & \mathcal{L}^{1,2,1}_{1,2,4}, & \mathcal{L}^{1,2,1}_{4,1,2}, & \mathcal{L}^{1,2,1}_{1,4,2}, & \mathcal{L}^{1,2,2,1}_{1,2,1,1}, & \mathcal{L}^{1,2,2,1}_{2,1,1,1}. \end{array}$$

All the 2 and 3-component links can be found using (4.2.7), (4.2.9), (4.2.10), (4.2.13), (4.2.14), (4.2.15), (4.2.17) and (4.2.18). Again, the triple string configurations in which all the strings are linked can be orientated in a line or a triangular configuration.

In the case of all link rational maps, there will exist an inherent symmetry based on the combination of the decomposed maps. This is most evident when linking two same type fractions. It is therefore useful to perturb the rational map configurations before performing energy minimisation. In fact, unperturbed configurations which either do not exist as local energy minima, or exist, but not as the global minima will often perturb themselves and tend off towards a different minima. When doing numerical

minimisation it is always useful to robustly test the energy minima, so in all cases the initial conditions will be perturbed away from any axis of symmetry by transforming the spatial coordinates. For example;

$$x \to ax,\ y \to by+ez,\ z \to cz+fy+gx, \quad \text{where } a,b,c \sim 1 \text{ and } |e|,|f|,|g| \ll 1. \tag{4.2.19}$$

This particular type of coordinate transformation would squash/stretch the solution in each of the x, y, z directions as well as changing the orientation of the y, z axes with respect to the lattice, i.e. deparallelized any symmetry axes with the box.

4.3 Skyrme-Faddeev

The best studied example of a field theory which permits Hopf solitons is the Skyrme-Faddeev model [7]. The model is of potential physical interest in both quantum field theory and condensed matter physics. It has been used as a possible description of potential knotted solitons in multicomponent superconductors [46,47] and it is a potential candidate for a low energy effective theory of QCD [48–50]. It has a Lagrangian density containing two parts, a sigma-type term and a Skyrme-type term.

$$\mathcal{L}_{FN} = (\partial^\mu \boldsymbol{\phi} \cdot \partial_\mu \boldsymbol{\phi}) - \kappa\,(\partial^\mu \boldsymbol{\phi} \times \partial^\nu \boldsymbol{\phi}) \cdot (\partial_\mu \boldsymbol{\phi} \times \partial_\nu \boldsymbol{\phi})\,. \tag{4.3.1}$$

Derrick's theorem is appeased by adding in the term that is fourth order in derivatives, like that shown in chapter 1. The details of this field theory follow on from that discussed above, where only static solutions are of interest here. Since static solutions have a finite energy, the field must tend to a constant at infinity. This choice is arbitrary, it is usually taken to be $\boldsymbol{\phi}=(0,0,\pm 1)$. Depending on your choice, the Riemann sphere coordinate W will either vanish or diverge at infinity. Taking $\phi_3 \to 1$ at infinity gives a position of the soliton where $\phi_3 \to -1$. Here, W will diverge at the position and vanish at infinity. An energy bound exists and is of the form [51, 52]

$$E \geq c\mathcal{Q}^{\frac{3}{4}}. \tag{4.3.2}$$

It has been shown that this fractional growth is optimal [53]. Optimal values for c have been conjectured, but this will not be of consequence in this discussion.

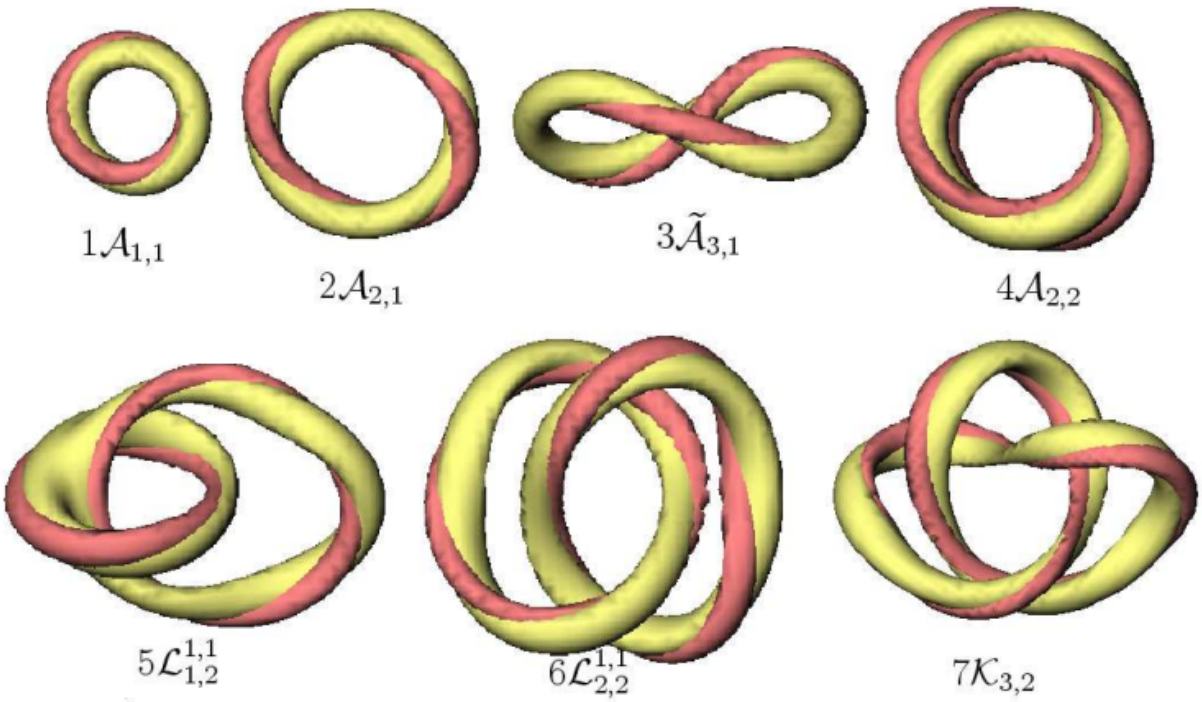

Figure 4.2: Minimal energy known Hopf solitons for $\mathcal{Q} = 1 \ldots 7$, taken from [40]. The position is shown in yellow, with linking shown in red. The position isosurface is close to where $\boldsymbol{\phi}$ is at its furthest point from the vacuum, and the linking isosurface is of a point close to the position on the $\mathcal{S}^2$.

Although Faddeev pondered this idea in 1975, it was not until much later that numerical attempts to construct such solitons took place. Following from this boom in interest, augmented by the ever increasing power to compute solutions, a comprehensive catalogue of solitons has been produced [40, 42, 43, 54–58]. These results confirm that minimal energy solitons take the form of knots and links. Figure 4.2 shows the known minimal energy solutions for Hopf index one to seven [40]. Higher charge solutions can also be found in [40]. They can be listed as follows.

The Hopf index one and two solitons are axially symmetric. They are of the type $\mathcal{A}_{1,1}$ and $\mathcal{A}_{2,1}$. The position consists of a single circular string, with a preimage of any other point of the $\mathcal{S}^2$ linking exactly once ($\mathcal{Q} = 1$) or twice ($\mathcal{Q} = 2$). Isosurfaces of constant ϕ_3 form tori of increasing size as $\phi_3 \to 1$. Note that $\phi_3 \to 1$ at both spatial infinity and the origin (centre of the circular string). The Hopf index three soliton is a twisted ring, denoted $\tilde{\mathcal{A}}_{3,1}$. It has similar characteristics to the $\mathcal{Q} = 1, 2$ solutions. Its position is along one closed loop but in this case the winding has caused the circular ring to buckle. It still has the same linking structure as the axial solutions, with the preimage of any other point on the $\mathcal{S}^2$ linking with the position exactly three times. A twisted axial

structure will appear again in other models permitting Hopf solitons. The buckling is a result of the winding, in this case the field winds around three times for one traversing of the circular string. The final example of axial symmetry in the Skyrme-Faddeev model is at Hopf index four. The minimal energy solution is an $\mathcal{A}_{2,2}$ axial soliton, with the fields winding the position twice as the string is traversed twice. This is like having two axial solitons with $\mathcal{Q}=2$ sat on top of each other. No further known minimal energy solutions have axial symmetry. Clearly, axial solitons are not favourable solutions as the Hopf index increases, and axial $\mathcal{A}_{n,m}$ configurations here only seem to be favoured where $|n-m|$ remains small. Even if they differ by two, the axial symmetry is lost even if the soliton's general structure is preserved. Hopf index five and six solitons are linked configurations, where the structure consists of two closed loops specifying the position linked once. They are $\mathcal{L}^{1,1}_{1,2}$ and $\mathcal{L}^{1,1}_{2,2}$ type configurations, respectively. The $\mathcal{Q}=5$ link has a roughly axial $\mathcal{Q}=1$ component and a perturbed $\mathcal{Q}=2$ component. The linking occurs in a chain configuration, where the length of the chain has been minimised such that the two loops almost touch at the point of linking. The $\mathcal{Q}=6$ link consists of two similar $\mathcal{Q}=2$ perturbed components, with the axial symmetry of the component loops lost. The Hopf index seven soliton is the first example of a knot configuration. It is a trefoil knot, denoted $\mathcal{K}_{3,2}$. It has a rather strange configuration in that there is a twist in the isosurface near to the position as it links through one of the loops of the knot. It represents a rapid winding of the preimages of other points around the position over this particular region of the closed loop. The trefoil knot is the only minimal energy knot configuration in the Hopf index range considered here, although all the further Hopf charges may have static trefoil knots, but none will be the minimal energy solutions. The Hopf index eight minimal energy soliton is similar to the $\mathcal{Q}=6$ link, of type $\mathcal{L}^{1,1}_{3,3}$. It consists of two $\tilde{\mathcal{A}}_{3,1}$ type closed loops, linked once with the loops lying close together. The minimal energy solutions for Hopf index nine, ten and eleven are all three component linked configurations, with each loop linking all the others exactly twice. The $\mathcal{Q}=9$ $\mathcal{L}^{2,2,2}_{1,1,1}$ loops are positioned in a line, like that described earlier in terms of rational maps. The $\mathcal{Q}=10$ $\mathcal{L}^{2,2,2}_{1,1,2}$ loops are positioned in a triangular type formation, as are the $\mathcal{Q}=11$ $\mathcal{L}^{2,2,2}_{1,2,2}$ loops. Details of Hopf index twelve to sixteen solutions can be found in [40].

The present work on knotted and linked configurations only relates to the Skyrme-

Faddeev model. It would be useful to investigate knotted and linked configurations in other models permitting Hopf solitons. This would allow for universal features of Hopf soliton models to be conjectured, for example, do knots even exist in models other than the Skyrme-Faddeev model as minimal energy configurations, or even as static configurations? Do all Hopf soliton models have the same structure of solutions, with axial solutions only existing for lower Hopf charges and linked and knotted configurations becoming favoured later? The next chapters will investigate knotted and linked configurations in some other models that permit Hopf solitons.

Chapter 5

Solitons in the Nicole Model

5.1 Introduction

If one were to trivially extend the O(3) sigma model from two to three spatial dimensions,

$$\mathcal{L} = \partial_\mu \boldsymbol{\phi} \cdot \partial^\mu \boldsymbol{\phi}, \tag{5.1.1}$$

Derrick's theorem [6] proves that no static, finite energy solutions other than the vacuum exist. Usually, a fourth order Skyrme-like term is added to the Lagrangian, such as the Skyrme-Faddeev model [54], to get around this problem. Instead, one can consider taking the O(3) sigma model in 3+1 dimensions raised to a non-integer power, namely;

$$\mathcal{L}_{Ni} = \left(\partial_\mu \boldsymbol{\phi} \cdot \partial^\mu \boldsymbol{\phi}\right)^{\frac{3}{2}}, \tag{5.1.2}$$

where $\boldsymbol{\phi}$ is a three-component unit vector, $\boldsymbol{\phi} = (\phi_1, \phi_2, \phi_3)$. Derrick's theorem allows for the existence of static, finite energy solutions in this case without the need to add a term that is quadratic in derivatives. Solutions here will also have a Hopf index associated with them, $\mathcal{Q}$. To have a finite energy the field must tend to a constant at spatial infinity, taken to be $\boldsymbol{\phi} = (0, 0, 1)$. This leads to the soliton's position being defined where the field is furthest from this vacuum, i.e. $\boldsymbol{\phi} = (0, 0, -1)$. In fact a static, spherically symmetric soliton with Hopf index one has been found analytically [8]. This takes the form of a stereographic projection of the natural Hopf map. Take natural coordinates Φ_a on $\mathcal{S}^3$, where $a = 1 \ldots 4$ and $\Phi_a \Phi_a = 1$ - similar to the real and imaginary components of the

two complex coordinates on the $\mathcal{S}^3$, $Z_1, Z_0 \in \mathbb{C}$. Now define the compactification using stereographic projection, such that

$$\Phi_i = \frac{2\sigma x_i}{\sigma^2 + r^2}\,, \qquad \Phi_4 = \frac{\sigma^2 - r^2}{\sigma^2 + r^2}, \tag{5.1.3}$$

where x_i, $i = 1..3$ are coordinates on the compactified space, with $r = \sqrt{x_i x_i}$. The parameter, σ, is an arbitrary real constant, associated with the scale of the soliton. The standard Hopf map with Hopf index 1 (4.1.4) then has the form

$$W = \frac{\Phi_1 + i\Phi_2}{\Phi_4 + i\Phi_3} = \frac{2\,(x_1 + ix_2)}{1 - r^2 + 2ix_3} \quad \equiv \quad \frac{\phi_1 + i\phi_2}{1 + \phi_3}, \tag{5.1.4}$$

using natural coordinates on $\mathcal{S}^2$, ϕ_i with $\phi_i\phi_i = 1$ (the Hopf map, $\boldsymbol{\phi}$) which are therefore given as

$$\phi_1 = 2\,(\Phi_1\Phi_4 + \Phi_2\Phi_3) \tag{5.1.5}$$

$$\phi_2 = 2\,(\Phi_1\Phi_3 - \Phi_2\Phi_4) \tag{5.1.6}$$

$$\phi_3 = \Phi_4^2 + \Phi_3^2 - \Phi_2^2 - \Phi_1^2. \tag{5.1.7}$$

The static Lagrangian density of the Nicole model, in terms of W is given by

$$\mathcal{L}'_{Ni} = \frac{-8\left(\partial_i\overline{W}\partial_i W\right)^{\frac{3}{2}}}{\left(1 + \overline{W}W\right)^3}. \tag{5.1.8}$$

The standard Hopf map (5.1.4) satisfies the equations of motion for (5.1.8) and is indeed a static solution. The Lagrangian density of the standard Hopf map is found to be spherically symmetric, giving a total static energy of

$$\mathcal{L}'_{Ni} = \frac{-128\sqrt{2}}{(1 + r^2)^3} \quad \Longrightarrow \quad E = \int -\mathcal{L}'_{Ni} d^3x = 32\sqrt{2}\pi^2. \tag{5.1.9}$$

The total static energy of a given solution is

$$E_{Ni} = \frac{1}{32\sqrt{2}\pi^2} \int \left(\partial_i\boldsymbol{\phi} \cdot \partial_i\boldsymbol{\phi}\right)^{\frac{3}{2}}\, d^3x \quad \text{where} \quad \left(\partial_i\boldsymbol{\phi} \cdot \partial_i\boldsymbol{\phi}\right)^{\frac{3}{2}} \equiv \Lambda^{\frac{3}{2}}. \tag{5.1.10}$$

This rescaling gives the Hopf index one soliton an energy $E_{Ni} = 1$. Indeed, closer examination of this solution shows that near where W diverges, the solution has the appearance of a closed vortex ring, twisting once around the divergent ring. This matches up with

the description given in the previous chapter in terms of baby Skyrmions.

Axially symmetric solitons for Hopf index $\mathcal{Q} > 1$ have been found [59] and it has been shown that each topological sector is separated by an infinite energy barrier [60]. It makes sense to re-express the equations of motion in terms of toroidal coordinates, (η, ξ, φ), i.e.

$$x = \frac{\sinh(\eta)\cos(\varphi)}{\cosh(\eta) - \cos(\xi)}, \quad y = \frac{\sinh(\eta)\sin(\varphi)}{\cosh(\eta) - \cos(\xi)}, \quad z = \frac{\sin(\xi)}{\cosh(\eta) - \cos(\xi)}, \tag{5.1.11}$$

taking a unit ring radius. It is then simple to apply an axially symmetric ansatz for W, the complex field describing the Hopf map, up to a profile function, i.e.

$$W = \rho(\eta) e^{in\xi + im\varphi} \quad n, m \in \mathbb{Z}, \tag{5.1.12}$$

where m describes the winding about φ, i.e. around the ring and n describes the winding about ξ, i.e. around the cross-section for a given η, which is the minor torus radius - the distance away from the core of the torus. This idea follows from the conformal symmetry of the Nicole model and $(\hat{\boldsymbol{e}}_\eta, \hat{\boldsymbol{e}}_\xi, \hat{\boldsymbol{e}}_\varphi)$ form an orthonormal frame in $\mathbb{R}^3$. Using the gradient components of this frame, the ansatz (5.1.12) can be inserted into the equations of motion, leading to a nonlinear ordinary differential equation in the profile function $\rho(\eta)$. In fact, this is the Hopf map (5.1.4) when $\rho = \sinh\eta$, with $n, m = 1$. The resulting energies grow linearly with Hopf index, which suggests that axial solitons will not be the global minima for large enough $\mathcal{Q}$ as the order of growth in energy should be proportional to $\mathcal{Q}^{3/4}$. The energies for $\mathcal{Q} = 1 \ldots 5$ have been computed to be [59]:

$\mathcal{A}_{1,1}$		$\mathcal{A}_{2,1}$		$\mathcal{A}_{3,1}$		$\mathcal{A}_{2,2}$		$\mathcal{A}_{4,1}$		$\mathcal{A}_{5,1}$
0.99958		1.85697		2.92275		3.19789		3.79963		5.33265

The linear growth in energy of the axial solutions is most evident for large Hopf index. A modified version of the Nicole model has also been investigated analytically [61]. An additional function is added to break the $O(3)$ symmetry, i.e.

$$\mathcal{L} = \frac{1}{2}\sigma(\boldsymbol{\phi})\left(\partial^\mu \boldsymbol{\phi} \cdot \partial_\mu \boldsymbol{\phi}\right)^{\frac{3}{2}}. \tag{5.1.13}$$

The Nicole model is recovered when σ is simply a constant. For $\mathcal{Q} = n^2$, where $m = n$, the energy of the axial solutions goes like $\mathcal{Q}^{3/2}$ in these models. Each solution calculated

relates to a different modified model and is toroidal in nature. This shows the existence of exact hopfions with higher than one topological charge in the modified Nicole models. The discussion of solutions to follow will relate only to the Nicole model.

5.2 Volume Preserving Flow

Finding other solutions to the field equations of (5.1.10) requires solving the full set of static equations. One method of finding static solutions is gradient flow. An energy minimising flow of (5.1.10) would take $\boldsymbol{\phi}$ away from the unit sphere. A Lagrange multiplier can be added to this system to preserve the unit length. If we take the static energy density to be

$$\mathcal{E} = \Lambda^{\frac{3}{2}} + \lambda \left(1 - \boldsymbol{\phi} \cdot \boldsymbol{\phi}\right), \tag{5.2.1}$$

then λ can be found either from the equation of motion, or from the gradient flow equations where it is required that the flow and field are orthogonal, keeping $\boldsymbol{\phi}$ on the unit sphere. In either case

$$\lambda = -3\Lambda^{\frac{1}{2}} \boldsymbol{\phi} \cdot \nabla^2 \boldsymbol{\phi} \equiv 3\Lambda^{\frac{3}{2}}. \tag{5.2.2}$$

This makes the gradient flow equations for this system

$$\frac{\partial \boldsymbol{\phi}}{\partial t_0} = -\frac{\delta \mathcal{E}}{\delta \boldsymbol{\phi}} = 3\left(\Lambda^{\frac{1}{2}} \nabla^2 \boldsymbol{\phi} + \left(\partial_i \partial_j \boldsymbol{\phi} \cdot \partial_j \boldsymbol{\phi}\right) \Lambda^{-\frac{1}{2}} \partial_i \boldsymbol{\phi}\right) + \lambda \boldsymbol{\phi} \equiv 3\boldsymbol{F}. \tag{5.2.3}$$

This flow will keep $\boldsymbol{\phi}$ on the unit sphere as $\boldsymbol{F} \cdot \boldsymbol{\phi} = 0$ but, due to the scale invariance of the problem, it is likely that a solution will tend to shrink when placed on a lattice until it eventually falls through. This is much like what would happen in an O(3) sigma model. To set a scale for the problem, a volume term can be introduced and the volume preserving flow, introduced in chapter 2, can be used. This volume would introduce a size of a given solution if properly defined. It is then possible to flow in a direction that keeps this size (and so the chosen scale) constant. It seems logical to choose a function of ϕ_3 to define this volume if the boundary conditions taken are that $\phi_3 \to 1$, with the soliton's location defined by when $\phi_3 = -1$. In both cases the other two field components

are obviously zero. A possible volume density of the soliton is

$$\upsilon = \frac{1}{2}(1-\phi_3). \tag{5.2.4}$$

It is important to remember here that in order to keep $\boldsymbol{\phi}$ on the unit sphere, another Lagrange multiplier, λ_v, must be used when calculating the volume flow. λ_v can be calculated in the same way as with (5.2.2). The flow that changes the volume is

$$\frac{\partial \boldsymbol{\phi}}{\partial t_1} = -\frac{\delta \upsilon}{\delta \boldsymbol{\phi}} = \frac{\boldsymbol{e}_3}{2} - \lambda_v \boldsymbol{\phi} \equiv \boldsymbol{f}, \tag{5.2.5}$$

where $\lambda_v = \phi_3/2$ and $\boldsymbol{e}_3$ is the unit vector in the ϕ_3 direction of field space. A direction with unit length can be found like that set out in chapter 2, but since the normalisation will cancel later this is not necessary. The volume preserving flow (2.1.38) is then

$$\begin{aligned}
\frac{\partial \boldsymbol{\phi}}{\partial t} &= \boldsymbol{F} - \left\langle \widehat{\boldsymbol{f}} \cdot \boldsymbol{F} \right\rangle \widehat{\boldsymbol{f}} = \boldsymbol{F} - \frac{\langle \boldsymbol{f} \cdot \boldsymbol{F} \rangle}{\langle \boldsymbol{f} \cdot \boldsymbol{f} \rangle} \boldsymbol{f} = \boldsymbol{F} - \left[\frac{1}{2\|\boldsymbol{f}\|^2} \int \boldsymbol{f} \cdot \boldsymbol{F} \, d^2x \right] \boldsymbol{f} \\
&= \boldsymbol{F} - \left[\frac{1}{2\|\boldsymbol{f}\|^2} \int (\boldsymbol{e}_3 - \phi_3 \boldsymbol{\phi}) \cdot \left(\left(\Lambda^{\frac{1}{2}} \nabla^2 \boldsymbol{\phi} + (\partial_i \partial_j \boldsymbol{\phi} \cdot \partial_j \boldsymbol{\phi}) \, \Lambda^{-\frac{1}{2}} \partial_i \boldsymbol{\phi} \right) + \lambda \boldsymbol{\phi} \right) d^2x \right] \boldsymbol{f} \\
&= \boldsymbol{F} - \left[\frac{1}{4\|\boldsymbol{f}\|^2} \int \left(\Lambda^{\frac{1}{2}} \nabla^2 \phi_3 + (\partial_i \partial_j \boldsymbol{\phi} \cdot \partial_j \boldsymbol{\phi}) \, \Lambda^{-\frac{1}{2}} \partial_i \phi_3 + \lambda \phi_3 \right) d^3x \right] (\boldsymbol{e}_3 - \phi_3 \boldsymbol{\phi}) \\
&= \left(\Lambda^{\frac{1}{2}} \nabla^2 \boldsymbol{\phi} + (\partial_i \partial_j \boldsymbol{\phi} \cdot \partial_j \boldsymbol{\phi}) \, \Lambda^{-\frac{1}{2}} \partial_i \boldsymbol{\phi} \right) + \lambda \boldsymbol{\phi} \\
&\quad - \frac{\int \left(\Lambda^{\frac{1}{2}} \nabla^2 \phi_3 + (\partial_i \partial_j \boldsymbol{\phi} \cdot \partial_j \boldsymbol{\phi}) \, \Lambda^{-\frac{1}{2}} \partial_i \phi_3 + \lambda \phi_3 \right) d^3x}{\int (1 - \phi_3^2) \, d^3x} (\boldsymbol{e}_3 - \phi_3 \boldsymbol{\phi}),
\end{aligned} \tag{5.2.6}$$

$\boldsymbol{\phi} \cdot \boldsymbol{F} = 0$, since any flow of the field must be perpendicular to the field itself and so keeping it on the unit sphere. In vector form, this looks like

$$\frac{\partial \boldsymbol{\phi}}{\partial t} = \begin{pmatrix} \Lambda^{\frac{1}{2}} \nabla^2 \phi_1 + (\partial_i \partial_j \boldsymbol{\phi} \cdot \partial_j \boldsymbol{\phi}) \, \Lambda^{-\frac{1}{2}} \partial_i \phi_1 + \lambda \phi_1 + A \phi_1 \phi_3 \\ \Lambda^{\frac{1}{2}} \nabla^2 \phi_2 + (\partial_i \partial_j \boldsymbol{\phi} \cdot \partial_j \boldsymbol{\phi}) \, \Lambda^{-\frac{1}{2}} \partial_i \phi_2 + \lambda \phi_2 + A \phi_2 \phi_3 \\ \Lambda^{\frac{1}{2}} \nabla^2 \phi_3 + (\partial_i \partial_j \boldsymbol{\phi} \cdot \partial_j \boldsymbol{\phi}) \, \Lambda^{-\frac{1}{2}} \partial_i \phi_3 + \lambda \phi_3 - A (1 - \phi_3^2) \end{pmatrix}, \tag{5.2.7}$$

where

$$A = \frac{\int \left(\Lambda^{\frac{1}{2}} \nabla^2 \phi_3 + (\partial_i \partial_j \boldsymbol{\phi} \cdot \partial_j \boldsymbol{\phi}) \, \Lambda^{-\frac{1}{2}} \partial_i \phi_3 + \lambda \phi_3 \right) d^3x}{\int (1 - \phi_3^2) \, d^3x}. \tag{5.2.8}$$

This will preserve the volume, V, and reduce the energy using (5.2.2) since $\left\langle \boldsymbol{f}, \dot{\boldsymbol{\phi}} \right\rangle = 0$, like that found in chapter 2, from (2.1.39) and (2.1.42), i.e.

$$\frac{dV}{dt} = \int \frac{dv}{dt}\, d^3x = \int \frac{\partial v}{\partial \boldsymbol{\phi}} \cdot \frac{\partial \boldsymbol{\phi}}{\partial t}\, d^3x = -\int \boldsymbol{f} \cdot \frac{\partial \boldsymbol{\phi}}{\partial t}\, d^3x = -\left\langle \boldsymbol{f}, \dot{\boldsymbol{\phi}} \right\rangle = 0. \tag{5.2.9}$$

Also note that this flow will keep the field on the unit sphere as $\boldsymbol{\phi} \cdot \dot{\boldsymbol{\phi}} = 0$. Gradient flow in this manner will preserve the volume V of any initial conditions used. It can also be easily shown that this flow will also minimise the energy to a local minima.

$$\begin{aligned} \frac{dE}{dt} &= \int \frac{d\mathcal{E}}{dt}\, d^3x = \int \frac{\partial \boldsymbol{\phi}}{\partial t} \cdot \frac{\delta \mathcal{E}}{\delta \boldsymbol{\phi}}\, d^3x = -\int \frac{\partial \boldsymbol{\phi}}{\partial t} \cdot \boldsymbol{F}\, d^3x = -\left\langle \dot{\boldsymbol{\phi}}, \boldsymbol{F} \right\rangle \\ &= -\left\langle \dot{\boldsymbol{\phi}}, \dot{\boldsymbol{\phi}} + \left\langle \hat{\boldsymbol{f}}, \boldsymbol{F} \right\rangle \hat{\boldsymbol{f}} \right\rangle = -\left\langle \dot{\boldsymbol{\phi}}, \dot{\boldsymbol{\phi}} \right\rangle \leq 0, \end{aligned} \tag{5.2.10}$$

and so the energy is never increasing, using $\left\langle \boldsymbol{f}, \dot{\boldsymbol{\phi}} \right\rangle = 0$. These should both be clear from the geometrical construction of the volume preserving flow.

The numerical calculations will occur in a finite region Ω, taken to be a cube, where the field will be fixed on $\partial\Omega$ to $\boldsymbol{\phi} = \boldsymbol{e}_3$. It is clear from the $\mathcal{Q} = 1$ exact solution, (5.1.4) (5.1.7), that the field goes to the vacuum slowly, like $1/r$. Making Ω large enough will allow for this behaviour, but as most of the energy will be concentrated nearer to the position than $\partial\Omega$ it is more useful to reduce the size Ω to have more lattice sites in the area which the energy density is greatest. This should not have a noticeable effect on the overall energy. In fact, varying the size of Ω and V alters the energy $\mathcal{O}(1\%)$. Calculations will be made on a 151^3 or 200^3 lattice, with unit spacing and an explicit method with first order accuracy with a timestep $\Delta t = 0.1$ will be used to evolve the field.

The volume function V, will be finite when Ω is a finite region. In the full continuum limit, $V_\Omega \to \infty$ and as noted previously, the field decays like $1/r$. This would result in an infinite volume since the integral will be logarithmically divergent. It is then sufficient to take the volume density (5.2.4), raised to a higher power:

$$\upsilon' = \left(\frac{1 - \phi_3}{2}\right)^a, \quad \boldsymbol{f}' = 2^{-a} a \left(\boldsymbol{e}_3 - \phi_3 \boldsymbol{\phi}\right) (1 - \phi_3)^{a-1}, \quad a \in \mathbb{N}. \tag{5.2.11}$$

The volume integral, in cylindrical coordinates (ρ, θ, z), for the Hopf map is given by

$$V = \int \left(\frac{1 - \phi_3}{2}\right)^a d^3x = 4^{a+1}\pi \int_0^{L_\rho} \int_0^{L_z} \frac{\rho^{2a+1}}{\left(\rho^2 + z^2 + 1\right)^{2a}} d\rho dz. \tag{5.2.12}$$

Taking $a \geq 2$ results in a quick enough fall off of the field and so the volume term in the continuum theory remains finite. It will alter the final form of (5.2.7) slightly with the addition of some extra terms, but the process is qualitatively the same. The results that will follow use $a=1$, although similar results were found for $a=3$.

5.3 Numerical Results

The initial conditions used as a starting point of the gradient flow will have a large effect on the static solutions the flow will reach. This is because gradient flow finds local minima, which are not necessarily the global minima. It is quite reasonable to use the exact solution for a charge 1 soliton as a check. It is expected there will be some small increase in the energy as a result of putting the solution into a box, since the field tends to its vacuum solution very slowly. The majority of the energy will be contained in the area surrounding the soliton's location, so it seems more reasonable to devote lattice points to this region rather than the tail region. There are no exact solutions with a higher Hopf index so other initial conditions must be used. The rational maps set out in the previous section will be used to generate solutions.

A 150^3 lattice with lattice spacing $\Delta x=1$ will be used to investigate Hopf index $1\ldots8$ and a 200^3 lattice with the same spacing will be used for larger $\mathcal{Q}$. As $\mathcal{Q}$ increases, so must the volume of the soliton as, in general, higher charged Hopf solitons will have a longer position string length. Taking a volume, V, that is not large enough can result in unwinding as the soliton scale becomes too small. Too large a volume may cause the fields to be influenced by the boundary. There will be a reasonably large range of volumes for which neither of these issues arise. The larger grid is used for $\mathcal{Q} > 8$ as larger volumes are required. For the most part, solutions with the same Hopf index will be evaluated for similar volumes to gain a fair understanding of their relative energies. Varying volumes will only have a weak effect for a reasonable range of values, with variances $\mathcal{O}(1\%)$. The flow will be evolved using an explicit method with a timestep $\Delta t = 0.1$. Energy, volume and inner products will be evaluated by a simple summation over the lattice and derivatives are found to a fourth order accuracy using a finite difference method.

The minimal energy solitons for Hopf index $1-11$ can be found in figure 5.1, while

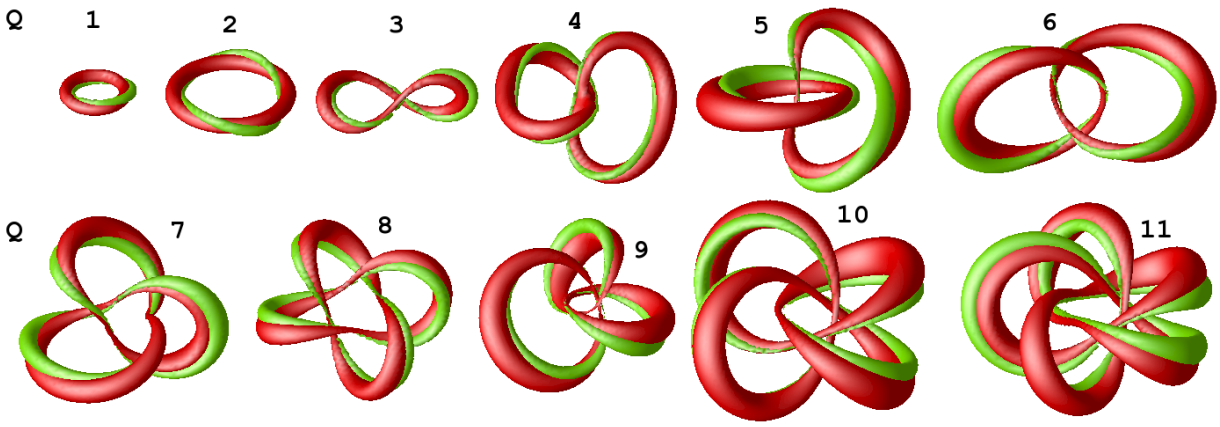

Figure 5.1: Hopf index $\mathcal{Q} = 1 - 11$ minimal energy soliton solutions in the Nicole model. Red surface is a level set, $\phi_3 = -0.9$, close to the solitons position where $\phi_3 = -1$. Green surface is a level set close to $\boldsymbol{\phi} = \left(\sqrt{\mu\,(2-\mu)}, 0, \mu - 1\right)$, with $\mu = 0.1$. This is needed to check the Hopf index.

the solution energies can be found in figure 5.2. A plot of the energy per $\mathcal{Q}^{3/4}$ can also be found in figure 5.2. A full list of static solutions, including initial and final field configurations can be found in figure 5.3 for Hopf index $1-8$ and figures 5.4, 5.5 and 5.6 for Hopf index 9, 10 and 11. The red parts are isosurfaces of $\phi_3 = -0.9$, near to the position and the green surfaces shows the linking of a pre-image curve close to the position.

The minimal energy soliton configurations for Hopf index $\mathcal{Q} = 1-3$ are the same type as that in the Skyrme-Faddeev model [40]. The $\mathcal{Q} = 1$ is a type $\mathcal{A}_{1,1}$ axial configuration. It matches up to the exact solution for a charge one soliton in this model [8] and has a normalised energy of 1.004, which is within $\sim 1/2\%$ of the exact value. The energy is expected to be slightly higher than the exact solution as the soliton falls off to the vacuum very slowly, and putting the soliton in a box forces this to occur more rapidly. This solution is in good agreement with the axial profile function minimisation results seen earlier [59]. As will be the case for all the static configurations in this model, increasing the size of the grid or changing the volume of the soliton will have an effect of about 1% on the energy. This example of the $\mathcal{A}_{1,1}$ had a volume $V = 60000$ where the total volume of the grid is 3375000 for 150^3 lattice points with unit spacing. This volume is $\sim 2\%$ of the total volume, but is not a realistic measure in terms of how the volume is counted. An $\mathcal{A}_{1,1}$ with $V = 60000$ has a $\phi_3 = -1$ ring diameter of around 20 lattice points. The $\mathcal{Q} = 2$ soliton is an $\mathcal{A}_{2,1}$ axial configuration, with an energy of 1.795 for a volume of $V = 57000$. This energy is significantly lower than 1.857 found by profile function minimisation in [59]. A lower energy for the $\mathcal{A}_{2,1}$ configuration would be expected, since

Static Solutions in the Nicole Model									
Q	**Type**	**E**	**Q**	**Type**	**E**	**Q**	**Type**	**E**
1	$\mathcal{A}_{1,1}$	1.004	8	$\mathcal{L}^{2,2}_{2,2}$	5.323	10	$\mathcal{L}^{2,2}_{3,3}$	6.421
2	$\mathcal{A}_{2,1}$	1.795	8	$\mathcal{K}_{3,2}$	5.370	10	$\mathcal{K}_{3,2}$	6.527
3	$\tilde{\mathcal{A}}_{3,1}$	2.528	8	$\mathcal{L}^{1,1}_{3,3}$	5.576	10	$\mathcal{L}^{1,1}_{4,4}$	7.075
3	$\mathcal{A}_{3,1}$	2.623	9	$\mathcal{L}^{2,2,2}_{1,1,1}$	5.740	11	$\mathcal{K}_{5,3}$	6.665
4	$\mathcal{L}^{1,1}_{1,1}$	3.149	9	$\mathcal{K}_{5,2}$	5.882	11	$\mathcal{L}^{2,2,2}_{1,2,2}$	6.729
5	$\mathcal{L}^{1,1}_{1,2}$	3.760	9	$\mathcal{K}_{3,2}$	5.989	11	$\mathcal{L}^{2,2}_{3,4}$	6.943
5	$\mathcal{K}_{3,2}$	3.771	9	$\mathcal{L}^{2,2}_{2,3}$	5.996	11	$\mathcal{K}_{5,2}$	7.054
6	$\mathcal{L}^{1,1}_{2,2}$	4.308	9	$\mathcal{L}^{1,1}_{3,4}$	6.242	11	$\mathcal{L}^{3,3}_{2,3}$	7.131
7	$\mathcal{K}_{3,2}$	4.829	10	$\mathcal{K}_{4,3}$	6.226	11	$\mathcal{K}_{3,2}$	7.179
7	$\mathcal{L}^{1,1}_{2,3}$	4.882	10	$\mathcal{L}^{2,2,2}_{1,1,2}$	6.258			

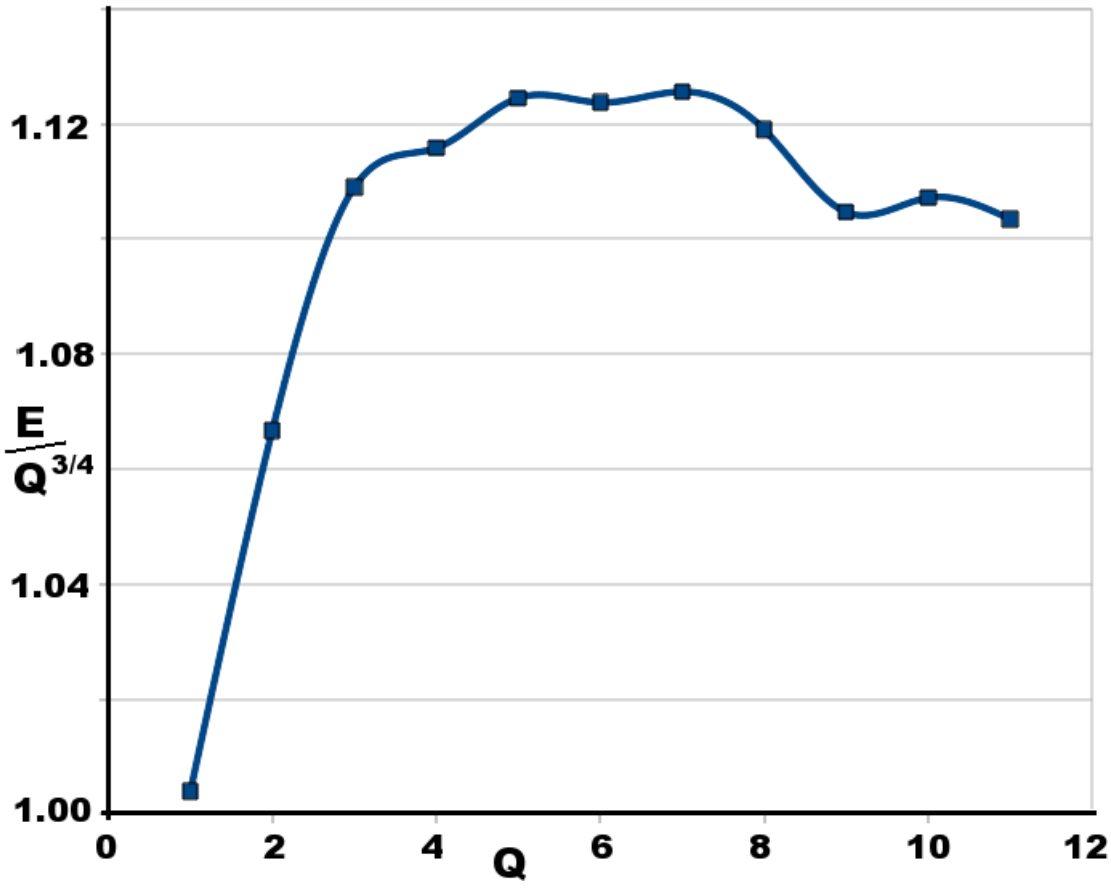

Figure 5.2: (top) Table of the normalised energy of static solutions of Nicole model, for Hopf index $\mathcal{Q} = 1 - 11$. (bottom) Plot of the minimal energy configurations, divided by $\mathcal{Q}^{3/4}$ for each Hopf index.

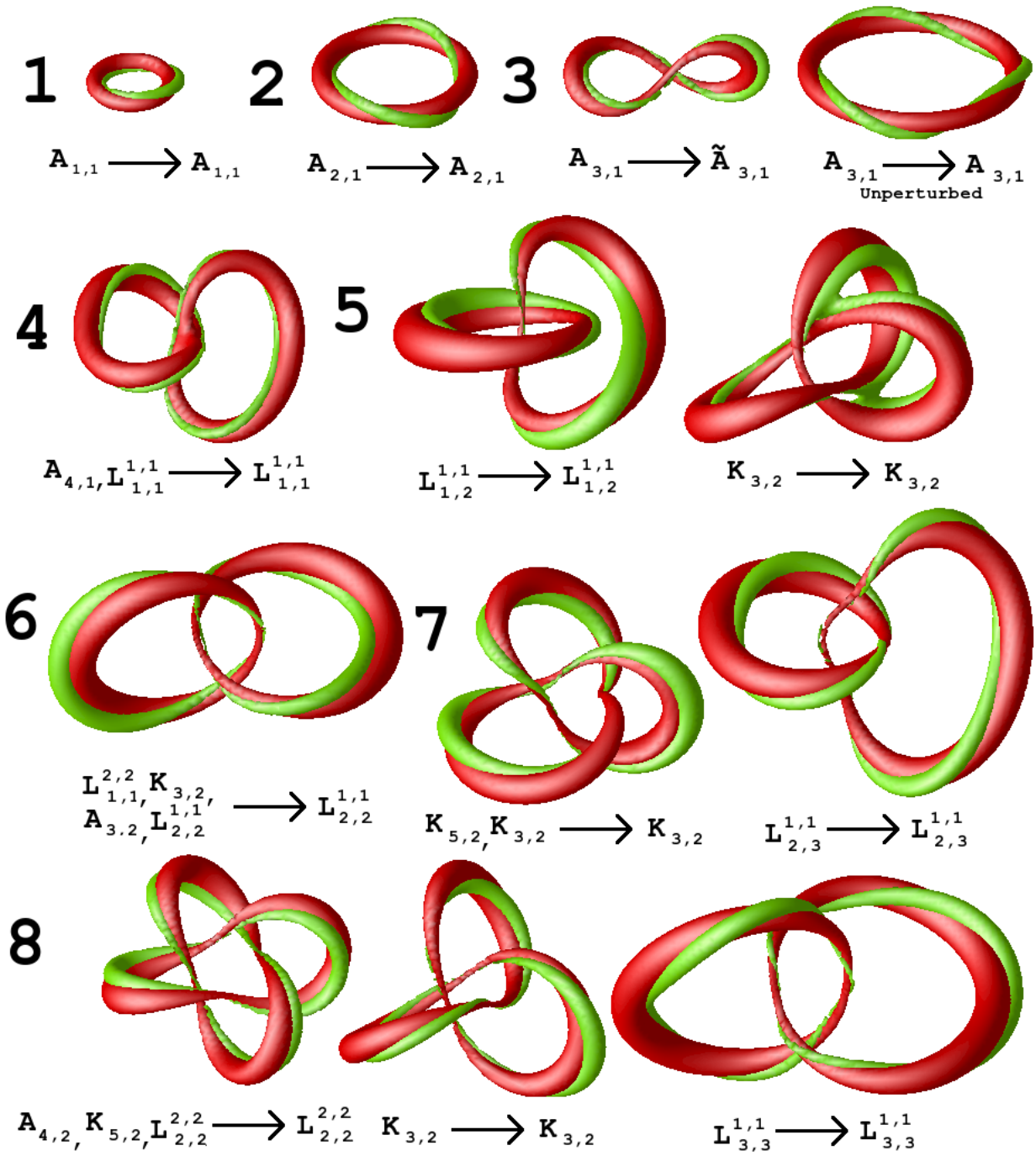

Figure 5.3: Hopf index $\mathcal{Q} = 1 - 8$ static solutions in the Nicole model. The numbers are the Hopf index and both initial and final field configuration types are given below each soliton. Solitons at each Hopf index are ordered lowest static energy to the left and highest static energy to the right. Not all solutions are stable, some may be saddle points or local minima in the restricted flow landscape but not exist in the full energy landscape. Surfaces are same as in figure 5.1.

the ansatz used in [59] reduces the equations to a profile function problem but it is not itself a fully axially symmetric ansatz (there is still another free parameter to fix). An $\mathcal{A}_{1,2}$ type initial configuration attempts to unwind itself towards the $\mathcal{A}_{2,1}$ configuration, but gets stuck during the volume preserving minimisation. This issue could be an artefact

of this minimisation process. The lack of a static $\mathcal{A}_{1,2}$ configuration in this model would agree with [59], which suggests that the $\mathcal{A}_{1,2}$ has a higher energy than the $\mathcal{A}_{2,1}$ if it exists. The results here suggests that a static configuration of this type does not exist in the Nicole model. The same is true for all other $\mathcal{A}_{n,m}$ with $m > n$ with this energy minimisation. In fact, the $\mathcal{Q}=2$, $\mathcal{A}_{2,1}$ is the last axially symmetric soliton found for the Nicole model. Like with the Skyrme-Faddeev model, the $\mathcal{Q}=3$ minimal energy soliton is a single twisted ring, denoted $\tilde{\mathcal{A}}_{3,1}$. It has an energy of 2.528 for $V=62000$. The ring twists into a chain-link type shape with two semicircles linked by two straight sections, with the straight sections then bent around so that the two planes containing each semicircle part are perpendicular. An axial $\mathcal{A}_{3,1}$ can be created if a totally axially symmetric initial condition is chosen. The ring does not know in which direction to squash and twist. A static configuration of this type has an energy of 2.623 for $V=53000$. It is a saddle point both in the volume preserving minimisation landscape, as well as the general energy minimisation landscape, as it is held by symmetry. The results of both the twisted ring and the axial saddle point are well below the axial solution found in [59].

The first difference in minimal energy field configurations in the Nicole and Skyrme-Faddeev [40] models is at Hopf index $\mathcal{Q}=4$. The static configuration is an $\mathcal{L}^{1,1}_{1,1}$ type field, with two $\mathcal{Q}=1$ components linked once. The energy of this configuration is 3.149 for a $V=75000$ sized configuration, just below the energy of the axial solution found in [59]. It can be seen in figure 5.3 and figure 5.1 that the two rings are perturbed towards a twisted oval shape and link with the $\phi_3=-1$ strings almost touching. The evolution from the rational map (4.2.7) with $n=1$ will first move towards an $\mathcal{A}_{2,2}$ like field, with the two strings almost on top of each other but still linked and then move out away from each other towards the configuration in figure 5.3 and figure 5.1. This implies the field configuration of a rational map like (4.2.7) is not a good approximation of an $\mathcal{L}^{1,1}_{1,1}$ type soliton in the Nicole model. Starting from an $\mathcal{A}_{4,1}$ field, the axial configuration twists during the minimisation like at $\mathcal{Q}=3$. The twisting takes a long gradient flow time, eventually reaching a single string almost comparable to the $\mathcal{L}^{1,1}_{1,1}$ with the middles of the twisted ring almost linking. This configuration has an energy of 3.160 when sized at $V=55000$. This inability to re-link to form the minimal energy field configuration could relate to zero modes associated with the volume preserving minimisation. Further

details of this will be discussed later. During the evolution of a $\mathcal{A}_{2,2}$ type field, (4.2.4) with $n, m = 2$, the two strings link together into a single string with one crossing. This string then attempts to untwist but gets stuck during the process. This issue could be caused by restricting the minimisation to volume preserving flow. A configuration of this type of a similar size to the other $\mathcal{Q} = 4$ solutions gets stuck with an energy of 3.180. As the strings connect and unravel, the isosurface $\phi_3 = -0.9$ becomes thin in the region where the field twists the most. It can then fall through the lattice if it becomes too thin and break the string. This pinching is a common problem with the minimisation of configurations using the volume preserving gradient flow method in the Nicole model. The configurations needs to have larger volumes to stop this occurring, meaning the field near to $\phi_3 = -1$ is covered by more points.

The Hopf index 5 minimal energy soliton is of the same type as with the Skyrme-Faddeev model [40], an $\mathcal{L}^{1,1}_{1,2}$. The static energy for a $V = 160000$ sized $\mathcal{L}^{1,1}_{1,2}$ is 3.760. A larger size is needed here as the $\mathcal{Q} = 2$ string part of the link tends to pinch in the section which links through the $\mathcal{Q} = 1$ string. This final configuration is also obtained from an $\mathcal{A}_{5,1}$ type initial condition, although as with the $\mathcal{A}_{4,1} \rightarrow \mathcal{L}^{1,1}_{1,1}$ transition this takes a lot of computational time. A $\mathcal{K}_{3,2}$ type field configuration is a stationary point of the energy functional restricted to volume preserving flow. A $V = 150000$ sized static solution has an energy of 3.771. Both field configurations can be seen in figure 5.3. The $\mathcal{K}_{3,2}$ configuration appears to be attempting to reconnect, most likely to move towards an $\mathcal{L}^{1,1}_{1,2}$ field configuration. This limitation in reconnection could be an artefact of the volume preserving flow used. It has already been seen that for certain configurations of domain walls forming double bubbles, stationary points in the energy functional occur when energy minimisation is restricted to be volume preserving. This could also occur in the Nicole model and will be discussed briefly later.

At Hopf index 6, the number of possible configurations begins to increase, although only one type of static solution exists. The soliton here is an $\mathcal{L}^{1,1}_{2,2}$ linked configuration, with a $V = 240000$ size field having an energy of 4.310. The field configuration here is two axial $\mathcal{Q} = 2$'s linked so that the planes of axial symmetry are approximately perpendicular. This configuration is also reached starting from a rational map of the types;

$$\mathcal{L}^{2,2}_{1,1} \rightarrow \mathcal{L}^{1,1}_{2,2} \text{ :- Energy 4.380 with } V = 215000,$$

$\mathcal{K}_{3,2} \rightarrow \mathcal{L}^{1,1}_{2,2}$:- Energy 4.338 with $V = 140000$,

$\mathcal{A}_{3,2} \rightarrow \mathcal{L}^{1,1}_{2,2}$:- Energy 4.290 with $V = 175000$, using a 200^3 grid.

A lower minimal energy solution was found for $\mathcal{Q} = 6$ when starting from a knot rational map (4.2.6), setting $a = 4, b = 2, \alpha = 1, \beta = 1$. It has twisted components like the $\mathcal{Q} = 4$ soliton and a $V = 220000$ sized field had an energy of 4.269. With almost all initial configurations, the static solution was the type in figure 5.1.

The first minimal energy knot soliton occurs at Hopf index 7, like in the Skyrme-Faddeev model [40], although again the $\phi_3 = -1$ string (like with the $\mathcal{Q} = 5\,\mathcal{L}^{1,1}_{1,2}$) is orientated differently in the Nicole model. This knot is a $\mathcal{K}_{3,2}$ type with an energy of 4.829 for a $V = 160000$. There is also a second static solution to the Nicole model under volume preserving gradient flow which is an $\mathcal{L}^{1,1}_{2,3}$ type field, which has an energy of 4.882 for $V = 180000$. This configuration needs a large size as it is very susceptible to pinching of the $\phi_3 = -1$ strings in the linking region, which is likely a result of the volume preserving flow rather than a stable local minima in full energy landscape. Both configurations can be seen in figure 5.3. Starting from a $\mathcal{K}_{5,2}$ or an $\mathcal{L}^{2,2}_{1,2}$ field configuration also leads towards a $\mathcal{K}_{3,2}$ type configuration.

Hopf index 8 permits many possible configurations. A list can be found in the rational map section of the previous chapter. As has been seen with $\mathcal{Q} = 5, 7$ some configuration types can be found to be static solutions of the volume preserving minimisation, but they may not be static solutions of the energy when not restricted to volume preservation. Figure 5.3 shows the range of solutions found. In fact, more initial configurations lead to minima in the volume preserving minimisation than to the calculated global minimum configuration. There are three static configurations resulting from volume preserving minimisation, two links and a knot. The minimal energy configuration is an $\mathcal{L}^{2,2}_{2,2}$ link, with two $\mathcal{Q} = 2$ components linked twice. Each component is twisted similarly to the $\mathcal{Q} = 3$ $\tilde{\mathcal{A}}_{3,1}$ axial solution. Each link has the same orientation of twist and they appear congruent. For a volume $V = 120000$, the energy is found to be 5.323. This configuration is also reached when starting from $\mathcal{A}_{4,2}$ and $\mathcal{K}_{5,2}$ type field configurations:

$\mathcal{K}_{5,2} \rightarrow \mathcal{L}^{2,2}_{2,2}$:- Energy 5.381 with $V = 140000$,

$\mathcal{A}_{4,2} \rightarrow \mathcal{L}^{2,2}_{2,2}$:- Energy 5.363 with $V = 220000$, using a 200^3 grid.

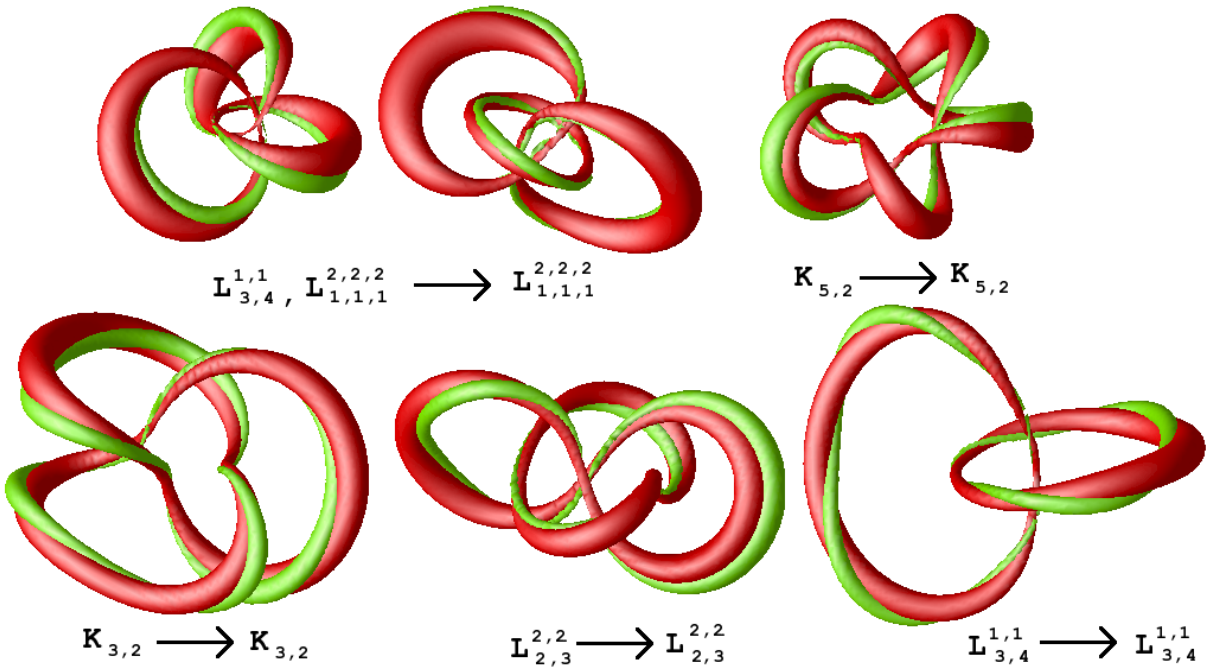

Figure 5.4: Hopf index $\mathcal{Q} = 9$ static solutions in the Nicole model. Initial and final field configuration types are given below each soliton. Surfaces are same as in figure 5.1. Solitons at each Hopf index are ordered lowest static energy to the left and highest static energy to the right. Not all solutions are stable, some may be saddle points or local minima in the restricted flow landscape but not exist in the full energy landscape.

With further time, these solutions would likely minimise to a lower energy but the final form of the field is of more interest. A static $\mathcal{K}_{3,2}$ configuration was also found with energy 5.370 for $V = 230000$. Parts of the position string become very thin at this energy and taking a small volume will lead to the field configuration unwinding as the scale of the string falls through the lattice. The final static configuration under volume preserving flow is an $\mathcal{L}^{1,1}_{3,3}$ link. It had an energy of 5.576 for $V = 155000$. The $\mathcal{L}^{1,1}_{3,3}$ link is the minimal energy configuration in the Skyrme-Faddeev model [40] and no static $\mathcal{L}^{2,2}_{2,2}$ configuration exists. A local minimum $\mathcal{K}_{3,2}$ solution also exists for the Skyrme-Faddeev model which is also not the global minimum.

The results for Hopf charges $\mathcal{Q} = 1 \ldots 8$ all match up well with the results presented in [3]. Those results were found by numerical simulations carried out by Sutcliffe. The results presented here were found independently to those presented in [3]. Investigation into higher $\mathcal{Q}$ were calculated exclusively by this author. All the previous results were calculated on a 150^3 lattice, with the results to follow being calculated on a 200^3 lattice.

As in the Skyrme-Faddeev model, the triple component links of type $\mathcal{L}^{2,2,2}_{1,1,1}$ is the minimal energy solution [40] for Hopf index 9. Minimisation under volume preserving

flow leads to two static solutions of this type and they both have comparable energies. Starting with a triangular type rational map (4.2.17) or an axial $\mathcal{A}_{3,3}$ rational map leads to a line type $\mathcal{L}^{2,2,2}_{1,1,1}$ configuration. A configuration of this type has an energy of 5.809 with $V = 200000$. This configuration can tend to collapse, likely caused by an attempt to connect one outer string with the inner string. An $\mathcal{A}_{3,3}$ type perturbed initial conditions will result in a static line type $\mathcal{L}^{2,2,2}_{1,1,1}$. For $V = 205000$, the resulting line type link has an energy of 5.810. A triangular type $\mathcal{L}^{2,2,2}_{1,1,1}$ configuration is reached under volume preserving minimisation from a line type rational map (4.2.18) or a $\mathcal{L}^{1,1}_{3,4}$ type initial configuration. It has an energy 5.740 for a volume $V = 230000$. These $\mathcal{L}^{2,2,2}_{1,1,1}$ differ from the minimal Skyrme-Faddeev $\mathcal{Q} = 9$ solution in that the central component in the line configuration is much smaller and is reasonably far away from the other two components. The layout of the three components is clearly different in the triangular type solution. The standard $\mathcal{L}^{2,2,2}_{1,1,1}$ rational map found in [40] and introduced in the previous chapter drastically alters itself under volume preserving minimisation, similar to the $\mathcal{L}^{1,1}_{1,1}$ rational map discussed earlier. In general the flow leads to a line type $\mathcal{L}^{2,2,2}_{1,1,1}$ configuration as mentioned above. The slightly lower energy of the triangular configuration could be due to each component unlink having a section that becomes very thin where they all link. In the line configuration, only the two outer components develop a pinching. The inner component remains fairly uniform. These details can be seen in figure 5.4. A second static solution to volume preserving flow occurs with an energy slightly higher than that of the $\mathcal{L}^{2,2,2}_{1,1,1}$ which is a knot of the type $\mathcal{K}_{5,2}$. Its energy is 5.882 for $V = 230000$. This type of configuration is very susceptible to pinching. All other static solutions have a much larger energy, as follows:

$\mathcal{K}_{3,2}$:- Energy 5.989 with $V = 230000$,

$\mathcal{L}^{2,2}_{2,3}$:- Energy 5.996 with $V = 230000$,

$\mathcal{L}^{1,1}_{3,4}$:- Energy 6.242 with $V = 205000$.

The $\mathcal{L}^{2,2}_{2,3}$ and $\mathcal{L}^{1,1}_{3,4}$ are saddle points, resulting in $\mathcal{K}_{3,2}$ and $\mathcal{L}^{2,2,2}_{1,1,1}$ type configurations respectively, depending on the exact nature of the initial conditions. This may be an artefact of the volume preserving flow, as discussed shortly.

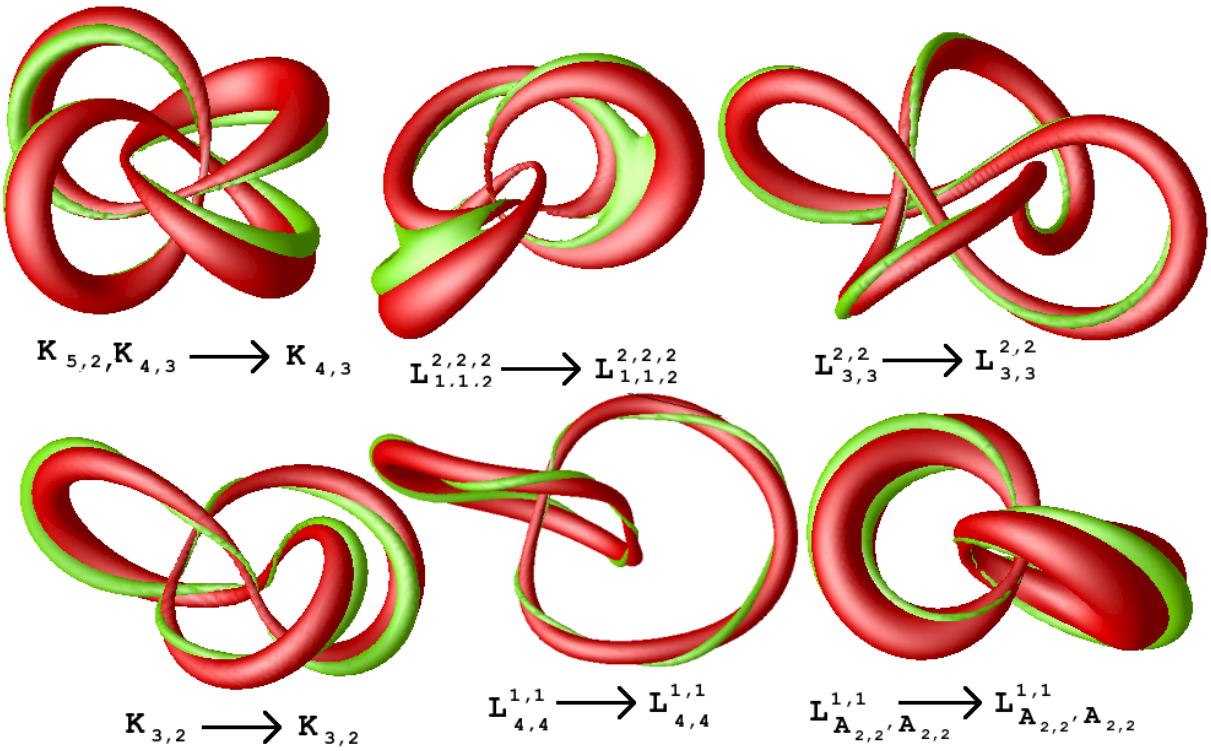

Figure 5.5: Hopf index $\mathcal{Q} = 10$ static solutions in the Nicole model. Initial and final field configuration types are given below each soliton. Surfaces are same as in figure 5.1. Solitons at each Hopf index are ordered lowest static energy to the left and highest static energy to the right. Not all solutions are stable, some may be saddle points or local minima in the restricted flow landscape but not exist in the full energy landscape.

The static solutions of Hopf index 10 can be found in figure 5.5. The minimal energy configuration is a $\mathcal{K}_{4,3}$ knot, it has an energy of 6.226 for a volume $V = 360000$. This configuration is also reached from a $\mathcal{K}_{5,2}$ type configuration. There is also a static solution under volume preserving minimisation with an energy slightly above this which is of the same type as the minimal configuration [40] in the Skyrme-Faddeev model, an $\mathcal{L}^{2,2,2}_{1,1,2}$ link. It has an energy of 6.258 for a volume $V = 325000$, but it may just be a stationary point of the energy functional restricted to volume preserving deformations. It can be seen in figure 5.5 that the three components become very thin around the linking points (a good reason for the energy to be so low) and the linking curve seems to be joining across the components. It may evolve towards a knotted field if not restricted to volume preserving deformations. The opposite happens in the Skyrme-Faddeev model, where $\mathcal{K}_{4,3} \rightarrow \mathcal{L}^{2,2,2}_{1,1,2}$. Other configurations have a much higher energy. They are:

$\mathcal{L}^{2,2}_{3,3}$:- Energy 6.421 with $V = 315000$,

$\mathcal{K}_{3,2}$:- Energy 6.527 with $V = 250000$,

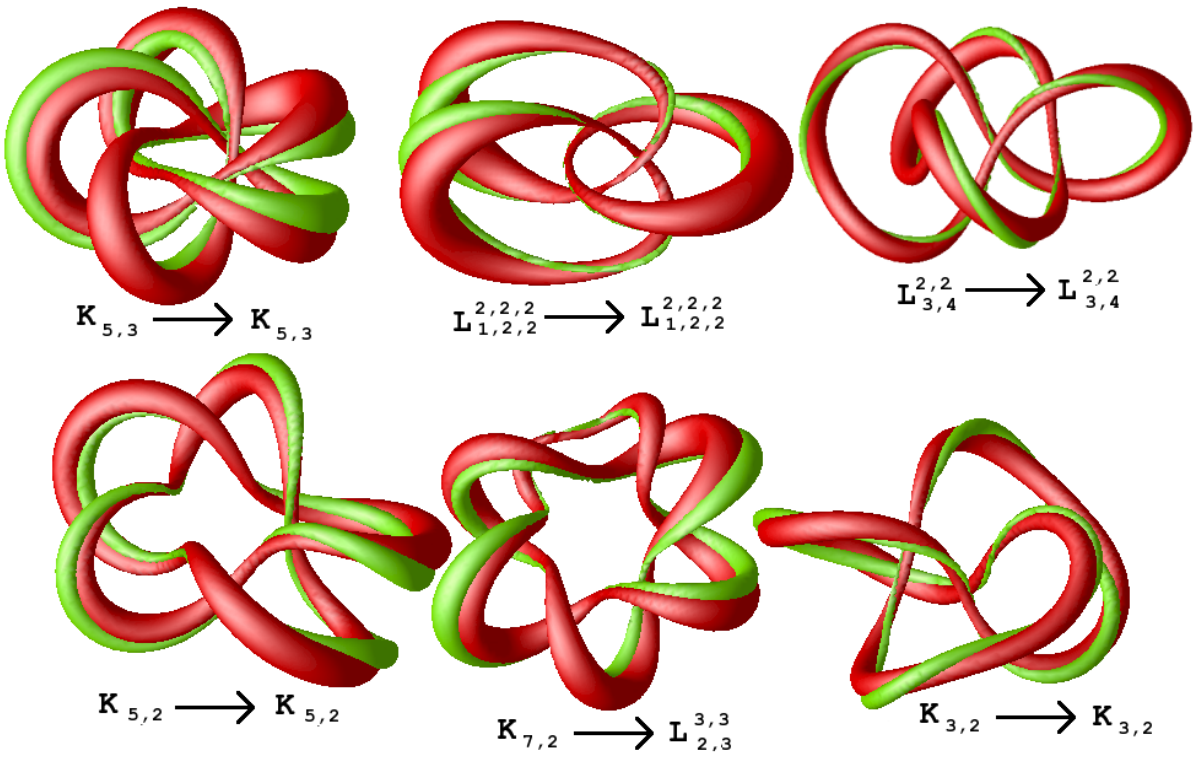

Figure 5.6: Hopf index $\mathcal{Q}=11$ static solutions in the Nicole model. Initial and final field configuration types are given below each soliton. Surfaces are same as in figure 5.1. Solitons at each Hopf index are ordered lowest static energy to the left and highest static energy to the right. Not all solutions are stable, some may be saddle points or local minima in the restricted flow landscape but not exist in the full energy landscape.

$\mathcal{L}^{1,1}_{4,4}$:- Energy 7.075 with $V=290000$,

$\mathcal{L}^{1,1}_{A_{2,2},A_{2,2}}$:- Energy 8.806 with $V=240000$.

The $\mathcal{L}^{1,1}_{4,4}$ and $\mathcal{L}^{1,1}_{A_{2,2},A_{2,2}}$ are unlikely to be static solutions of the Nicole model, it is likely that they have zero modes associated with volume preserving deformations which result in very slow evolution by volume preserving minimisation. The Skyrme-Faddeev model also has static $\mathcal{L}^{2,2}_{3,3}$ and $\mathcal{K}_{3,2}$ solutions, which can be found from several different initial configurations.

Hopf index 11 also has many static solutions under volume preserving minimisation. Again the Nicole model differs from the Skyrme-Faddeev model in that the minimal energy configuration is a knot once again. It is a $\mathcal{K}_{5,3}$ type knot, with an energy of 6.665 for $V=210000$ and it is also found by minimising a $\mathcal{K}_{7,4}$ type field configuration. This configuration required a much larger volume, where the energy reduced to 6.772 for $V=700000$. An $\mathcal{L}^{2,2,2}_{1,2,2}$ configuration is found, with an energy of 6.729 for $V=300000$. It can be seen in figure 5.6. The two $\mathcal{Q}=2$ components seem to be attempting to link

together suggesting that this evolution may be a zero mode resulting from the restriction to volume preserving flow. A $\mathcal{K}_{4,3}$ type configuration is not stable under volume preserving minimisation. Two further knot solutions are found, along with two double component links:

$\mathcal{L}^{2,2}_{3,4}$:- Energy 6.943 with $V = 205000$,

$\mathcal{K}_{5,2}$:- Energy 7.054 with $V = 280000$,

$\mathcal{L}^{3,3}_{2,3}$:- Energy 7.131 with $V = 285000$,

$\mathcal{K}_{3,2}$:- Energy 7.179 with $V = 340000$.

The $\mathcal{K}_{5,2}$ appears to have a zero mode associated with two of the string sections moving together to reconnect and so it not likely to be a static solution in the Nicole model. The $\mathcal{K}_{3,2}$ configuration has a similar zero mode relating to reconnection and so is not likely to be a static solution of the Nicole model.

5.3.1 Restrictions of Volume Preserving Flow

It has already been found that this volume preserving minimisation technique can restrict the flow through configuration space to the extent that stationary points of the energy functional occur that are not local minima in the full configuration landscape. This was covered in detail in chapter 3 and may also occur here. For some initial configurations of a given type, the field flows to a static solution with the same knot topology. For other initial configurations of the same type, the flow alters the knot topology to that of a different type - usually to the knot topology of the global minimum of the energy functional. This requires a little more rigour in the numerical investigation of the Nicole model for a given Hopf index using volume preserving flow than if there were fewer local minima. It becomes important to begin with as many different initial conditions as possible to ensure all static configurations are found. It is also necessary to use perturbed initial conditions and, where possible, different initial conditions with the same knot topology (such as taking different α, β in (4.2.6)). These restrictions are certainly less of an issue than in [2] as these stationary points of the energy, with respect to volume preserving deformations, only seem to relate the re-linking of the knot and link strings.

5.4 Conclusion

Volume preserving flow has been used to find stable, minimal energy solitons in the Nicole model for Hopf index one to eleven. The results presented here were compared to results obtained by Sutcliffe for $\mathcal{Q} = 1 \ldots 8$ and then energys matched to well within the errors of the calculation. Solutions for $\mathcal{Q} = 9 \ldots 11$ were also found in addition to the results of Sutcliffe. The solutions are similar to those found in the Skyrme-Faddeev model as they include both knotted and linked solutions. In some cases, the form of the minimal energy solution for a given $\mathcal{Q}$ are similar and in some cases they are different. It has also been shown that the previously calculated solutions with axial symmetry are unstable past Hopf index two. This indicates that knotted and linked solutions may be universal features of Hopf solitons. These results indicate that for small charges, the solitons are qualitatively similar in the Nicole and Skyrme-Faddeev model. They also show that for higher charges, this is generally not the case. There does not appear to be a general rule to indicate whether a Hopf index soliton will be of the same type in both models or not. For larger $\mathcal{Q}$, mnore static solutiosn were found. I believe that all the global energy minima have been found in this range of $\mathcal{Q}$. Im am not convinced that the $\mathcal{Q} = 5\mathcal{K}_{3,2}$ solution is a local minimum of the full energy function, but a stationary point (or shallow energy gradient) of the restricted energy function. The same could be said of some of the other solutions for $\mathcal{Q} > 8$, which have an energy significantly larger than that of the global minimum. In most cases, the three lowest energy configurations are likely to be true minima and the only configurations I would discount as being true minima are the $\mathcal{Q} = 10\mathcal{L}^{1,1}_{4,4}$ and the $\mathcal{Q} = 10\mathcal{L}^{1,1}_{A_{2,2},A_{2,2}}$. Further investigation is required to establish some of the other solutions as true minima or purely stationary points of the restricted energy function.

The Skyrme-Faddeev model has a conjectured lower bound on the energy, introduced in the previous chapter. The proof in the Skyrme-Faddeev model [51] of this lower bound cannot be easily adapted for the Nicole model [59]. The largest possible conjectured lower bound in the units given here is

$$E_{Ni} \geq \mathcal{Q}^{\frac{3}{4}}, \tag{5.4.1}$$

where the solitons with $\mathcal{Q} > 2$ have energies $\sim 10-12\%$ above this bound. This fits in

with the explicit solution for $\mathcal{Q} = 1$ and these results, seen in figure 5.2, clearly fit well with this bound. This suggests the results found are good candidates to be the global minima for the Hopf charges investigated. Any future proof of this bound would also indicate a universal feature of Hopf solitons and the numerical results here support that.

Future work could include an investigation of larger Hopf index solutions and how they relate to Hopf solitons in other models. A possible proof of the energy bound would also be useful. Other models with Hopf solitons will be discussed in the chapters to follow.

Chapter 6

Solitons in the AFZ Model

6.1 Introduction

The previous two chapters have discussed Hopf solitons in two different models, the Skyrme-Faddeev model and the Nicole model. The Skyrme-Faddeev model has a Lagrangian density containing two parts, a sigma-type term and a Skyrme-type term. In three spatial dimensions neither term on its own will allow for the possibility of solitons, but the combination of the terms does, by Derrick's theorem [6]. Topological solitons may be allowed, by taking either term to a specific fractional power. The Nicole model [8], which takes the first term to a fractional power, was discussed in the previous chapter. Taking the Skyrme-term to the power three quarters is referred to as the AFZ model [9, 10], after Aratyn, Ferreira and Zimerman who found infinitely many analytic solutions using toroidal coordinates. The Lagrangian density is given by

$$\mathcal{L}_{AFZ} = \left(H_{\mu\nu}^2\right)^{\frac{3}{4}} , \quad \text{where} \quad H_{\mu\nu} = \boldsymbol{\phi} \cdot (\partial_\mu \boldsymbol{\phi} \times \partial_\nu \boldsymbol{\phi}) . \tag{6.1.1}$$

As the target space is an $\mathcal{S}^2$, $\boldsymbol{\phi} \cdot \boldsymbol{\phi} = 1$. Like the Nicole model, the AFZ model is a scale invariant field theory. The Hopf map $\boldsymbol{\phi} : \mathbb{R}^3 \to \mathcal{S}^2$ was introduced in chapter 4. Solitons are classified by an integer valued topological charge $\mathcal{Q}$, the Hopf index. This charge is topological, meaning that maps of different charges cannot be continuously deformed into each other. The static energy of the AFZ model is given by

$$E_{AFZ} = \frac{1}{16\pi^2 2^{\frac{3}{4}}} \int \left(H_{ij}^2\right)^{\frac{3}{4}} d^3x , \quad H_{ij} = \boldsymbol{\phi} \cdot (\partial_i \boldsymbol{\phi} \times \partial_j \boldsymbol{\phi}) . \tag{6.1.2}$$

The normalisation gives the charge $\mathcal{Q}=1$ soliton an energy $E_{AFZ}=1$. Finite energy does not require the field to tend to a constant value at infinity, but our compactification of $\mathbb{R}^3$ does. This can be arbitrarily chosen without a loss of generality and, as before, it will be taken to be $\boldsymbol{\phi}=(0,0,1)$. The position of the soliton will be taken to be where the field is antipodal to this value, i.e. $\boldsymbol{\phi}=(0,0,-1)$.

6.2 Exact Solutions

It is possible to find an infinite number of soliton solutions to the AFZ model by exploiting its symmetries [10]. The static equations of motion for the AFZ model can be re-expressed in terms of toroidal coordinates, (η,ξ,φ):

$$x=\frac{a\sinh(\eta)\cos(\varphi)}{\cosh(\eta)-\cos(\xi)}\,,\quad y=\frac{a\sinh(\eta)\sin(\varphi)}{\cosh(\eta)-\cos(\xi)}\,,\quad z=\frac{a\sin(\xi)}{\cosh(\eta)-\cos(\xi)}. \tag{6.2.1}$$

Here, a is the radius of the torus ring. The ranges for the toroidal coordinates are $\eta\in[-\infty,+\infty]$, $\xi\in\left(-\frac{\pi}{2},+\frac{\pi}{2}\right]$, $\varphi\in[0,2\pi)$. Finding (η,ξ,φ) from (x,y,z) is a little more tricky. These coordinates can be derived by the rotation of a bipolar coordinate system, (η,ξ), figure 6.1. The rotation is of two foci $\mathcal{F}_1,\mathcal{F}_2$ about their perpendicular bisector giving the angle φ. In bipolar coordinates, any points in the plane are d_1 and d_2 away from $\mathcal{F}_1$ and $\mathcal{F}_2$. η is the natural log of the ratio of these two distances. ξ is the angle that a point makes when connected to the two foci. Curves of constant η are a set of non-intersecting, non-concentric circles, surrounding a focus, with the circle's centre lying on the x'-axis (blue curves in figure 6.1-right). Curves on the $x'>0$ half-plane have positive η while negative η gives curves on the $x'<0$ half-plane, with $\eta=0$ giving the y'-axis. Curves of constant ξ also from non-concentric circles, all passing through the two foci with centres lying along the y'-axis (red curves figure 6.1-right). Circles centred on the $y'>0$ half-axis have positive ξ while negative ξ gives curves on the $y<0$ half-axis, with $\xi=0$ being a circle of radius a centred at $(x',y')=(0,0)$. As $|\xi|$ increases, curves of constant ξ will be circles with ever increasing radii, with the maximal $|\xi|=\frac{\pi}{2}$ circle having infinite radius, i.e. the x'-axis. The circles of constant η,ξ meet orthogonally at two points and so are Apollonian circles. Note that the x' and y'-axes do not describe the x and y of the three dimensional system. In fact, the y'-axis becomes the z-axis and

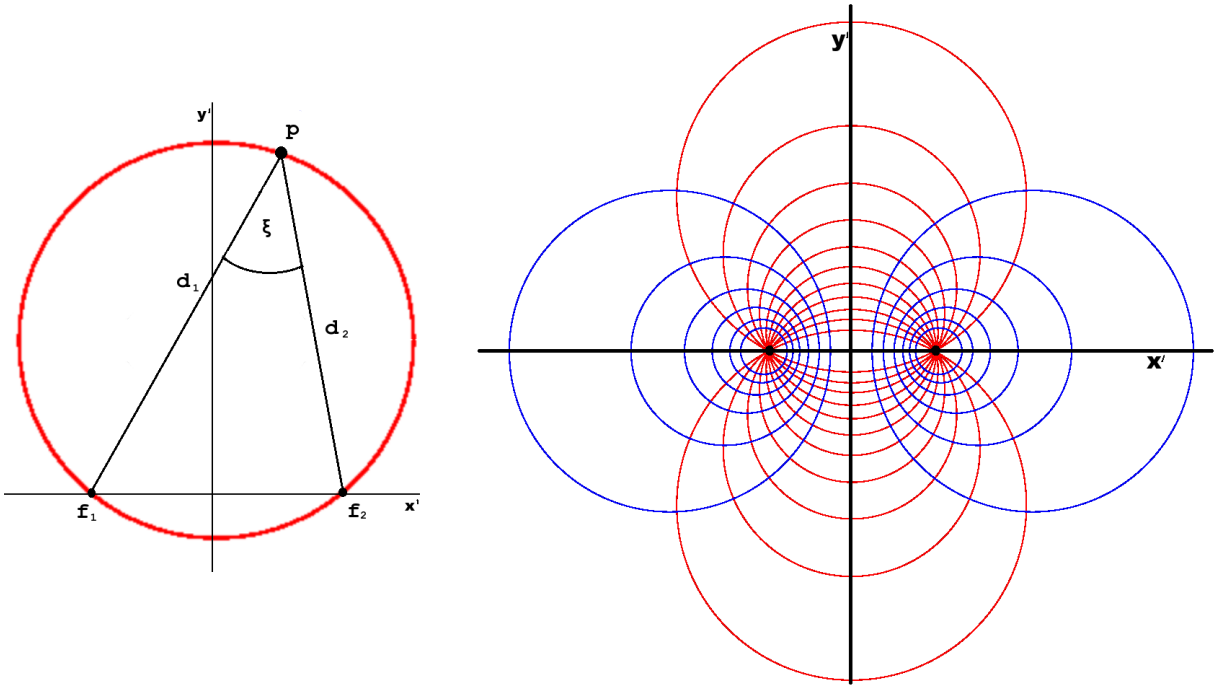

Figure 6.1: Bipolar Coordinates. (left) The red circle is a curve of constant ξ, a point is connected to the two foci, $\mathcal{F}_1$ and $\mathcal{F}_2$. The natural logarithm of these two distances gives the η coordinate and the angle between them gives ξ. (right) The Apollonian circles, which characterises the constant coordinate curves here. The red circles are curves of constant ξ while the blue circles are curves of constant η.

the x and y-axes are the x'-axis when $\varphi = 0$ and $\frac{\pi}{2}$ respectively.

In terms x, y, z, toroidal coordinates are;

$$\eta = \ln\left(\frac{d_1}{d_2}\right), \quad \cos(\xi) = \frac{d_1^2 + d_2^2 - 4a^2}{2d_1 d_2} \quad \text{and} \quad \tan(\varphi) = \frac{x}{y}; \tag{6.2.2}$$

where d_1 and d_2 are the two distances to the foci, see figure 6.1-left

$$\begin{aligned} d_1^2 &= \left(\sqrt{x^2+y^2}+a\right)^2 + z^2 \\ d_2^2 &= \left(\sqrt{x^2+y^2}-a\right)^2 + z^2. \end{aligned} \tag{6.2.3}$$

The sign of the angle ξ is determined by the sign of z.

An ansatz for an axially symmetric soliton in these coordinates is be [10];

$$W = f(\eta) e^{in\xi - im\varphi}, \tag{6.2.4}$$

where W is the Riemann sphere coordinate on the the target $\mathcal{S}^2$ of $\boldsymbol{\phi}$, (4.1.2). Taking m and n to be integers makes W single valued. These integers turn out to be the winding numbers for lines of constant ϕ_1, ϕ_2 about the surfaces of constant ϕ_3, which are themselves tori. m defines the φ winding, about the ring of the torus and n defines the

ξ winding, which is effectively around the cross section of the torus, i.e. about the focal ring.

The resulting energy minimising profile functions can then be found analytically [10] for infinitely many soliton solutions with a given set of boundary conditions. This integrability is due to an infinite number of conserved charges on top of the manifest scale invariance for the model. The static equations of motion in toroidal coordinates using this ansatz become ordinary differential equations that can simply be integrated. This results in a profile function which only depends on η and the ratio of the windings, for $m^2/n^2 > 1$.

$$f^2 = \frac{\cosh\eta - \sqrt{\frac{n^2}{m^2} + \sinh^2\eta}}{\sqrt{1 + \frac{m^2}{n^2}\sinh^2\eta} - \cosh\eta}. \tag{6.2.5}$$

The boundary conditions here are that $\boldsymbol{\phi} \to (0,0,1)$ at spatial infinity and $\boldsymbol{\phi} \to (0,0,-1)$ at the centre of the torus, i.e. where $\eta{=}0$. This is equivalent to $|W| \to 0$ as $\eta \to 0$ and $|W| \to \infty$ as $\eta \to \infty$. Then as $m \to n$,

$$\lim_{m\to n} f^2 = \sinh^2\eta. \tag{6.2.6}$$

The resultant energy for a given axial soliton in this model is given by;

$$E_{AFZ} = 2^{-\frac{1}{2}}\sqrt{|n||m|\,(|n| + |m|)}. \tag{6.2.7}$$

Here, m and n are the winding numbers about the two $\mathcal{S}^1$'s of the torus. This can be re-expressed using a ratio of these winding numbers to show that the energy of an axial soliton is minimised when the two winding numbers are as close as possible to one another.

$$E_{AFZ} = 2^{-\frac{1}{2}}\mathcal{Q}^{\frac{3}{4}}\sqrt{\vartheta + \frac{1}{\vartheta}}\,, \qquad \vartheta^2 = \left|\frac{m}{n}\right|. \tag{6.2.8}$$

This property suggests that $\vartheta = 1$ solitons which have equal winding numbers are candidates for the lowest energy solutions for those given charges, although this has not been quantified to date. It can also be shown [10] that ϕ_3 rises monotonically from -1 at $\eta{=}0$ to 1 at $\eta{=}\infty$ and the Hopf charge $\mathcal{Q}{=}nm$ for solutions of this type. Modified AFZ models have also been investigated [62] where the $O(3)$ symmetry is explicitly broken.

Axial AFZ Energy					
Q	**Type**	**E/E$_1$**	**Q**	**Type**	**E/E$_1$**
1	$A_{1,1}$	1.000	8	$A_{8,1}$	6.000
2	$A_{2,1}$	1.732	9	$A_{3,3}$	5.196
3	$A_{3,1}$	2.449	9	$A_{9,1}$	6.708
4	$A_{2,2}$	2.828	10	$A_{5,2}$	5.916
4	$A_{4,1}$	3.162	11	$A_{11,1}$	8.124
5	$A_{5,1}$	3.873	12	$A_{4,3}$	6.481
6	$A_{3,2}$	3.873	13	$A_{13,1}$	9.539
6	$A_{6,1}$	4.583	14	$A_{7,2}$	7.937
7	$A_{7,1}$	5.292	15	$A_{5,3}$	7.746
8	$A_{4,2}$	4.899	16	$A_{4,4}$	8.000

Computed Hopf soliton AFZ energy					
Q	**Type**	**E/E$_1$**	**Q**	**Type**	**E/E$_1$**
1	$A_{1,1}$	0.998	8	$L^{2,2}_{2,2}$	5.201
2	$A_{2,1}$	1.776	8	$K_{3,2}$	5.299
3	$\tilde{A}_{3,1}$	2.487	8	$L^{1,1}_{3,3}$	5.485
3	$A_{3,1}$	2.583	9	$L^{2,2,2}_{1,1,1}$	5.596
4	$L^{1,1}_{1,1}$	3.099	9	$K_{5,2}$	5.752
5	$L^{1,1}_{1,2}$	3.645	9	$K_{3,2}$	5.853
5	$K_{3,2}$	3.676	10	$K_{4,3}$	6.073
6	$L^{1,1}_{2,2}$	4.192	10	$L^{2,2,2}_{1,1,2}$	6.091
7	$K_{3,2}$	4.738	11	$K_{5,3}$	6.536
7	$L^{1,1}_{2,3}$	4.813	11	$L^{2,2,2}_{1,2,2}$	6.568

Table 6.1: (left) List of AFZ axial soliton energies, calculated using (6.2.7) and (right) are the AFZ energies of static solutions to the Nicole model.

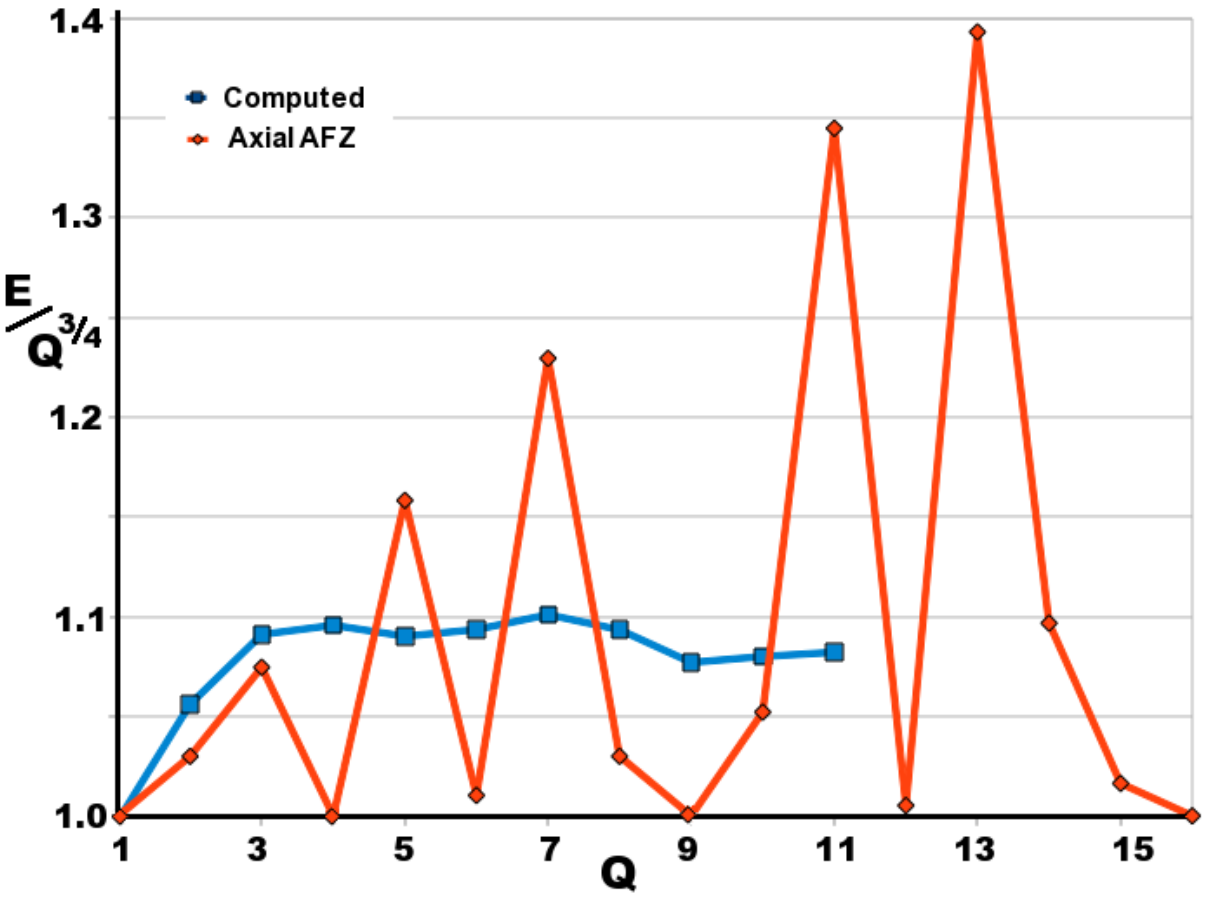

Figure 6.2: Energy/$\mathcal{Q}^{\frac{3}{4}}$ vs. charge for the computed soliton energies and the calculated axial solitons. (red) Axial energies calculated using (6.2.7). (blue) AFZ energies of the Nicole solitons. These are purely Hopf soliton field configurations of the correct Hopf index and their energy is evaluated but note they are not solutions to the AFZ model.

These models are also integrable in that an infinite number of conserved charges can be constructed. Once again they are axial solutions and the energy follows a $\mathcal{Q}^{3/4}$ trajectory. In fact, the energy takes the same value as in the AFZ model [10].

The energy of the axial solutions follows a $\mathcal{Q}^{\frac{3}{4}}$ trajectory, and the square charged solitons with equal winding attain this bound. There is room for non-axial solutions for other charges though. For $\mathcal{Q}$ that are prime numbers, ϑ will become large and axial solitons will have energies that lie some way above the trajectory followed by the square charged axial solitons. The normalised energy for low charged axial solitons in the AFZ model can be found in table 6.1(left). Table 6.1(right) shows the AFZ energies of some static field configurations found in the Nicole model. No minimisation has been done here, the energy of the configurations has been simply evaluated. Figure 6.2 plots the energy/$\mathcal{Q}^{3/4}$ against Hopf index for the analytic solutions and the static solutions to the Nicole model. Clearly for Hopf charges 5, 7 and 11, the link and knot solutions to the Nicole model have a much lower energy than the axial solutions. In these cases at least, a non-axial solution must be the minimal energy configuration. Details of these solutions for Hopf index 1 to 8 will be presented later.

6.3 Volume Preserving Flow

For the AFZ model, the local energy density $\mathcal{E}$ in three spatial dimensions can be given in the form (employing a Lagrange multiplier as before)

$$\mathcal{E} = \left(H_{ij}^2\right)^{\frac{3}{4}} + \lambda\left(1 - \boldsymbol{\phi}\cdot\boldsymbol{\phi}\right), \tag{6.3.1}$$

where

$$H_{ij} = \boldsymbol{\phi}\cdot\left(\partial_i\boldsymbol{\phi}\times\partial_j\boldsymbol{\phi}\right), \quad \text{denote} \quad H_{ij}^2 \equiv H. \tag{6.3.2}$$

The Lagrange multiplier, λ, is locally defined so that at every point the equations of motion are satisfied. To examine the variation, it is useful to rewrite H. It can be rewritten as any of the following;

$$\begin{aligned} H &= \left(\partial_i\boldsymbol{\phi}\times\partial_j\boldsymbol{\phi}\right)\cdot\left(\partial_i\boldsymbol{\phi}\times\partial_j\boldsymbol{\phi}\right), \\ &= \left[\left(\partial_k\boldsymbol{\phi}\cdot\partial_k\boldsymbol{\phi}\right)^2 - \left(\partial_i\boldsymbol{\phi}\cdot\partial_j\boldsymbol{\phi}\right)\left(\partial_i\boldsymbol{\phi}\cdot\partial_j\boldsymbol{\phi}\right)\right] \end{aligned} \tag{6.3.3}$$

Variation of the energy density leads to the static equations of motion for the AFZ model,

$$H^{-\frac{5}{4}}\left[\left(\partial_i\partial_j\boldsymbol{\phi}\cdot\partial_j\boldsymbol{\phi}\right)\Lambda-\left(\partial_i\partial_j\boldsymbol{\phi}\cdot\partial_k\boldsymbol{\phi}\right)\left(\partial_j\boldsymbol{\phi}\cdot\partial_k\boldsymbol{\phi}\right)\right]\left[\partial_l\boldsymbol{\phi}\left(\partial_i\boldsymbol{\phi}\cdot\partial_l\boldsymbol{\phi}\right)-\partial_i\boldsymbol{\phi}\Lambda\right] \tag{6.3.4}$$
$$+H^{-\frac{1}{4}}\left[\nabla^2\boldsymbol{\phi}\Lambda+\partial_i\boldsymbol{\phi}\left(\partial_i\partial_j\boldsymbol{\phi}\cdot\partial_j\boldsymbol{\phi}\right)-\partial_i\partial_j\boldsymbol{\phi}\left(\partial_i\boldsymbol{\phi}\cdot\partial_j\boldsymbol{\phi}\right)-\partial_j\boldsymbol{\phi}\left(\nabla^2\boldsymbol{\phi}\cdot\partial_j\boldsymbol{\phi}\right)\right]+\lambda\boldsymbol{\phi}=\mathbf{0},$$

where $\Lambda=\left(\partial_i\boldsymbol{\phi}\cdot\partial_i\boldsymbol{\phi}\right)$ and $\nabla^2\boldsymbol{\phi}=\partial_i\partial_i\boldsymbol{\phi}$. λ is defined by (6.3.4), using $\boldsymbol{\phi}\cdot\boldsymbol{\phi}=1$.

The gradient flow equations (2.1.19) for this model are

$$\frac{\partial\boldsymbol{\phi}}{\partial t} = -\frac{\delta\mathcal{E}}{\delta\boldsymbol{\phi}} \equiv \boldsymbol{F} = \boldsymbol{F}_{AFZ}+\lambda\boldsymbol{\phi}: \tag{6.3.5}$$
$$\begin{aligned}\boldsymbol{F}_{AFZ} &= H^{-\frac{1}{4}}\left[\nabla^2\boldsymbol{\phi}\Lambda+\partial_i\boldsymbol{\phi}\left(\partial_i\partial_j\boldsymbol{\phi}\cdot\partial_j\boldsymbol{\phi}\right)-\partial_i\partial_j\boldsymbol{\phi}\left(\partial_i\boldsymbol{\phi}\cdot\partial_j\boldsymbol{\phi}\right)-\partial_j\boldsymbol{\phi}\left(\nabla^2\boldsymbol{\phi}\cdot\partial_j\boldsymbol{\phi}\right)\right]\\ &+ H^{-\frac{5}{4}}\left[\left(\partial_i\partial_j\boldsymbol{\phi}\cdot\partial_j\boldsymbol{\phi}\right)\Lambda-\left(\partial_i\partial_j\boldsymbol{\phi}\cdot\partial_k\boldsymbol{\phi}\right)\left(\partial_j\boldsymbol{\phi}\cdot\partial_k\boldsymbol{\phi}\right)\right]\left[\partial_l\boldsymbol{\phi}\left(\partial_i\boldsymbol{\phi}\cdot\partial_l\boldsymbol{\phi}\right)-\partial_i\boldsymbol{\phi}\Lambda\right],\end{aligned}$$

and $\boldsymbol{\phi}\cdot\boldsymbol{F}=0$ is needed to keep the flow on the unit sphere, so $\lambda=-\boldsymbol{\phi}\cdot\boldsymbol{F}_{AFZ}$, i.e.

$$\lambda=-H^{-\frac{1}{4}}\boldsymbol{\phi}\cdot\left[\nabla^2\boldsymbol{\phi}\Lambda-\partial_i\partial_j\boldsymbol{\phi}\left(\partial_i\boldsymbol{\phi}\cdot\partial_j\boldsymbol{\phi}\right)\right]. \tag{6.3.6}$$

Volume preserving gradient flow (2.1.38) can be used to constrain the flow to a direction which will leave a given total integral of a given function, v, unchanged.

$$\frac{\partial\boldsymbol{\phi}}{\partial t}=\boldsymbol{F}-\frac{\langle\boldsymbol{f}\cdot\boldsymbol{F}\rangle}{\langle\boldsymbol{f}\cdot\boldsymbol{f}\rangle}\boldsymbol{f}, \quad \text{with} \quad \boldsymbol{f}=-\frac{\delta v}{\delta\boldsymbol{\phi}}, \quad \text{and} \quad v=\frac{1}{2}\left(1-\phi_3\right). \tag{6.3.7}$$

This particular flow will preserve, in general, the size of the soliton. Since the soliton position is defined to be where $\phi_3=-1$ and $\phi_3\to 1$ at spatial infinity, this choice of volume counting seems reasonable.

Note here, it is important not to scale out the H's to make the solution more manageable. As H gets very small and is spatially dependent, scaling it out can result in very little movement in the flow, as anywhere that H is small is effectively not moved.

6.3.1 Problems with Solutions of the AFZ Model

Several features of this model make it difficult to investigate numerically. Firstly, the model is scale invariant. For static solutions, this problem can be overcome using volume preserving gradient flow as has been set out previously.

In addition to the conformal symmetry that leads to a simplified form of the equations of motion in toroidal coordinates there are also infinitely many hidden symmetries. In

fact, the AFZ model shows infinitely many target space symmetries. There are area preserving diffeomorphisms of the target space in the AFZ model [63, 64]. A symmetry transformation which maps solutions to solutions exists. It connects any solution with the trivial one, so naively one might think any field configuration can then unwind to the trivial solution. The unwinding would result in sectors of different Hopf charges that are not separated by an infinite energy barrier. Since static solitons have already been found, this problem can be overcome [60]. In fact, these intermediate configurations are only weak solutions and are described by fields that are not fully continuous. This unwinding can be stopped by fixing a boundary value for the field, although finite energy considerations do not require that the field tends to a constant. The ability of this value to change on the boundary as a result of the target space symmetries leads to the unwinding.

The scaling symmetry of the base space and the area preserving diffeomorphisms of the target space can be combined to find a symmetry of the action, resulting in a conserved current which has a divergence associated [63]. This divergence has been found to occur in an infinite line [63] and can also be ring-like [65]. This could restrict to only $\mathcal{C}^1$ differentiability. The energy as it is only dependent on gradient products, but equations of motion contain second derivative terms which may diverge. The Nicole model does not have these symmetries [66], and therefore does not display the same integrability as the AFZ model. There is also some room for discussion on the stability of possible solutions for the AFZ model which is still to be resolved.

6.3.2 Overcoming the Problems

As was mentioned earlier, any investigation into solutions to the AFZ model is fraught with difficulties. The many symmetries present in the model which make it easier to address questions from an analytical point of view cause great problems when probing the model numerically. Firstly the conformal invariance will inherently be broken under discretisation. In this case, most attempts to minimise energy will cause any solution to shrink, until it falls through the lattice. Volume preserving gradient flow will help to avoid complications here.

The major hurdle comes from a lack of smoothness. Although the fields themselves

are continuous, discontinuities in the derivatives can lead to problems with further differentiation. The equations of motion (which contain second derivative terms) may not always be well defined. Some limitation of derivatives may overcome, or at least subdue such an issue. Breaking the symmetries that cause this problem would be a better approach. The Nicole model and AFZ model share a large group of symmetries but not the problematic ones set out above. Introducing a small amount of the Nicole model to our energy minimisation could overcome this issue. As long as this amount is small it should not greatly alter the form of any solutions.

It can easily be seen from (6.2.5) that the tails of the axial solitons will be very long. To be able to reasonably compute solutions, these tails will need to be truncated, by putting the theory into a box. This will introduce an error of the order of a few % so if the amount of Nicole model added is in the region of this error, it should not cause an issue. When referring directly to the AFZ model, any energies quoted will be the pure AFZ energy and the extra symmetry breaking term will only contribute to the flow. Any solutions found will be static in the broken symmetry model. These should be good approximations of the static solutions of the AFZ model as long the symmetry breaking contribution remains small.

6.3.3 Energy minimisation with Symmetry Breaking

The minimisation procedure remains closely related to that stated earlier on. There will be a new flow energy, which will be the energy associated with the gradient flow;

$$\mathcal{E}' = H^{\frac{3}{4}} + \epsilon\Lambda^{\frac{3}{2}} + \lambda'\left(1 - \boldsymbol{\phi}\cdot\boldsymbol{\phi}\right), \tag{6.3.8}$$

where H, Λ have previously been defined, λ' will be the new Lagrange multiplier and ϵ is a constant that weights the impact of the Nicole model on the gradient flow. Since energies in the Nicole model and AFZ model are of the same order, $\epsilon = 0.01$ would add $\sim 1\%$ of Nicole model to the overall flow direction. The new direction of flow $\boldsymbol{F}'$ will be given by $\boldsymbol{F}' = \boldsymbol{F}_{AFZ} + \epsilon\boldsymbol{F}_{Ni} + \lambda'\boldsymbol{\phi}$, where the gradient flow of the AFZ model, $\boldsymbol{F}_{AFZ}$, is the same as (6.3.6) and the gradient flow of the Nicole model, $\boldsymbol{F}_{Ni}$, is

$$\boldsymbol{F}_{Ni} = \nabla^2\boldsymbol{\phi}\Lambda^{\frac{1}{2}} + \partial_i\boldsymbol{\phi}\left(\partial_i\partial_j\boldsymbol{\phi}\cdot\partial_j\boldsymbol{\phi}\right)\Lambda^{-\frac{1}{2}}, \tag{6.3.9}$$

and again λ' is required to keep the fields on the unit sphere, i.e. $\boldsymbol{\phi}\cdot\boldsymbol{F}'=0$. Finally, the volume preserving flow is like before (6.3.7),

$$\frac{\partial\boldsymbol{\phi}}{\partial t'}=\boldsymbol{F}'-\frac{\langle\boldsymbol{f}\cdot\boldsymbol{F}'\rangle}{\langle\boldsymbol{f}\cdot\boldsymbol{f}\rangle}\boldsymbol{f},\quad\text{with}\quad\boldsymbol{f}=-\frac{\delta v}{\delta\boldsymbol{\phi}},\quad\text{and}\quad v=\frac{1}{2}\left(1-\boldsymbol{\phi}\cdot\boldsymbol{e}_3\right). \tag{6.3.10}$$

Volume preserving flow will be applied to configurations of Hopf index $\mathcal{Q}=1\,..\,8$ using the rational maps detailed in chapter 4. These configurations will exist in a finite region Ω, and the field will be fixed at $\boldsymbol{\phi}=(0,0,1)$ on $\partial\Omega$. For the purpose of numerical investigation, Ω will be a cubic lattice with unit spacing of length 150. Derivatives will be approximated to fourth order accuracy using a finite difference method and the fields evolved using an explicit method with timestep $\Delta t\leq 0.1$. The AFZ energy and volume for configurations will be

$$E_{AFZ}=\frac{1}{16\pi^2 2^{\frac{3}{4}}}\int_\Omega\mathcal{E}\,d^3x\,,\qquad V=\int_\Omega v\,d^3x. \tag{6.3.11}$$

The energy $\mathcal{E}$ is that of the pure AFZ model, not including contributions from the symmetry breaking term. These integrals and inner products will be evaluated as summations over the lattice. The timestep will be reduced, where appropriate, to allow for continued evolution for a given ϵ which may be necessary if symmetry issues of the AFZ model become problematic. This reduction will be done to keep ϵ as small as possible. Calculations will be done with $\epsilon=0.01, 0.02$ in general, but $\epsilon\lesssim 0.05$ may be used for small periods of evolution to circumvent symmetry issues which cannot be overcome efficiently by lowering the timestep. In all cases except for the charge 1 soliton, $\epsilon>0$ is needed, although minimising a charge 1 with $\epsilon>0$ reaches almost the same static solution as without.

6.4 Solitons in the AFZ model

The previously defined rational maps create field configurations which have a given Hopf index. By minimising the energy of different rational maps, potential local and global energy minima may be found for a variety of Hopf charges in the AFZ model. This section will classify those results, as well as noting transitions between different types of configuration.

AFZ Energy									
Axial Solutions					**Numerical Results**				
$\mathcal{Q}$	**Type**	E	$E/\mathcal{Q}^{\frac{3}{4}}$		$\mathcal{Q}$	**Type**	ϵ	E	$E/\mathcal{Q}^{\frac{3}{4}}$
1	$A_{1,1}$	1.000	1.000		1	$A_{1,1}$	0.01	1.003	1.003
2	$A_{2,1}$	1.732	1.030		2	$A_{2,1}$	0.01	1.738	1.033
3	$A_{3,1}$	2.449	1.075		3	$\tilde{A}_{3,1}$	0.01	2.414	1.059
4	$A_{2,2}$	2.828	1.000		4	$A_{2,2}$	0.01	2.852	1.008
4	$A_{4,1}$	3.162	1.118		5	$K_{3,2}$	0.01	3.391	1.014
5	$A_{5,1}$	3.873	1.158		5	$L^{1,1}_{1,2}$	0.01	3.451	1.032
6	$A_{3,2}$	3.873	1.010		6	$A_{3,2}$	0.01	3.907	1.019
7	$A_{7,1}$	5.292	1.230		7	$K_{3,2}$	0.01	4.417	1.026
8	$A_{4,2}$	4.899	1.030		8	$A_{4,2}$	0.01	4.954	1.041

Table 6.2: (left) List of AFZ axial soliton energies, calculated using (6.2.7) and (right) are the energies of the static solutions found using the volume preserving gradient flow method. The amount of Nicole model used to find the solutions, ϵ is also given.

The soliton plots (figure 6.4) show a level set of $\phi_3 = -0.9$, giving an idea about the position of the soliton and a level set $\boldsymbol{\phi} = \left(\sqrt{\mu\,(2-\mu)}, 0, \mu - 1\right)$, with $\mu = 0.1$ which shows the linking. This is an arbitrary choice of a second pre-image curve, used to see the linking number, and so the Hopf index of a given configuration. Any preimage curves on the $\mathcal{S}^3$ can be chosen for this, including curves where $\phi_{1/2}$ are the only non-vanishing field quantities, but choosing a set of curves close to the position allows for the linking to be more easily counted.

The soliton energies for both the axial solutions and numerical results are given in table 6.2. These results are also shown in the graphs in figure 6.3. The minimal energy soliton positions and linking are shown in figure 6.4. All local minima as well as details on initial conditions and the resulting static configuration types are given in figure 6.5.

Hopf index one and two solitons are the same as in the Skyrme-Faddeev and Nicole models. They are the axial $\mathcal{A}_{1,1}$ and $\mathcal{A}_{2,1}$ configurations, see figure 6.4. The $\mathcal{A}_{1,1}$ axial soliton has an energy of 1.003 for a volume $V = 115000$. This matches well with the exact axial solution and is $< 0.5\%$ above the expected energy. The $\mathcal{A}_{2,1}$ axial soliton has an energy of 1.738 with $V = 100000$. This is also $< 0.5\%$ above the energy of the exact axial solution. Hopf index three solitons are also the same as in the Skyrme-Faddeev

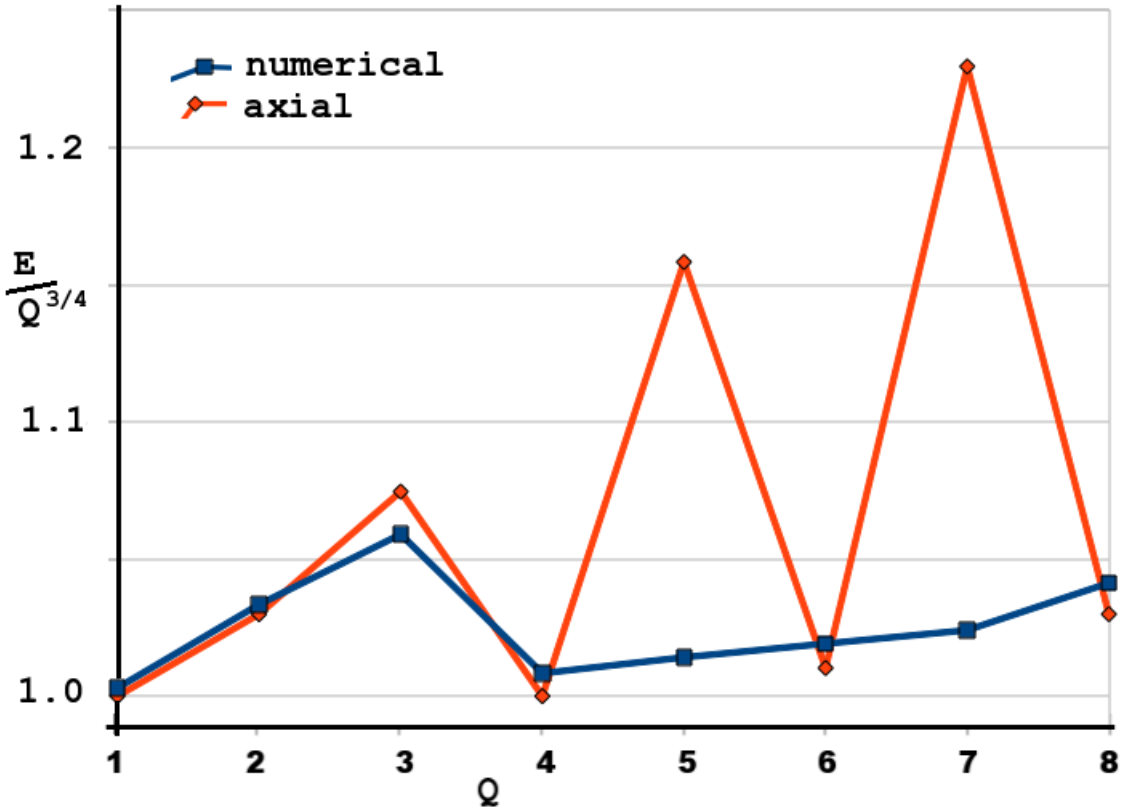

Figure 6.3: Plot of $E/\mathcal{Q}^{\frac{3}{4}}$ against charge from table 6.2 for both the axial solution (6.2.7) and the numerically calculated energies. E is normalised to be 1 for a charge one soliton.

and Nicole models, the $\tilde{\mathcal{A}}_{3,1}$ twisted axial configuration. It has an energy of 2.414 when $V=60000$. An axial $\mathcal{A}_{3,1}$ can be found as a saddle point of the minimisation if held by symmetry. An axial $\mathcal{A}_{3,1}$ configuration minimises to an energy of 1.476 with a volume $V=60000$. The axial solution held by symmetry is $\sim 1\%$ above the exact axial solution while the twisted $\tilde{\mathcal{A}}_{3,1}$ soliton is $\sim 1.5\%$ below the energy of the exact axial solution. Figure 6.3 shows that the $\mathcal{Q}=3$ soliton has an energy which is around 6% above the potential energy bound $E \geq \mathcal{Q}^{\frac{3}{4}}$. This energy is the furthest from the bound for any solitons found in this investigation.

The Hopf index four $\mathcal{A}_{2,2}$ exact axial solution attains the potential energy bound. The only stable solution with $\mathcal{Q}=4$ is in fact the axial $\mathcal{A}_{2,2}$, see figure 6.4. This is the same configuration found in the Skyrme-Faddeev model but not the Nicole model where the $\mathcal{Q}=4$ soliton is an $\mathcal{L}^{1,1}_{1,1}$ link. The $\mathcal{A}_{2,2}$ in the AFZ model has an energy of 2.852 for $V=130000$. This is $\lesssim 1\%$ above the expected energy, clearly not in as good an agreement as the $\mathcal{Q}=1,2$ solutions. Starting from an $\mathcal{L}^{1,1}_{1,1}$ type initial condition the field evolves towards an $\mathcal{A}_{2,2}$ type configuration but does not quite make it the whole way.

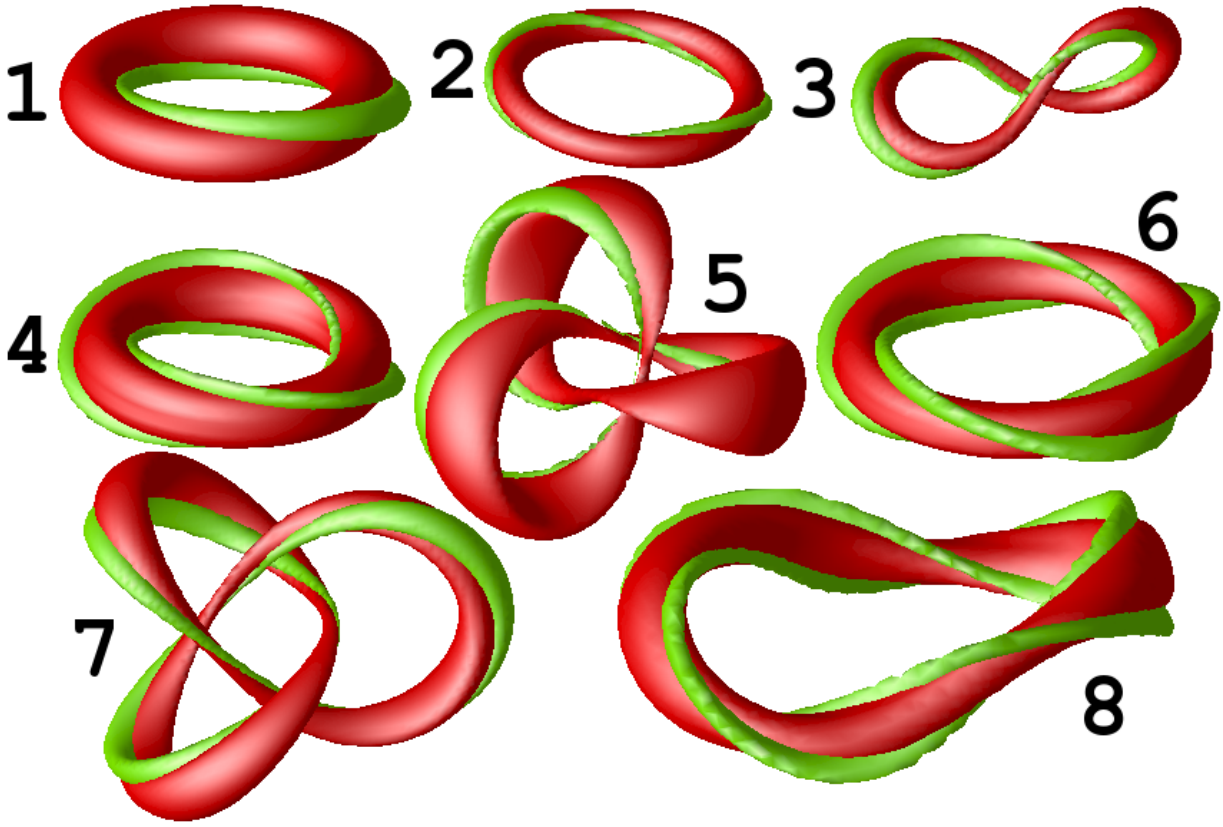

Figure 6.4: Hopf index $\mathcal{Q} = 1-8$ minimal energy soliton solutions in the AFZ model. The numbers indicate the Hopf index $\mathcal{Q}$.

The two strings do not seem to be able to unlink themselves and the result is a linked configuration but with the two unlinks lying almost on top of each other. This inability to make the full transition could be a result of the volume preserving minimisation as seen with the Nicole model in the previous chapter. It seems as though this type of configuration is a stationary point of the energy functional when restricted to volume preserving deformations. Some further details of these solutions are discussed in chapter 7. Axial $\mathcal{A}_{4,1}$ initial conditions tend to twist during minimisation. Imposing that the initial conditions are axially symmetric makes the twisting slow, with an axial $\mathcal{A}_{4,1}$ configuration having an energy of 3.196 for a volume $V = 60000$. The twisted $\tilde{\mathcal{A}}_{4,1}$ evolves similarly in the AFZ model as in the Nicole model, discussed previously. Unfortunately, solutions tend to pinch off near the points of greatest twist before any configuration transition occurs.

Hopf index five is the first which we might expect non-axial solutions to be minimal energy solutions based on figure 6.3. The axial $\mathcal{A}_{5,1}$ exact axial solution is $\sim 15\%$ above the $E \geq \mathcal{Q}^{\frac{3}{4}}$ conjectured energy bound. It has also been shown that evaluating the

AFZ energy of the minimal energy configurations in the Nicole model gives a much lower result than that of the exact axial solution. Volume preserving minimisation using the symmetry breaking term results in two local minima with energies much lower than the $\mathcal{A}_{5,1}$ axial solution, see figure 6.5. The lowest energy configuration is a $\mathcal{K}_{3,2}$ trefoil knot, with an energy of 3.339 for a volume $V=150000$. This is $\sim 1.5\%$ above the conjectured bound. The isosurface near to the soliton position forms a band-like structure rather than the usual string-like structure seen with trefoil knots in the Nicole or Skyrme-Faddeev model, (see figure 5.1 and [40]). The other static solution is an $\mathcal{L}^{1,1}_{1,2}$ link solution, like the minimal energy solutions in the Nicole and Skyrme-Faddeev models. It has an energy of 3.451 when $V=190000$, which is $\sim 2\%$ larger than the knotted solution. The trefoil knot appears to be the minimal energy soliton at $\mathcal{Q}=5$, but the small difference in energy and the fact that no configuration transitions are seen makes this proposition inconclusive. Axial $\mathcal{A}_{5,1}$ initial conditions tend to twist like with the $\mathcal{A}_{4,1}$ initial conditions. Axial solutions with a larger Hopf index, $\mathcal{Q}$, where the linking curve winds $\mathcal{Q}$ times around the position are more difficult to find than by simply imposing symmetry on the initial conditions. An approximately axial $\mathcal{A}_{5,1}$ configuration with a volume $V=225000$ has an energy of 3.924 which is $\sim 1.5\%$ above the expected value. This configuration is not stable. It tends to twist itself until a section of the string pinches off and the solution collapses. Conducting minimisation on a lattice with axial symmetry may result in an axial configuration with an energy much closer to the exact axial solution.

Hopf index six has a static solution that differs from the Nicole and Skyrme-Faddeev models. As the $\mathcal{A}_{3,2}$ exact axial solution has an energy that is only 1% above the conjectured bound it seems likely it will be the minimal energy solution. In fact it is, with an energy of 3.907 for a volume $V=160000$. This is $\lesssim 1\%$ above the energy of the exact axial solution, as was the axial $\mathcal{A}_{2,2}$ solution at Hopf index $\mathcal{Q}=4$. A range of initial conditions can be used, where the resultant minimisation leads to an $\mathcal{A}_{3,2}$ type configuration, or something near to an $\mathcal{A}_{3,2}$, as listed in figure 6.5. The same issue with configuration transition occurs at $\mathcal{Q}=6$ as did at $\mathcal{Q}=4$. An $\mathcal{L}^{1,1}_{1,3}$ configuration tends to pinch off at the point of the $\mathcal{Q}=3$ unlink that passes through the $\mathcal{Q}=1$ unlink before any configuration transition can occur. The $\mathcal{L}^{1,1}_{2,2}$, $\mathcal{L}^{2,2}_{1,1}$, $\mathcal{K}_{3,2}$ and $\mathcal{K}_{4,3}$ initial configurations all move towards an $\mathcal{A}_{3,2}$ type configuration, but the position strings seem unable to reconfigure

themselves into the correct formation. The result are knots or links where the strings all approximately in a plane, almost on top of each other.

Hopf index seven has only one solution and it is the same type as in the Nicole and Skyrme-Faddeev models, a trefoil knot. The $\mathcal{K}_{3,2}$ has an energy of 4.418 with $V=180000$ and is $\sim 17\%$ lower in energy than the exact axial solution. It is also $\sim 2.5\%$ above $\mathcal{Q}^{\frac{3}{4}}$. All possible starting configurations lead to a trefoil knot when $\mathcal{Q}=7$, as detailed in figure 6.5. Axial initial conditions twist once again under minimisation. In fact, they twist too quickly for the axial profile function to minimise and an axial energy to be found. All axial solutions are likely to be unstable for all prime $\mathcal{Q} > 7$, where the minimal energy configurations are likely to be knots and links, as in the Nicole and Skyrme-Faddeev models.

The final Hopf index investigated here is $\mathcal{Q}=8$. This time the axial $\mathcal{A}_{4,2}$ exact axial solution has an energy 3% above $\mathcal{Q}^{\frac{3}{4}}$. It is a likely candidate for the minimal energy solution but not a dead certainty. The minimal energy solution found by volume preserving minimisation from a range of initial conditions is a twisted $\mathcal{A}_{4,2}$ type configuration, denoted $\tilde{\mathcal{A}}_{4,2}$. It has an energy of 4.954 for $V = 130000$, around 4% above $\mathcal{Q}^{\frac{3}{4}}$. That makes it $\sim 1\%$ above the exact axial solutions energy. This would be in line with the energies found when $\mathcal{Q}=4,6$, except this solution is twisted. The configuration seems to be robust, since several types of initial conditions lead to an $\tilde{\mathcal{A}}_{4,2}$ type configuration, see figure 6.5 for details. As with the axial solutions for $\mathcal{Q}=4,6$, the minimisation of other knot and linked configurations results in configurations close to the $\tilde{\mathcal{A}}_{4,2}$ configuration, where the strings are not able to reconnect in the correct orientation under volume preserving minimisation with symmetry breaking. Imposing axial symmetry in the initial conditions can lead to an $\mathcal{A}_{4,2}$ axial configuration, which has an energy of 4.978 when $V=110000$. This is $\sim 1.5\%$ above the exact axial solutions energy. As the energy of the twisted $\tilde{\mathcal{A}}_{4,2}$ configuration is approximately what might be expected for the energy of an axial configuration under volume preserving minimisation it is not clear whether this is the $\mathcal{Q}=8$ soliton configuration in the AFZ model or not. The twisting may be an artefact of the Nicole symmetry breaking term in the modified minimisation. The twisting may minimise the Nicole component to such an extent that breaking the symmetry kills the axial solution. Investigation using a much larger domain Ω may help shed light on this.

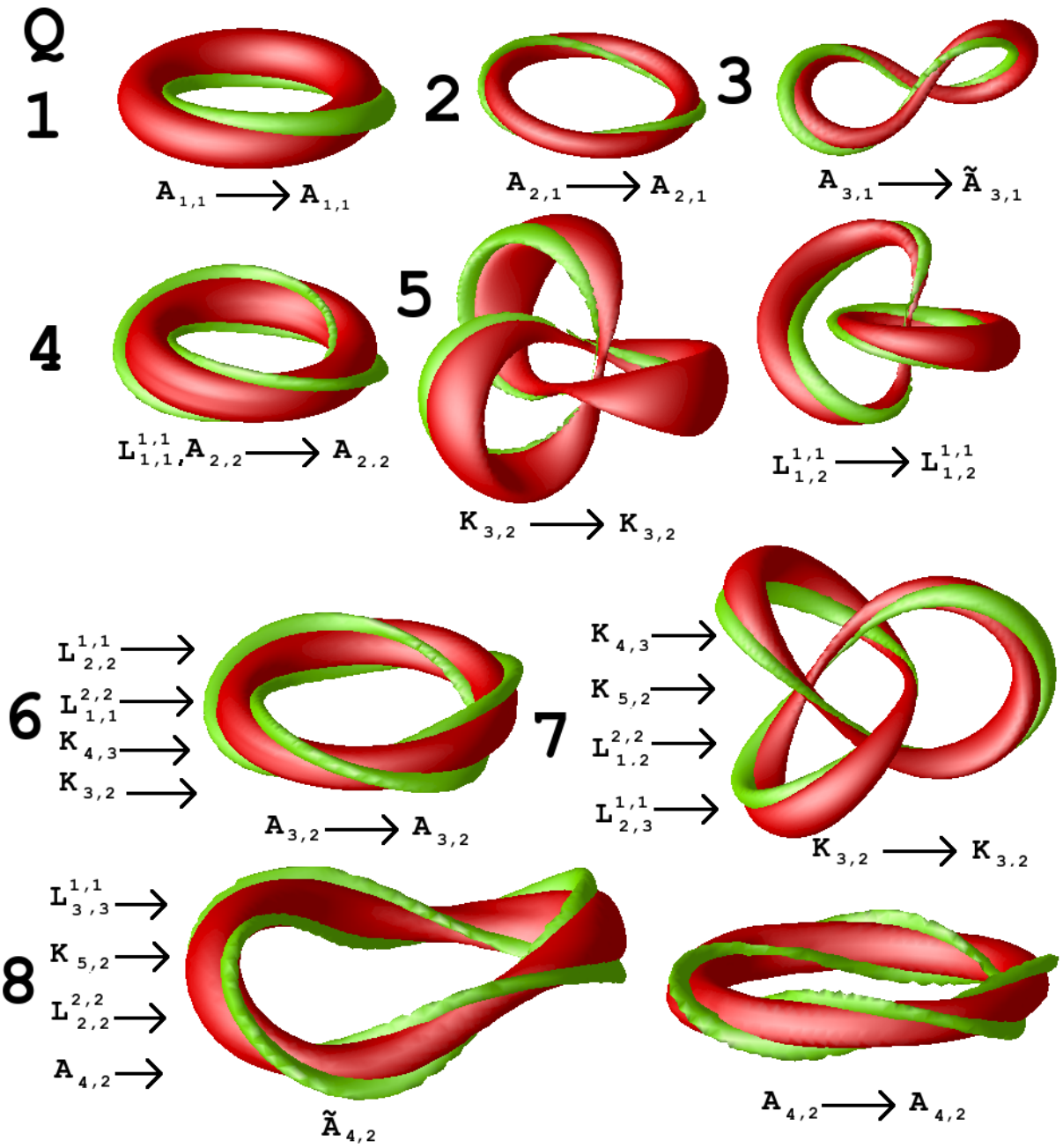

Figure 6.5: Hopf index $\mathcal{Q} = 1 - 7$ soliton solutions in the AFZ model.

Perhaps another method of breaking the symmetry could also be used to back up these results. In either case, the Hopf index eight soliton differs from the solitons in the Nicole and Skyrme-Faddeev models.

6.4.1 Increasing ϵ

The results presented above were found using mainly $\epsilon = 0.01$. On occasion short runs using $\epsilon = 0.02 - 0.05$ may be performed to overcome breakdowns in the minimisation

process resulting from symmetry problems in the AFZ model. Taking $\epsilon \geq 0.05$ during minimisation can have a large influence on the resulting static solutions for some Hopf charges. Increasing ϵ for $\mathcal{Q}=1,2,3,4,5$ and 7 does not alter the topology of the solitons. The only change is in the energy, where the field has been slightly altered to minimise the increased proportion of Nicole model energy present in the minimisation process.

At Hopf index 6, minimising the knotted configurations with a larger ϵ leads to a $\mathcal{K}_{3,2}$ type configuration. For small ϵ, they minimise towards a $\mathcal{K}_{3,2}$ where the position is squashed into a plane and the string sections are close together. For larger ϵ the strings move apart, but the knot still remains somewhat squashed. The linked configurations evolve towards an $\mathcal{L}^{1,1}_{2,2}$ type configuration when $\epsilon > 0.05$, which may be expected since the minimal energy solution in the Nicole model is of this type. The $\mathcal{A}_{3,2}$ configuration can also be altered by increasing ϵ. Taking ϵ between 0.05 and 0.10 can evolve the field towards a twisted $\tilde{\mathcal{A}}_{3,2}$ type configuration, but with increased AFZ energy. In all cases, the energy is significantly larger than the small ϵ minimisations.

Similar results occur at Hopf index 8. For $\epsilon < 10$ the evolution tends towards an $\tilde{\mathcal{A}}_{4,2}$ twisted configuration. If ϵ is increased further the configuration splits into an $\mathcal{L}^{2,2}_{2,2}$ type link configuration. An $\mathcal{L}^{1,1}_{3,3}$ type configuration evolves towards an $\tilde{\mathcal{A}}_{4,2}$ twisted configuration for low ϵ, but the two strings do not seem to be able to cross over to the $\tilde{\mathcal{A}}_{4,2}$ configuration using the symmetry breaking minimisation. Without the symmetry breaking the minimisation breaks down. Increasing ϵ leads to an $\mathcal{L}^{1,1}_{3,3}$ type configuration like that seen in the Skyrme-Faddeev model, where they lie close to each other almost in a plane. This is different to the static $\mathcal{L}^{1,1}_{3,3}$ configuration in the Nicole model, which has two unlinks linked perpendicular to each other. Again these configurations have a much larger AFZ energy than for small ϵ. This behaviour might account for the broken symmetry minimisation resulting in an $\tilde{\mathcal{A}}_{4,2}$ twisted configuration rather than an axial $\mathcal{A}_{4,2}$ configuration for small ϵ.

6.5 Conclusion

Non-axial solitons in the AFZ model are hard to find. Scale invariance can be overcome using volume preserving flow, but other difficulties relating to the symmetries of the

model prevent a simple implementation. By adding a symmetry breaking term into the minimisation, static solutions can be found. These solutions include knotted and linked configurations, including the first minimal energy knot at Hopf index five found in Hopf soliton models. The Hopf index 7 soliton is again a knot, which seems to be common to all Hopf solitons models investigated to date. These results also fit well with the analytical axial solutions. It appears as though $\mathcal{Q}=n^2$ charged solitons are indeed axial $\mathcal{A}_{n,n}$ type solutions. Their energy is also close to the $\mathcal{Q}^{\frac{3}{4}}$ bound. Other axial $\mathcal{A}_{n,m}$ solutions appear to be minimal energy when $m \simeq n$, or $m/n > 0.5$. It is clear that although the results are accurate for lower charges, difficulties increase for $\mathcal{Q} > 7$. An axial $\mathcal{A}_{3,3}$ has yet to be constructed using this technique. Further investigation is needed into non-axial solutions to the AFZ model, but this evidence indicates that the AFZ model does have knotted and linked solutions for some Hopf charges.

The use of the symmetry breaking term in the minimisation leads to a new family of conformal Hopf models, made through linear combinations of the Nicole and AFZ models. Behaviour of solitons in these models will be discussed in the final chapter.

Chapter 7

Solitons in Conformal Skyrme-Faddeev Models

7.1 Introduction

The Nicole and AFZ models have been investigated both analytically and numerically. The most recent numerical developments have been detailed in the previous two chapters. Any linear combination of these two models will also result in a scale invariant theory with topological solitons. The set of all linear combinations of the Nicole and AFZ model forms a one parameter family of conformal field theories permitting Hopf solitons. They will be referred to as conformal Skyrme-Faddeev (CSF) models.

Differences in topology of minimal energy solutions at a given Hopf index in the Nicole and AFZ models has already been noted and is clearest in the case of square charges, $\mathcal{Q}=m^2$. Solitons with $\mathcal{Q}=m^2$ in the AFZ model are axial with equal winding about the 2 torus angles. Solitons with $\mathcal{Q}=m^2$ in the Nicole model are links and knots since the Nicole model does not appear to permit stable axial solitons above Hopf index 2. Investigation of solitons in the conformal Skyrme-Faddeev models and the topological transition of solutions across the set could shed some light on the nature of the solutions of the Nicole and AFZ models. They may also lead to some insights about the Skyrme-Faddeev model and its solitons.

The one parameter family of conformal Skyrme-Faddeev models $\mathcal{L}(\theta)$ are

$$\mathcal{L}(\theta) = \cos^2(\theta)\mathcal{L}_{Ni} + \sin^2(\theta)\mathcal{L}_{AFZ}. \tag{7.1.1}$$

Both Lagrangian components have been previously introduced (5.1.2), (6.1.1), and $\theta \in [0, \frac{\pi}{2}]$. The two extremes of the set give each model individually, the Nicole model is recovered when $\theta = 0$ and the AFZ model is recovered when $\theta = \frac{\pi}{2}$. The static energy of this set of models is

$$E_\theta = \int \frac{\cos^2(\theta)\Lambda^{\frac{3}{2}} + \sin^2(\theta)H^{\frac{3}{4}}}{32\pi^2\sqrt{2}\cos^2(\theta) + 16\pi^2 2^{\frac{3}{4}}\sin^2(\theta)}\, d^3x. \tag{7.1.2}$$

This energy has been normalised so that $E_0 = E_{\frac{\pi}{2}} = 1$ for $\mathcal{Q} = 1$, i.e. the energy of the Hopf map is set to one in both the Nicole and AFZ models, keeping in line with the conventions used in previous chapters.

7.2 Volume Preserving Flow

The conformal Skyrme-Faddeev models are clearly scale invariant $\forall\theta$, so energy minimisation can be conducted using volume preserving flow. The energy densities, taking into account that $\boldsymbol{\phi}$ takes values on the two-sphere, are

$$\mathcal{E}_\theta = \cos^2(\theta)\mathcal{E}_{Ni} + \sin^2(\theta)\mathcal{E}_{AFZ} + \gamma_\theta\left(1 - \boldsymbol{\phi}\cdot\boldsymbol{\phi}\right). \tag{7.2.1}$$

Each model will require its own Lagrange multiplier, γ_θ and the energy densities of the Nicole and AFZ models are as defined previously, i.e.

$$\mathcal{E}_{Ni} = (\partial_i\boldsymbol{\phi}\cdot\partial_i\boldsymbol{\phi})^{\frac{3}{2}} \equiv \Lambda^{\frac{3}{2}}, \qquad \mathcal{E}_{AFZ} = [(\partial_i\boldsymbol{\phi}\times\partial_j\boldsymbol{\phi})\cdot(\partial_i\boldsymbol{\phi}\times\partial_j\boldsymbol{\phi})]^{\frac{3}{4}} \equiv H^{\frac{3}{4}}. \tag{7.2.2}$$

The equations of motion for this model are just a linear combination of the individual equations of motion, leading to gradient flow given by

$$\boldsymbol{F}_\theta = \cos^2(\theta)\boldsymbol{F}_{Ni} + \sin^2(\theta)\boldsymbol{F}_{AFZ} + \gamma_\theta\boldsymbol{\phi}. \tag{7.2.3}$$

$\boldsymbol{F}_{Ni}$ and $\boldsymbol{F}_{AFZ}$, (6.3.6, 6.3.9), were defined earlier:

$$\begin{aligned}\boldsymbol{F}_{Ni} &= \nabla^2\boldsymbol{\phi}\Lambda^{\frac{1}{2}} + \partial_i\boldsymbol{\phi}\left(\partial_i\partial_j\boldsymbol{\phi}\cdot\partial_j\boldsymbol{\phi}\right)\Lambda^{-\frac{1}{2}}, \qquad (7.2.4)\\ \boldsymbol{F}_{AFZ} &= H^{-\frac{1}{4}}\left[\nabla^2\boldsymbol{\phi}\Lambda + \partial_i\boldsymbol{\phi}\left(\partial_i\partial_j\boldsymbol{\phi}\cdot\partial_j\boldsymbol{\phi}\right) - \partial_i\partial_j\boldsymbol{\phi}\left(\partial_i\boldsymbol{\phi}\cdot\partial_j\boldsymbol{\phi}\right) - \partial_j\boldsymbol{\phi}\left(\nabla^2\boldsymbol{\phi}\cdot\partial_j\boldsymbol{\phi}\right)\right]\\ &+ H^{-\frac{5}{4}}\left[\left(\partial_i\partial_j\boldsymbol{\phi}\cdot\partial_j\boldsymbol{\phi}\right)\Lambda - \left(\partial_i\partial_j\boldsymbol{\phi}\cdot\partial_k\boldsymbol{\phi}\right)\left(\partial_j\boldsymbol{\phi}\cdot\partial_k\boldsymbol{\phi}\right)\right]\left[\partial_l\boldsymbol{\phi}\left(\partial_i\boldsymbol{\phi}\cdot\partial_l\boldsymbol{\phi}\right) - \partial_i\boldsymbol{\phi}\Lambda\right].\end{aligned}$$

The Lagrange multiplier is found as the flow must map to solutions still on the two-sphere, i.e. $\boldsymbol{\phi}\cdot\boldsymbol{F}_\theta = 0$, such that

$$\gamma_\theta = -\cos^2(\theta)\boldsymbol{\phi}\cdot\boldsymbol{F}_{Ni} - \sin^2(\theta)\boldsymbol{\phi}\cdot\boldsymbol{F}_{AFZ}. \qquad (7.2.5)$$

Volume preserving flow can then be applied to fix a scale for the energy minimisation by moving in a direction which preserves the global total of an appropriately chosen volume term.

$$\frac{\partial\boldsymbol{\phi}}{\partial t_\theta} = \boldsymbol{F}_\theta - \frac{\langle\boldsymbol{f}\cdot\boldsymbol{F}_\theta\rangle}{\langle\boldsymbol{f}\cdot\boldsymbol{f}\rangle}\boldsymbol{f}, \quad \text{with} \quad \boldsymbol{f} = -\frac{\delta v}{\delta\boldsymbol{\phi}}, \quad \text{and} \quad v = \frac{1}{2}\left(1 - \boldsymbol{\phi}\cdot\boldsymbol{e}_3\right). \qquad (7.2.6)$$

The same term used in volume preserving flow of the Nicole and AFZ models is still an appropriate choice for fields taking values in a domain Ω. The field must tend to a constant value on $\partial\Omega$, again set to be $\boldsymbol{\phi} = (0, 0, 1)$, for the energy to remain finite. The position of the solitons will again be where the field is antipodal to this vacuum value.

7.3 Solitons and Transitions

To see how the soliton configurations alter with θ, it is best to pick a Hopf index where there is a difference between the soliton configurations for the global minima at either end of the spectrum. Square Hopf index, $\mathcal{Q} = n^2$, solutions seem a good candidate as the global minima in the AFZ model are axially symmetric and are non-axial in the Nicole model. Other Hopf charges, such as $\mathcal{Q} = 5$, 6 and 8 could also be interesting. Investigating changes in static, minimal energy soliton configurations of conformal Skyrme-Faddeev models could be undertaken for any of these.

Areas of interest here relate to whether there is a slow change in configuration as θ changes; whether the energy of the two configurations meet in the middle where both

configurations have the same energy; whether an intermediate soliton configuration exists in between the two extreme θ's or whether there is a sudden topological change in solutions at a given θ.

7.3.1 Variation of θ

The lowest Hopf index that shows topological differences in the global energy minima between solutions to the Nicole model and the AFZ model is $\mathcal{Q} = 4$. The Nicole model soliton is an $\mathcal{L}^{1,1}_{1,1}$ type linked configuration, with no other stable local minima existing. In the AFZ model, it has been seen earlier that the soliton configuration representing the global energy minimum is an $\mathcal{A}_{2,2}$ type field configuration. It also appears to be the only stable local minimum although, as the amount of Nicole model added to the energy minimisation increases, an $\mathcal{L}^{1,1}_{1,1}$ type linked configuration can be found. It has a very similar AFZ energy to that of the $\mathcal{A}_{2,2}$ field, although the field configuration is somewhat symmetrical (see figure 6.5). Energy minimisations made with $\sim 5\%$ Nicole model contribution will usually form an $\mathcal{L}^{1,1}_{1,1}$ type configuration, but one which is visually very similar to an $\mathcal{A}_{2,2}$, with the two linked rings lying very close together. This may be an artefact of the energy minimisation method and has been discussed in detail previously.

The numerical calculations were conducted in a cubic domain Ω with volume 150^3. It comprises of a lattice with unit spacing and derivatives are calculated using a finite difference method with fourth order accuracy. The fields are evolved using the volume preserving flow method, where the flow is evaluated using an explicit method with a timestep $\Delta t \leq 0.1$. Minimisation where $\theta \approx \frac{\pi}{2}$ will require a much reduced timestep to nullify problems relating to the AFZ model discussed in chapter 6. The results presented will have a volume $V = 160000$ and will result from initial configurations determined by rational maps $\mathcal{A}_{2,2}$ and $\mathcal{L}^{1,1}_{1,1}$ detailed in chapter 4. The volume, energy and inner products will be evaluated as a summation over the lattice.

Table 7.1 shows a breakdown of the energies over a range of θ for both the link and the axial solitons. Figure 7.1 shows these plots for the full range of θ (top) and in the range of topological change (bottom). The (left) plots are $E/\mathcal{Q}^{\frac{3}{4}}$ against θ and the (right) plots are $E/\mathcal{Q}^{\frac{3}{4}}$ against $\sin^2\theta$. For Hopf index 4, $\mathcal{L}^{1,1}_{1,1}$ type configurations exist and have very

CSF Energy for a Range of Theta							
$\mathcal{L}^{1,1}_{1,1}$ **link**				**Axial** $\mathcal{A}_{2,2}$			
θ	$\sin^2(\theta)$	E	$E/\mathcal{Q}^{\frac{3}{4}}$	θ	$\sin^2(\theta)$	E	$E/\mathcal{Q}^{\frac{3}{4}}$
0.00	0.000	3.165	1.119	0.80	0.515	3.145	1.112
0.05	0.002	3.165	1.119	0.81	0.525	3.143	1.111
0.10	0.010	3.165	1.119	0.82	0.535	3.141	1.110
0.15	0.022	3.165	1.119	0.83	0.545	3.139	1.110
0.20	0.039	3.164	1.119	0.84	0.554	3.136	1.109
0.25	0.061	3.164	1.118	0.85	0.564	3.134	1.108
0.30	0.087	3.163	1.118	0.86	0.574	3.132	1.107
0.35	0.118	3.162	1.118	0.87	0.584	3.129	1.106
0.40	0.152	3.160	1.117	0.88	0.594	3.127	1.105
0.45	0.189	3.159	1.117	0.89	0.604	3.124	1.104
0.50	0.230	3.157	1.116	0.90	0.614	3.121	1.104
0.55	0.273	3.155	1.116	0.91	0.623	3.119	1.103
0.60	0.319	3.153	1.115	0.92	0.633	3.116	1.102
0.65	0.366	3.150	1.114	0.93	0.643	3.113	1.101
0.70	0.415	3.147	1.113	0.94	0.652	3.110	1.100
0.75	0.465	3.143	1.111	0.95	0.662	3.107	1.098
0.79	0.500	3.139	1.110	1.00	0.708	3.090	1.092
0.80	0.515	3.138	1.109	1.05	0.752	3.071	1.086
0.81	0.525	3.137	1.109	1.10	0.794	3.049	1.078
0.82	0.535	3.136	1.109	1.15	0.833	3.025	1.070
0.83	0.545	3.134	1.108	1.20	0.869	2.999	1.060
0.84	0.554	3.133	1.108	1.25	0.901	2.971	1.050
0.85	0.564	3.132	1.107	1.30	0.928	2.943	1.040
0.86	0.574	3.130	1.107	1.35	0.952	2.911	1.029
0.87	0.584	3.129	1.106	1.40	0.971	2.884	1.020
0.88	0.594	3.128	1.106	1.42	0.977	2.874	1.016
0.89	0.604	3.127	1.105	1.45	0.985	2.858	1.011
0.90	0.614	3.126	1.105	1.47	0.990	2.850	1.008
0.91	0.623	3.125	1.105	1.50	0.995	2.839	1.004
0.92	0.633	3.124	1.104	1.52	0.997	2.834	1.002
0.93	0.643	3.122	1.104	1.54	0.999	2.830	1.001
0.94	0.652	3.121	1.103	1.56	1.000	2.829	1.000
0.95	0.662	3.120	1.103	1.57	1.000	2.828	1.000

Table 7.1: Static CSF energy for (left) $\mathcal{L}^{1,1}_{1,1}$ (right) $\mathcal{A}_{2,2}$ type initial conditions. $\mathcal{L}^{1,1}_{1,1}$ configurations with $\theta \gtrsim 0.87$ move towards an $\mathcal{A}_{2,2}$ type configuration. $\mathcal{A}_{2,2}$ energies with $\theta \lesssim 0.87$ are the energies of the axial configurations, which are saddle points of the minimisation. $\mathcal{A}_{2,2}$ configurations with $\theta \ll 0.87$ don't have static solutions as the field will attempt to unwind to a single string and collapse, see figure 7.4. Axial configurations for θ just under 0.87 can re-link and evolve towards the $\mathcal{L}^{1,1}_{1,1}$ minimal energy configuration. This transformation takes a very long time, due to the shallow gradient of the restricted energy functional in this region. Continued minimisation of the $\mathcal{L}^{1,1}_{1,1}$ solutions for $\theta > 0.87$ leads towards near-axial configurations, with an energy slightly larger than that of the $\mathcal{A}_{2,2}$ minimal energy solutions.

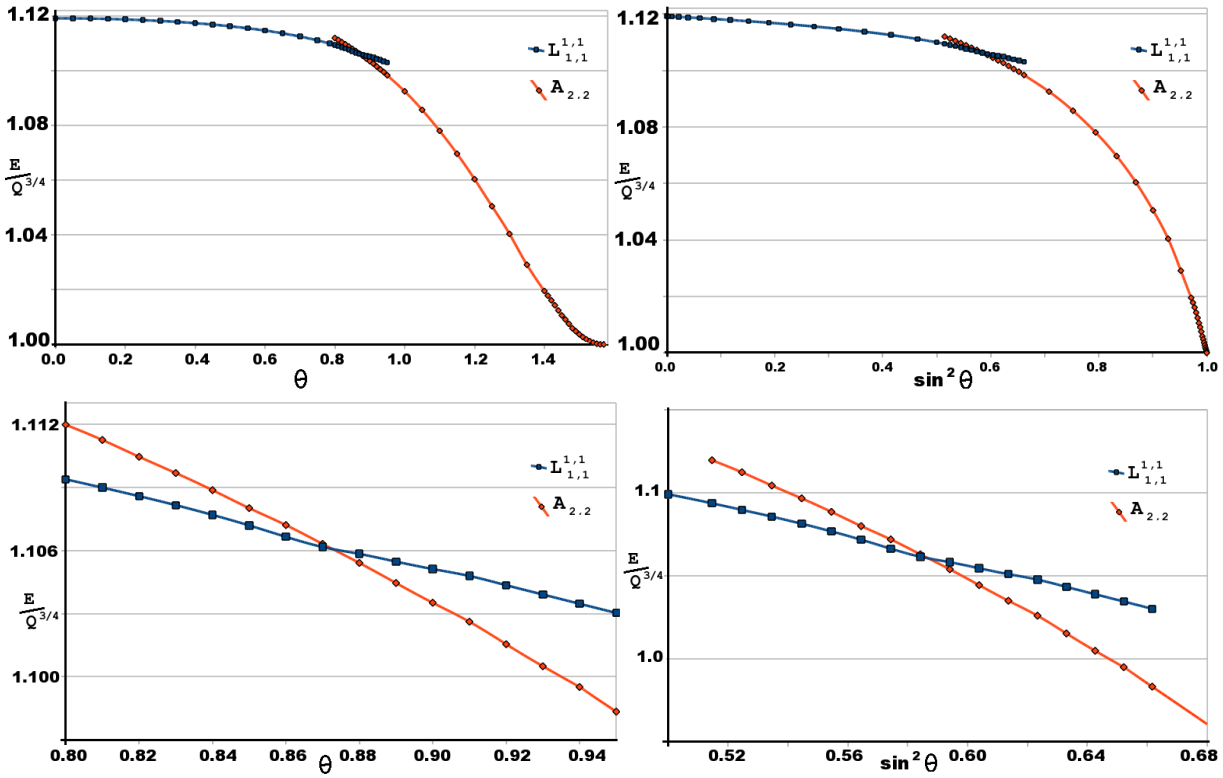

Figure 7.1: Plots of the CSF energies for both configurations for a range of θ's, details found in table 7.1. (top) Full range of θ and (bottom) region near transition $\mathcal{L}^{1,1}_{1,1} \leftrightarrow \mathcal{A}_{2,2}$. Plots are against θ (left) and $\sin^2\theta$ (right).

similar appearances for $\theta \lesssim \frac{\pi}{2}$, see figure 7.2. Axial $\mathcal{A}_{2,2}$ solitons exist and are similar in appearance for $\theta \gtrsim \frac{\pi}{3}$, see figure 7.3. The spacing between models considered, $\delta\theta$ is decreased for $\theta > \frac{3\pi}{7}$ due to issues relating to the AFZ model, as discussed in chapter 6. The range $\theta \in \left(\frac{\pi}{4}, \frac{\pi}{3}\right)$ is somewhat more complicated and more models are considered in this region. Some details are set out in figures 7.2 and 7.3. Figure 7.4 details the evolution of axial solutions for $\theta \lesssim \frac{\pi}{4}$.

The two components are self intersecting in the Nicole model and as $\theta \to \frac{\pi}{4}$ the self intersection is broken. For $\frac{\pi}{4} < \theta \lesssim 0.87$ the unlinks move inward, eventually towards an $\mathcal{A}_{2,2}$ type configuration when $\theta \gtrsim 0.88$. Transitions between a configuration like figure 7.2 ($\theta = 0.81$) and the minimal configuration for a given θ in this range occurs over a very small energy range. For $\theta = 0.80$, the axial solution is only 0.2% above the linked solution. This error reduces quickly as $\theta \to 0.87$. Axial solutions lie in definite minima for $\theta \gtrsim \frac{\pi}{3}$. In the range $0.87 \gtrsim \theta \gtrsim \frac{\pi}{3}$, solutions fluctuate between an axial configuration and a configuration similar to figure 7.2 ($\theta = 0.88$). The energy fluctuates up and down by

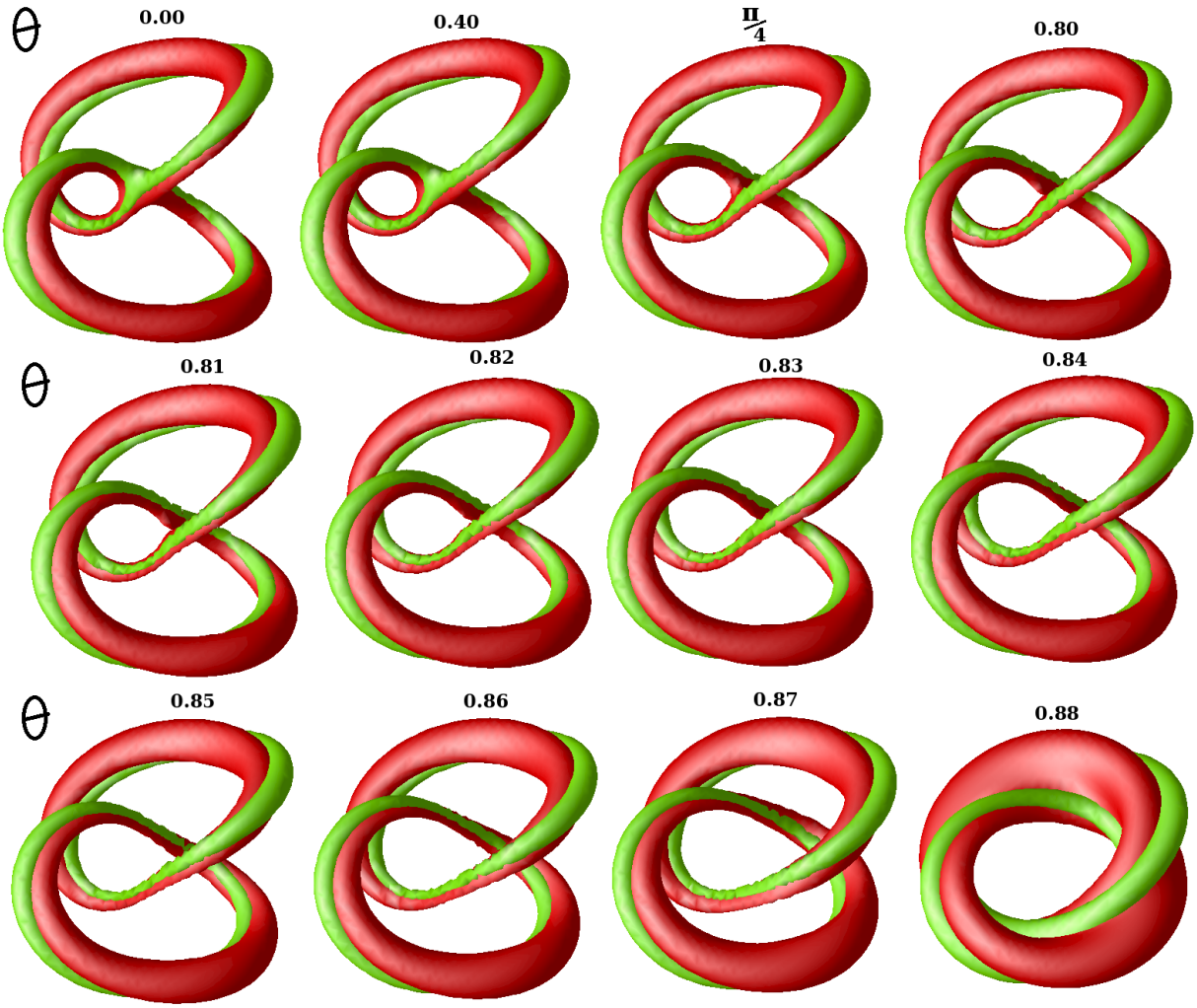

Figure 7.2: Position (red) and linking (green) plots for $\mathcal{L}^{1,1}_{1,1}$ minima for a range of θ. Above $\theta = 0.87$ solutions move towards $\mathcal{A}_{2,2}$ type configurations. For $\theta \gg \pi/2$, $\mathcal{L}^{1,1}_{1,1}$ initial conditions will lead to a similar configuration as with $\theta = 0.88$ and it has a slightly larger energy than an $\mathcal{A}_{2,2}$ minima for the same θ.

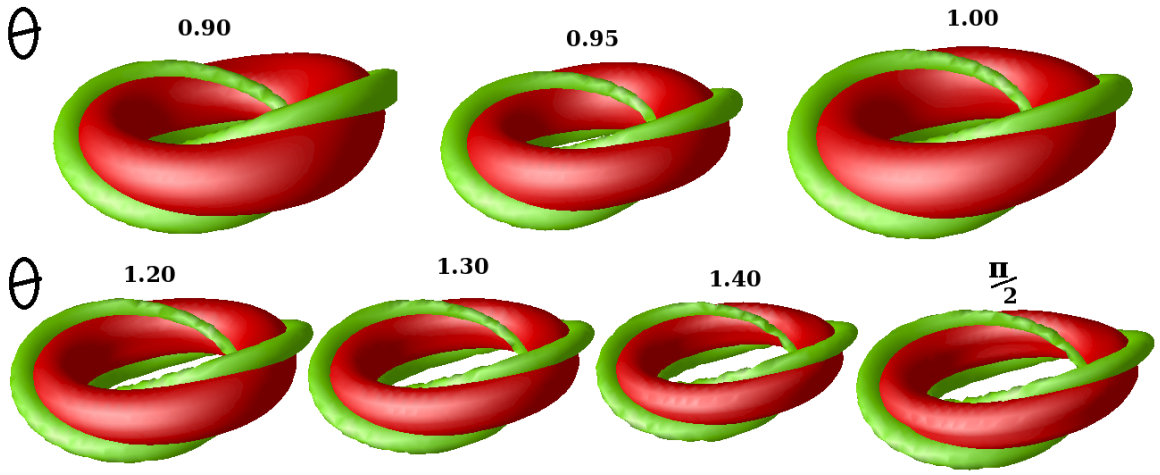

Figure 7.3: Position (red) and linking (green) plots for $\mathcal{A}_{2,2}$ minima for a range of θ. Configurations with $\theta \approx 0.9$ fluctuate between an $\mathcal{A}_{2,2}$ state like $\theta = 1.00$ and a slightly linked state like figure 7.2 ($\theta = 0.88$) with very little increase/decrease in energy. $\mathcal{A}_{2,2}$ configurations with $\theta \lesssim 0.86$ tend to try to unwind to a twisted single string configuration, then to a $\mathcal{L}^{1,1}_{1,1}$ link - collapsing along the way as a section becomes thin.

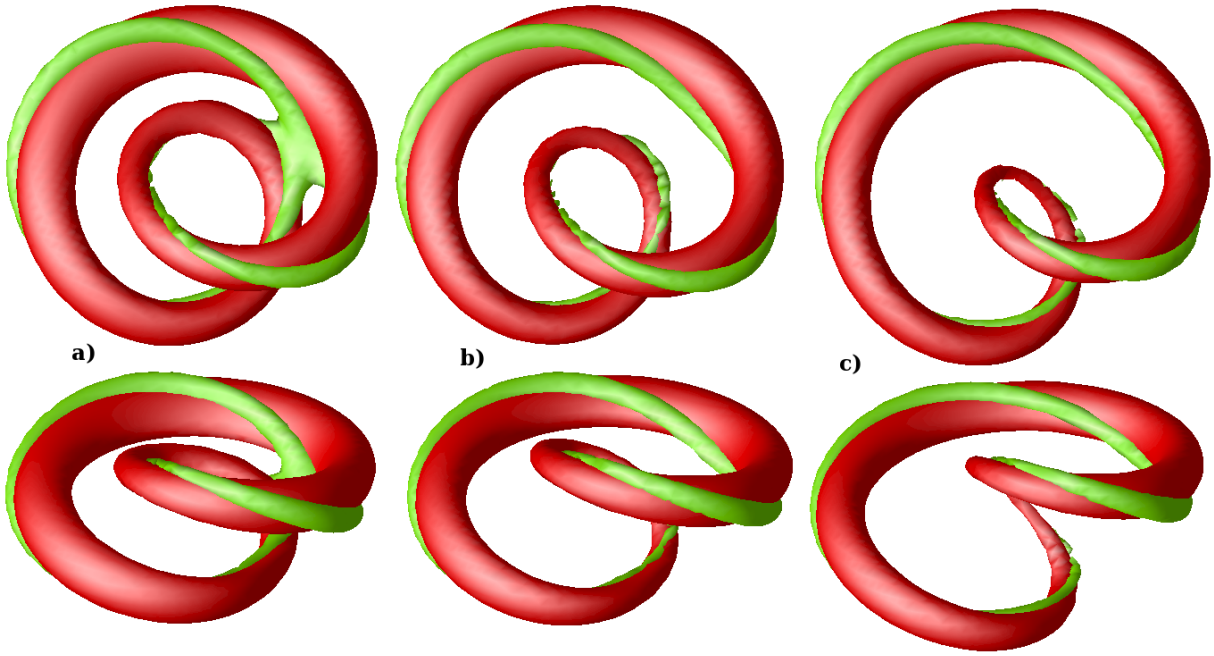

Figure 7.4: Position (red) and linking (green) plots $\mathcal{A}_{2,2}$ configurations for $\theta = 0.80$ during unwinding. The configurations has re-linked to form a single string configuration. The unwinding stages can be seen $a) \rightarrow c)$. The configuration will tend to collapse at sometime after c), as the position string around the most twisted section pinches off. If not for this pinching and collapse, the solution would likely evolve to an $\tilde{\mathcal{A}}_{4,1}$ configuration and then towards an $\mathcal{L}^{1,1}_{1,1}$ which is the only stable static solution for $\mathcal{Q} = 4$ in the $\theta = 0.80$ CSF model.

a fraction of a percent. This fluctuation indicates that either there are two local minima separated by a very low energy barrier and the minimisation cannot properly distinguish them in this range or that only one shallow local minima exists. Perturbations about this minima would then have a very similar energy if the gradient of the energy functional would be small for a wider range of field configurations.

Clearly the topological transition of solutions for $\mathcal{Q}{=}4$ occurs for $\theta > \frac{\pi}{4}$. This can be easily explained by analysing the Hopf map for the Nicole and AFZ models in the context of the CSF models. The rescaling terms in (5.1.10) and (6.1.2) tell the tail. Unscaled, the $\mathcal{Q} = 1$ energy in the Nicole model is $32\pi^2\sqrt{2} \approx 467$ and in the AFZ model it is $16\pi^2 2^{\frac{1}{4}} \approx 266$. This means that for the rescaling of the CSF models, each term gives an equally weighted contribution when $\theta \approx 0.91$. Minimisation effects would have an equal contribution from both terms for the Hopf index one solution here. This matches with the results for the transition seen. One might expect the transition of the $\mathcal{Q}{=}4$ soliton to occur slightly later rather than earlier as is seen. In the AFZ model $\mathcal{Q}{=}4$ is a square charge and so the solution is expected to attain the energy bound $16\pi^2 2^{\frac{1}{4}}\mathcal{Q}^{\frac{3}{4}}$ whereas the $\mathcal{Q} > 2$ solitons are around 11% above the energy bound $32\pi^2\sqrt{2}\mathcal{Q}^{\frac{3}{4}}$ (these energy

bounds are not normalised such that the Hopf map has an energy of one). Note that these bounds are not proven, they are simply the largest possible for behaviour like

$$E \geq c\mathcal{Q}^{\frac{3}{4}}, \tag{7.3.1}$$

where the constant c is the energy of the Hopf map in each case. These are the largest possible values of c allowed. One might then expect a topological transition to occur at around $\theta \sim 0.94$ rather than the $\theta \sim 0.87$ seen. The cause of the fluctuations in this region is the most likely explanation for this.

7.4 Conclusion

A one parameter family of conformal Skyrme-Faddeev models has been introduced. The two extremal models are the Nicole and AFZ models. The family of models has been investigated for a Hopf index with qualitatively different topology of static solutions to the extremal models. The energy transition, as the parameter is varied for these models, has been found. Details regarding the topological transition of the static solutions has been investigated throughout the set of models. The Nicole model is energetically less favourable for static solutions than the AFZ model, therefore more than half the models have static solutions resembling solitons in the Nicole model rather than the solitons of the AFZ model. In the region where contributions from the Nicole term and the AFZ term are roughly equal, static solutions are much harder to find. Volume preserving flow finds these minima reasonably well for most models. For parameters near to the topological transition of static solutions, solitons are found to be slightly unstable up to small perturbations. These solutions appear to have near-zero modes associated with transitions relating to the breaking of axial symmetry, at least in the $\mathcal{Q}=4$ case.

A number of issues relating to CSF models are left open to investigation. An explicit analysis of the stability of solutions to such models would be of use. Do the equations of motion of such models simplify in the same way as with the Nicole and AFZ models? Can an energy bound of the form (7.3.1) behaviour for all solutions be proven?

Conclusion

This thesis has introduced a modified gradient flow method that will minimise energy while leaving a number of globally defined quantities constant. This is the volume preserving flow detailed in chapter 2. Two simple examples were used to show the effectiveness of the technique, building on subjects introduced in chapter 1.

Volume preserving flow was then used to find minimal surfaces using domain wall networks. The minimal surfaces investigated were double bubbles on the square two and three-tori. Work on the two-torus reproduced analytic results to a good accuracy. All known double bubble configurations on the three-torus were also found, as well as a further static solution. Other solutions were also found, but only as saddle points of the minimisation held by symmetry.

Volume preserving flow was also used to find numerical solutions of Hopf soliton models which display conformal symmetry. Here symmetry was broken by the lattice and without some method of fixing a scale for solitons, broken zero modes evolved configurations to the trivial solution as the scale of the soliton shrinks below the lattice spacing. Details of Hopf solitons were introduced in chapter 4. Volume preserving flow was used to find solitons in the Nicole model (chapter 5), the AFZ model (chapter 6) and a one-parameter family of conformal Skyrme-Faddeev models (chapter 7) consisting of all linear combinations of the Nicole and AFZ models where the coefficients sum to one.

Solitons were found to the Nicole model for Hopf charges one to eleven. They showed some similarities with the solitons in the Skyrme-Faddeev model, while the topology of solutions at a given Hopf index did not always match. The configurations were similar for $\mathcal{Q} < 4$, $\mathcal{Q} = 5, 6, 7$ and 9. The solutions were all knots or links for $\mathcal{Q} > 3$.

Solitons in the AFZ model were found using a modified volume preserving flow with the addition of a symmetry breaking term. A small amount of the Nicole model was

added to the minimisation to overcome problems with the second derivative terms in the field equations. The resulting solitons matched well with the exact axial solutions for $\mathcal{Q}=1,2,4$ and 6. The $\mathcal{Q}=3$ soliton was a twisted axial configuration like those found in the Nicole and Skyrme-Faddeev models. The $\mathcal{Q}=5$ soliton was a trefoil knot, although a static link was also found with a slightly larger energy. Both solutions have a much lower energy than the exact axial solution. The $\mathcal{Q}=7$ soliton was once again a trefoil knot, as with other Hopf soliton models. The $\mathcal{Q}=8$ soliton found by the symmetry breaking and volume preserving minimisation was a twisted axial solution. It had an energy slightly above the exact axial solutions and it remains unclear whether ir not it is a static solution to the AFZ model or purely a static solution of the model with broken symmetry.

The one-parameter family of conformal Skyrme-Faddeev models were investigated for $\mathcal{Q}=4$, the lowest Hopf index where the two extremal models (AFZ and Nicole models) have topologically different solutions. The solutions changed slightly as the parameter moved the minimisation focus between the models. For most models, only one solution exists. This was a link in the Nicole-dominated models and axial in the AFZ-dominated models. The region where the two models had a roughly equal effect on the minimisation had more ambiguous solutions. A quick topological shift from axial to linked configurations occured. The solutions around this point seemed to have large, shallow minima. These configurations fluctuated under volume preserving minimisation.

This work has shown that volume preserving flow is a useful tool when looking for local minima in systems where solutions lack some kind of scale. Volume preserving flow could be used to investigate many systems. One such theory is the extended Skyrme-Faddeev model, where the theory is scale invariant under the correct constraints [67, 68]. Volume preserving flow could be used to find non-axial solitons, in addition to the axial solutions already found. Volume preserving flow could also provide a useful tool in the numerical construction of instantons which arise as solutions to the Yang-Mills equations in four-dimensional Euclidean space [69].

Appendix

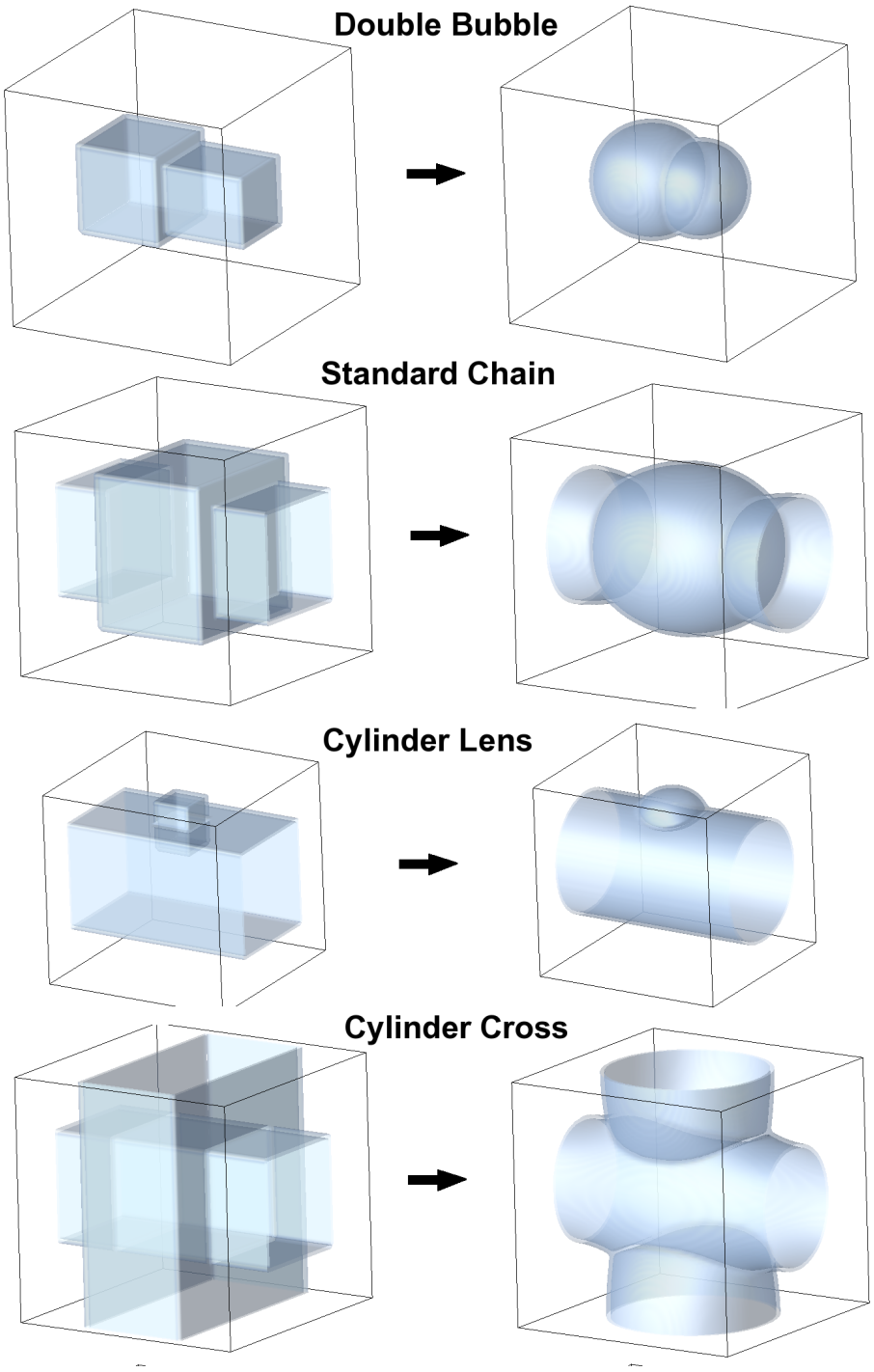

Figure 7.5: The start and end configurations for the possible minimisers in three-dimensions.

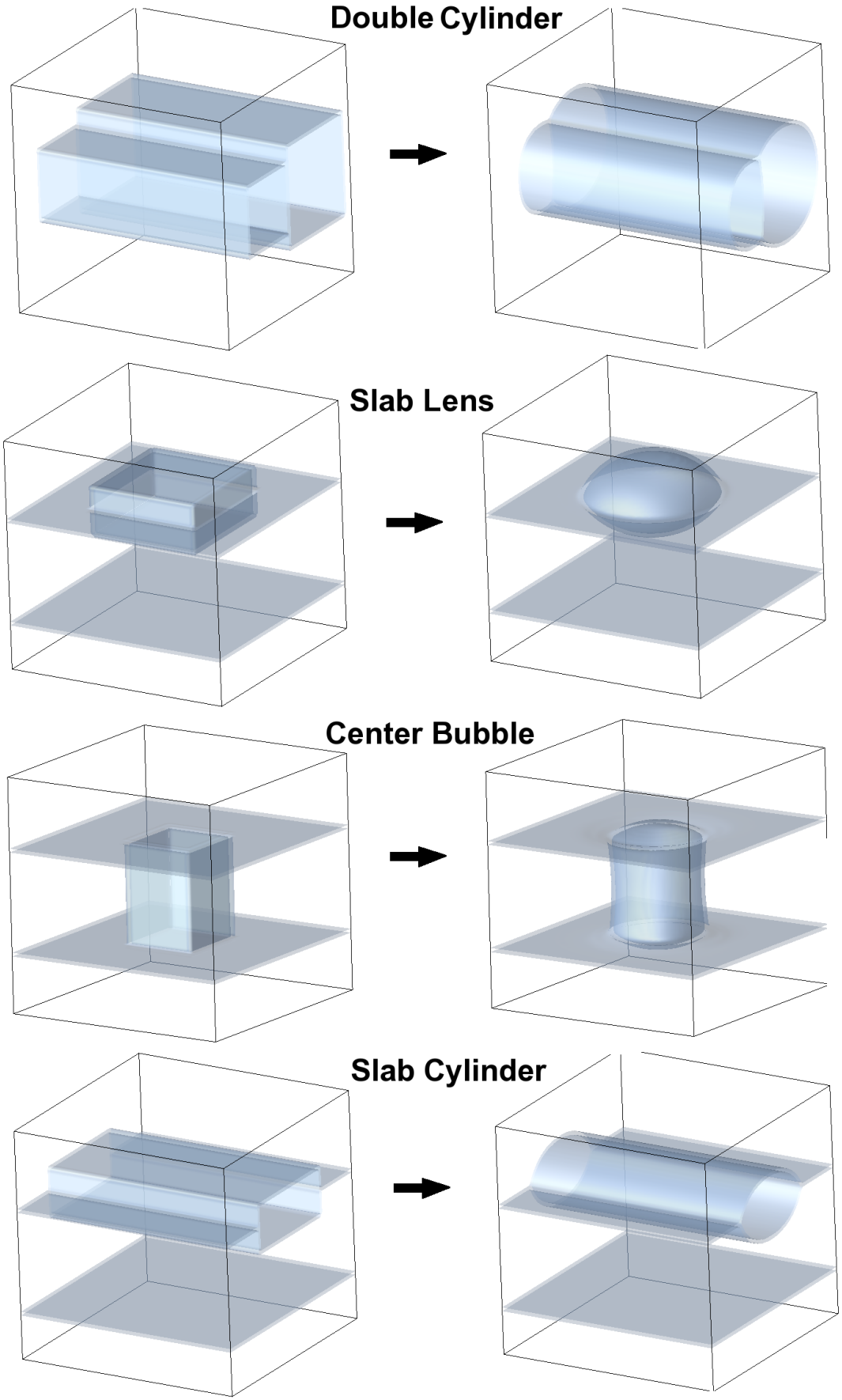

Figure 7.6: Start and end configurations continued.

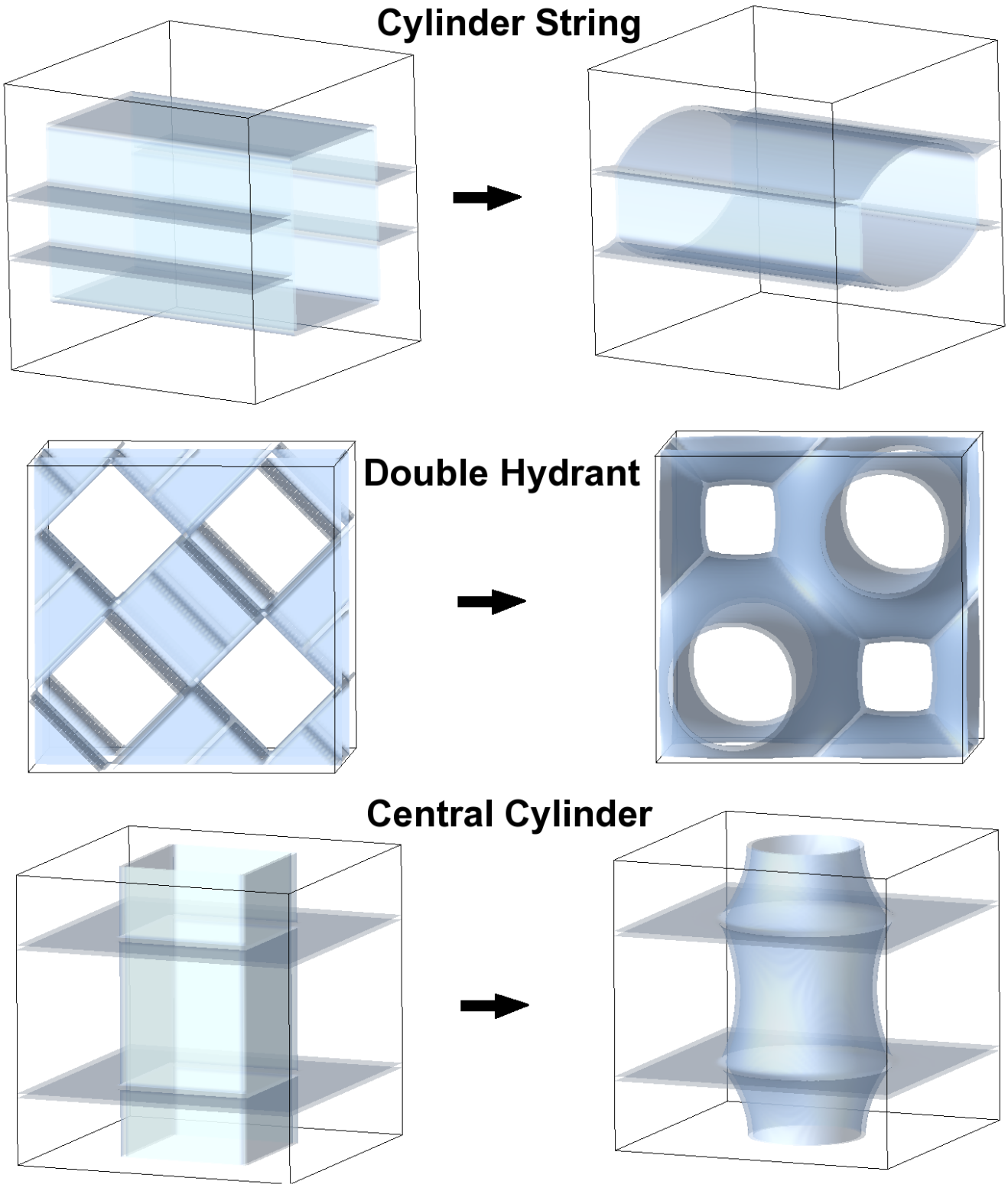

Figure 7.7: Start and end configurations continued.

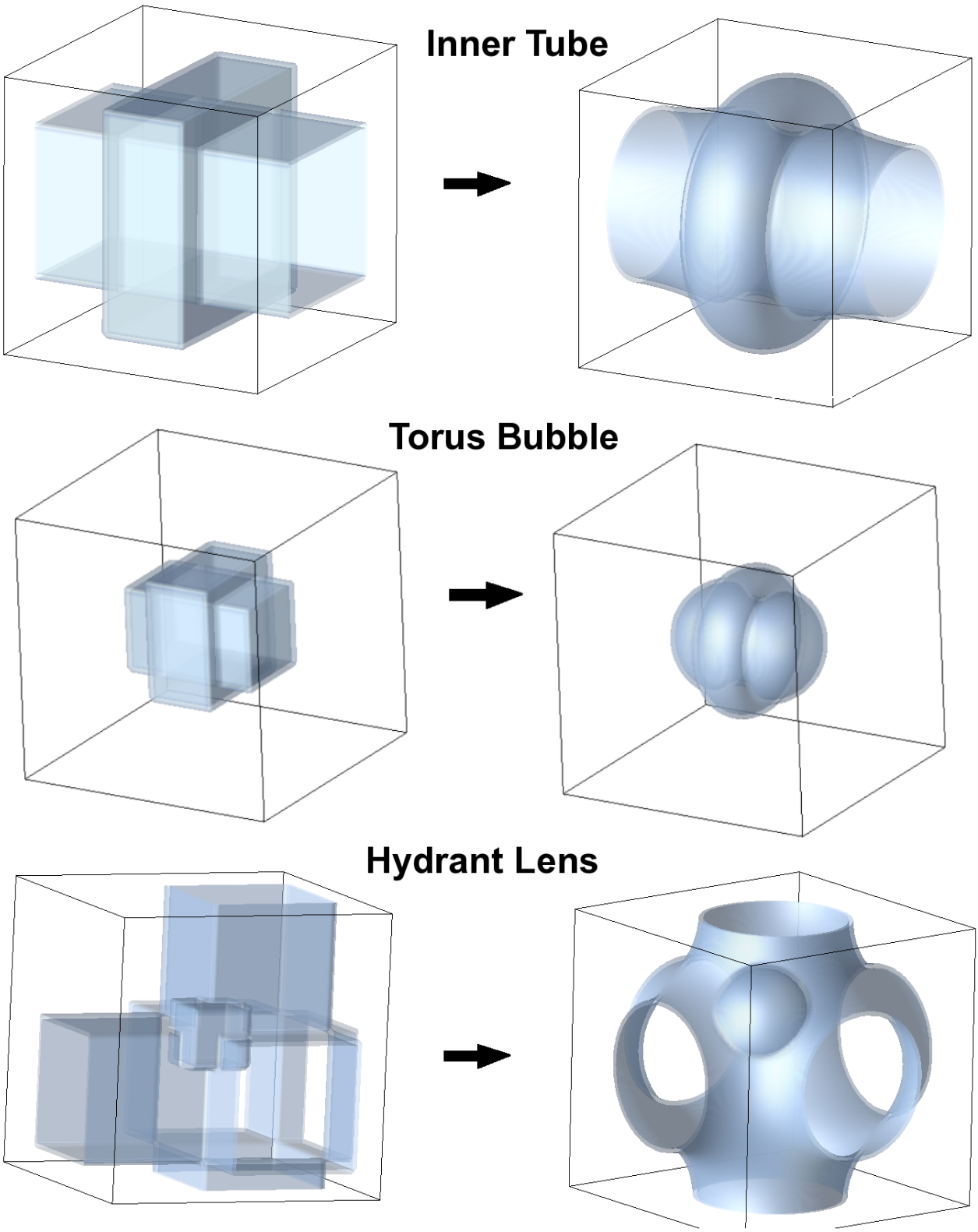

Figure 7.8: Start and end configurations continued.

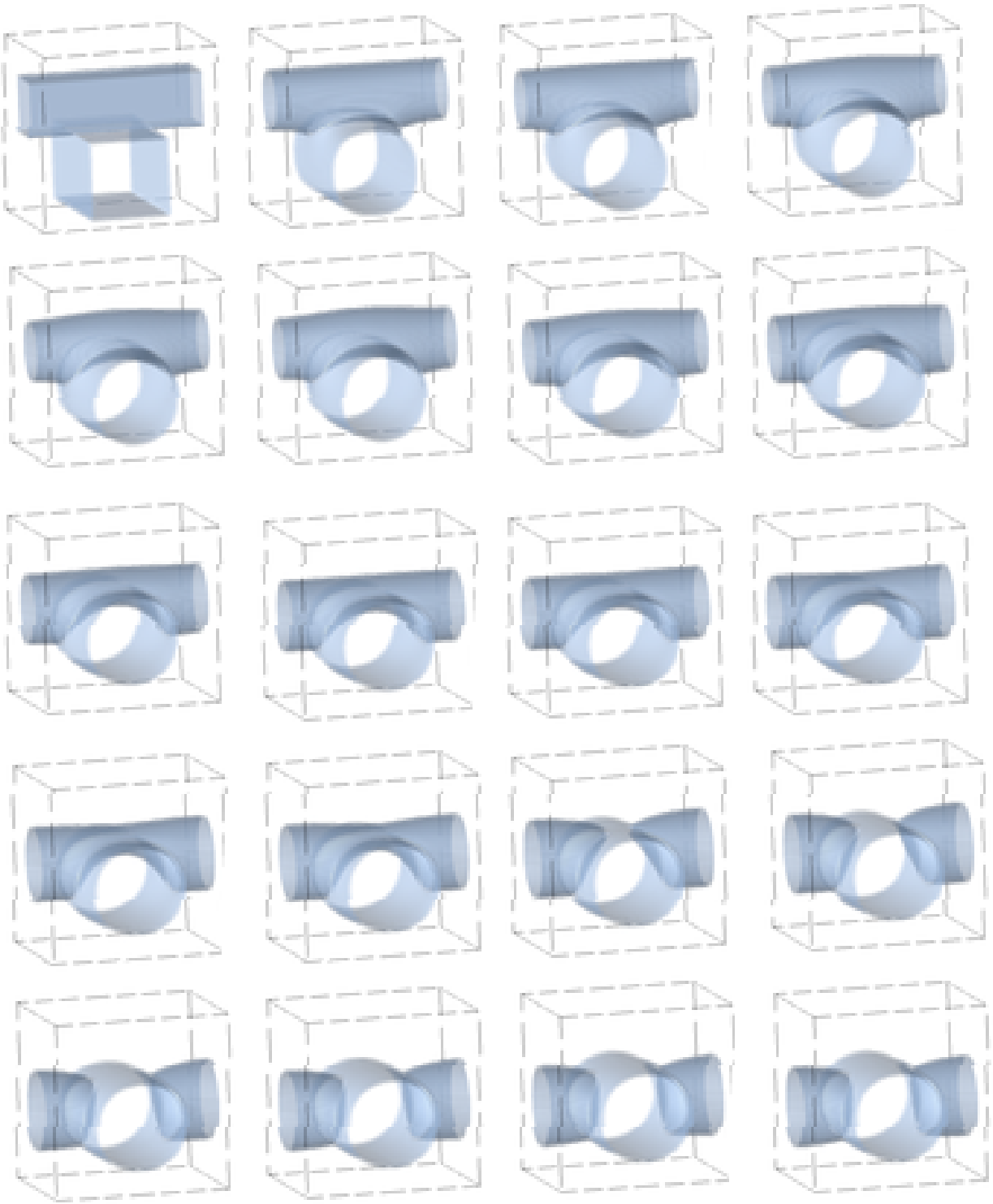

Figure 7.9: Transverse Cylinder evolution to a Cylinder Cross. Time increases left to right, row by row in each evolution given. The first row is time steps 1-4 and the next are steps 5-8, etc. reaching the final time step in the bottom right.

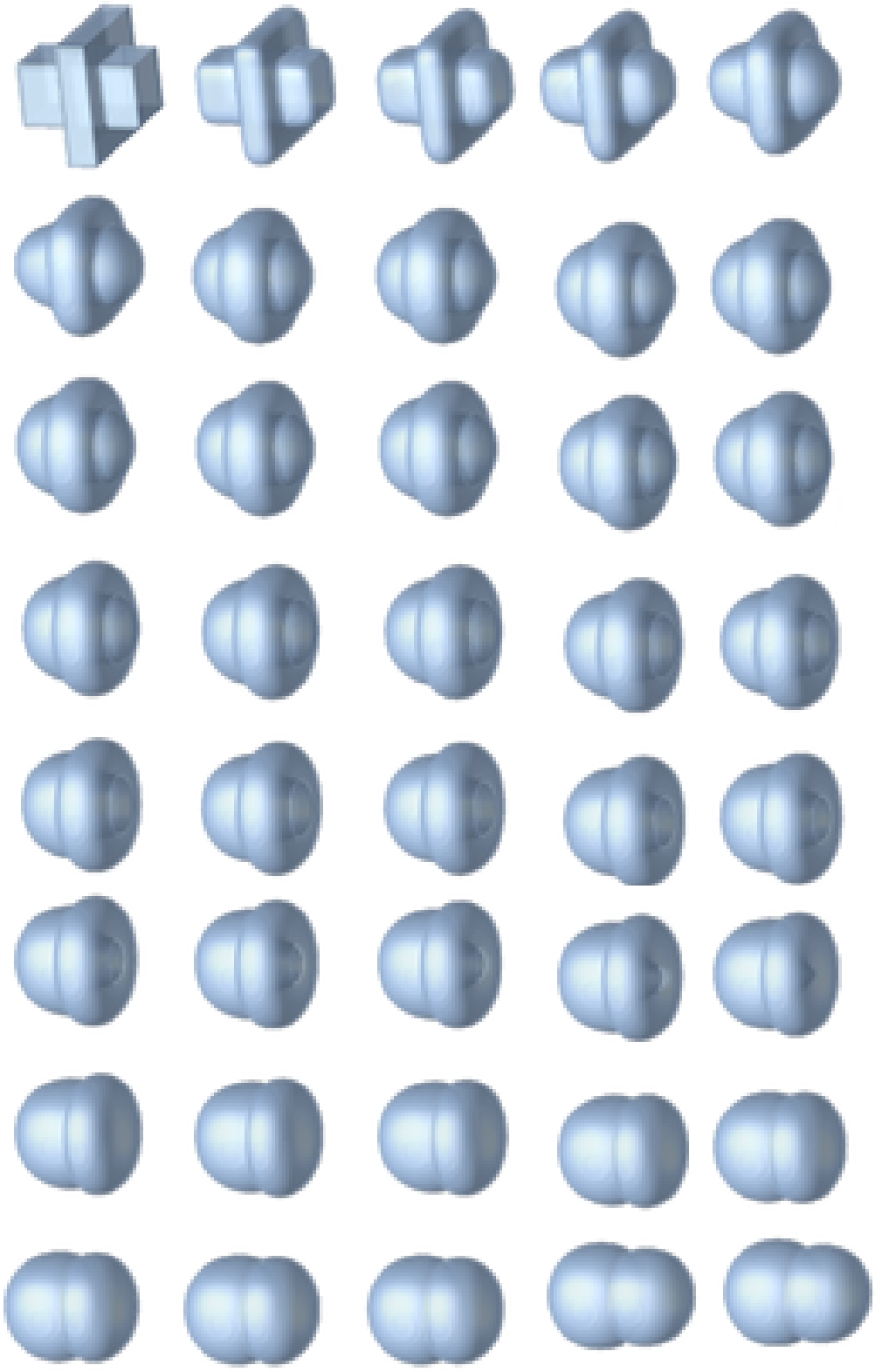

Figure 7.10: Torus Bubble evolution to a Double Bubble.

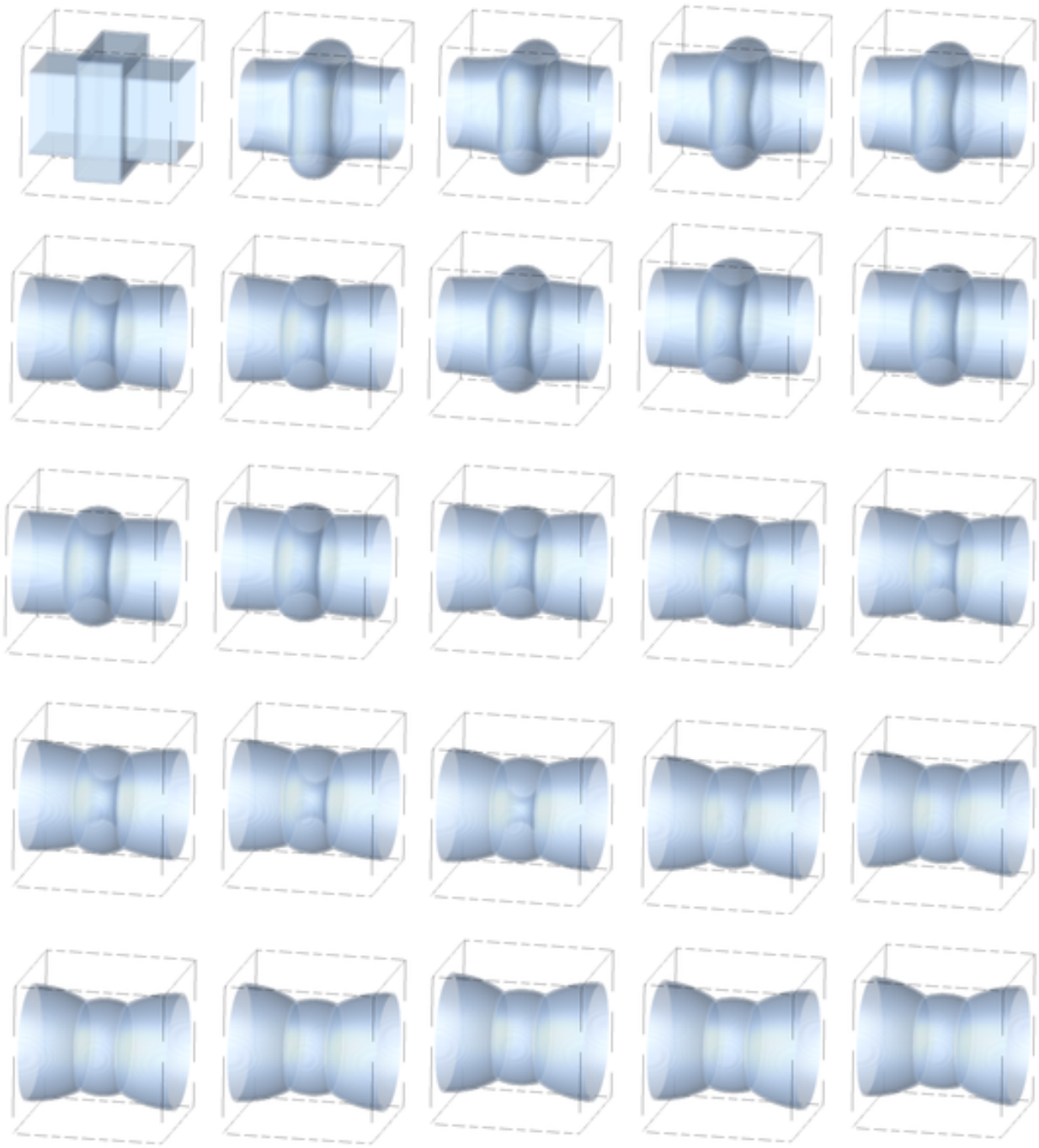

Figure 7.11: Inner Tube evolution to a Standard Chain.

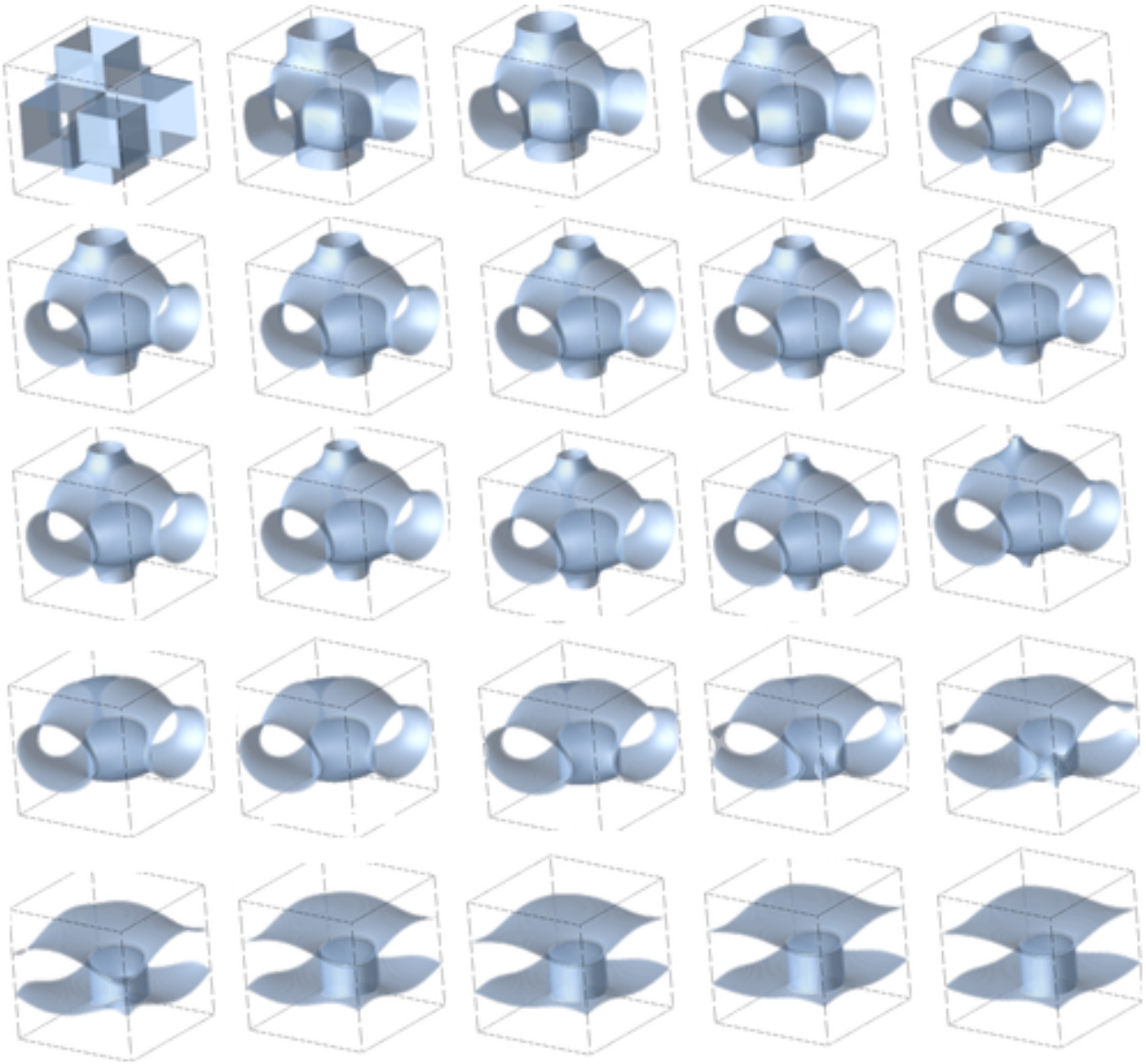

Figure 7.12: Hydrant Lens evolution to a Center Bubble.

Figure 7.13: Double Hydrant evolution to a Double Cylinder.

Bibliography

[1] M. Gillard, *http://arxiv.org/abs/1007.2335*.

[2] M. Gillard and P.M. Sutcliffe, *Proc. R. Soc. Lond.* **A465**, 2911 (2009).

[3] M. Gillard and P.M. Sutcliffe, *http://arxiv.org/abs/1009.2983*.

[4] A. Hatcher, *Algebraic topology*, Cambridge University Press (2002).

[5] M. Aubry, *Homotopy Theory and Models*, Boston, MA: Birkhuser (1995).

[6] G. H. Derrick, *J. Math. Phys.* **5**, 1252 (1964).

[7] L. D. Faddeev, Quantization of solitons, Princeton preprint IAS-75-QS70 (1975).

[8] D. A. Nicole, *J. Phys.* **G4**, 1363 (1978).

[9] H. Aratyn, L. A. Ferreira and A. Zimerman, *Phys. Lett.* **B456**, 162 (1999).

[10] H. Aratyn, L. A. Ferreira and A. Zimerman, *Phys. Rev. Lett.* **83**, 1723 (1999).

[11] E. B. Bogomolny, *Sov. J. Nucl. Phys.* **24**, 449 (1976).

[12] G. W. Gibbons and P. K. Townsend, *Phys. Rev. Lett.* **83**, 1727 (1999).

[13] E Albraham and P. K. Townsend, *Nucl. Phys.* **B351**, 313 (1991).

[14] P. M. Saffin, *Phys. Rev. Lett.* **83**, 4249 (1999).

[15] G. Woo, *J. Math. Phys.* **18**, 1264 (1977).

[16] A. Belavin and A. Polyakov, *JETP Lett.* **22**, 245 (1975).

[17] N. S. Manton and P. M. Sutcliffe, *Topological Solitons*, Cambridge University Press (2004).

[18] A. Peleg, M. Conti and B. Meerson, *Phys. Rev.* **E64**, 036127 (1990).

[19] W. Gautschi, *Numerical Analysis: An Introduction*, Springer (1997).

[20] R. L. Burden and J. D. Faires, *Numerical Analysis*, Brookes/Cole (2005).

[21] W. Cheneu and D. Kincaid, *Numerical Mathematics and Computing*, Brookes/Cole (2007).

[22] R. A. Leese, M. Peyrard and W. J. Zakrzewski, *Nonlinearity* **3**, 387 (1990).

[23] R. S. Ward, *Lett. Math. Phys.* **35**, 385 (1995).

[24] J. Plateau, *Statique expérimentale et théorique des liquides soumis aux seules forces molec- ulaires*, Gathier-Villars, Paris, (1873).

[25] H. A. Schwartz, *Beweis des Satzes, dass die Kugel kleinere Oberfläche besitzt als jeder andere Körper gleichen Volumens. Nachrichten Königlichen Gesellschaft Wissenschaften Göttingen* 1-13 (1884).

[26] D. Weaire and R. Phelan, *Phil. Mag. Lett.* **69**, 107-110 (1994).

[27] C. Isenberg, *The Science of Soap Films and Soap Bubbles*, Courier Dover Publications (1992).

[28] F. J. Almgren and J. E. Taylor, *Scientific American* **July**, 82-93 (1976).

[29] M. Alfaro, J. Brock, J. Foisy, N. Hodges and J. Zimba, *Pacific J. Math* **159**, 47-59 (1993).

[30] J. Hass, M. Hutchings and R. Schlafly, *Ann. of Math.* **151**, 459 (2000).

[31] M. Hutchings, F. Morgan, M. Ritoré and A. Ros, *Ann. of Math.* **155**, 459 (2002).

[32] B. W. Reichardt, *J. Geom. Ann.* **18**, 172-191 (2008).

[33] J. Corneli, P. Holt, G. Lee, N. Leger, E. Schoenfeld and B. Steinhurst, *Trans. Amer. Math. Soc.* **356**, 3769 (2004).

[34] M. Carrión Álvarez, J. Corneli, G. Walsh and S. Beheshti, *Experimental Mathematics* **12**, 79 (2003).

[35] N. D. Brubaker, S. Carter, S. M. Evans, D. E. Kravatz Jr., Sherry Linn, Stephen W. Peurifoy, and Ryan Walker , *Maths Horizons* **May**, 18-21 (2008).

[36] Q. Sheng and V. Elser, *Phys. Rev.* **B49**, 9977 (1994).

[37] W. T. Góźdź and R. Hołyst, *Phys. Rev.* **E54**, 5012 (1996).

[38] K. Brakke, *Experimental Mathematics* **1**, 141 (1992).

[39] H. Hopf, *Math. Ann.* **104**, 637-665 (1931).

[40] P. M. Sutcliffe, *Proc.Roy.Soc.Lond.A* **463**, 3001 (2007).

[41] B. M. A. G. Piette, B. J. Schroers and W. J. Zakrzewski, *Z. Phys* **C65**, 165 (1995).

[42] R. A. Battye and P. M. Sutcliffe, *Phys. Rev. Lett.* **81**, 4798 (1998).

[43] R. A. Battye and P. M. Sutcliffe, *Proc.Roy.Soc.Lond.A* **455**, 4305 (1999).

[44] D. Rolfsen, *Knots and Links*, American Mathematical Society Chelsea Publishing (1976).

[45] C. Adams, *The Knot Book: An Elementary Introduction to the Mathematical Theory of Knots*, American Mathematical Society (2004).

[46] E. Babaev, L. Faddeev, A. Niemi, *Phys. Rev. B* **65**, 100512 (2002).

[47] E. Babaev, *Phys. Rev. Lett.* **88**, 177002 (2002).

[48] L. Faddeev and A. J. Niemi, *Phys. Rev. Lett.* **82**, 1624 (1999).

[49] L. Faddeev and A. J. Niemi, *Phys. Lett. B* **449**, 214 (1999).

[50] L. Faddeev and A. J. Niemi, *Phys. Lett. B* **464**, 90 (1999).

[51] A. F. Vakulenko and L. V. Kapitanski, *Dokl. Akad. Nauk USSR* **246**, 840 (1979).

[52] A. Kundu and Yu. P. Rybakov, *J. Phys.* **A15**, 269 (1982).

[53] F. Lin and Y. Yang, *Commun. Math. Phys.* **249**, 273 (2004).

[54] L. Faddeev and A. J. Niemi, *Nature* **387**, 58 (1997).

[55] J. Gladikowski and M. Hellmund, *Phys. Rev.* **D56**, 5194 (1997).

[56] J. Hietarinta and P. Sato, *Phys. Lett.* **B451**, 60 (1999).

[57] J. Hietarinta and P. Sato, *Phys. Rev.* **D62**, 081701 (2000).

[58] R. Ward, *Phys. Lett. B* **473**, 291 (2000).

[59] C. Adam, J. Sánchez-Guillén, R. A. Vázquez and A. Wereszczyński *J. Math. Phys.* **47**, 052303 (2006).

[60] C. Adam, J. Sánchez-Guillén and A. Wereszczyński *J. Math. Phys.* **48**, 022305 (2007).

[61] A. Wereszczynski, *Eur. Phys. J.* **C41**, 265, (2005).

[62] A. Wereszczynski, *Eur. Phys. J.* **C38**, 261, (2004).

[63] O. Babelon and L. A. Ferreira, *JHEP* **0211**, 020, (2002).

[64] L.A. Ferreira and A.V. Razumov, *Lett. Math. Phys.* **55**, 143, (2001).

[65] C. Adam and J. Sánchez-Guillén, *J. Math. Phys.* **44**, 5243 (2003).

[66] C. Adam and J. Sánchez-Guillén, *JHEP* **01**, 004 (2005).

[67] L.A. Ferreira, N. Sawado and K. Toda, *JHEP* **11**, 124, (2009).

[68] L.A. Ferreira, N. Sawado and K. Toda, *JHEP* **03**, 119, (2010).

[69] A. A. Belavin, A. M. Polyakov, A. S. Schwartz and Y. S. Tyupkin, *Phys. Lett. B* **59**, 85, (1975).